Mechanisms and Factors Affecting Chromium Oxide Particle Reduction in Iron-Chromium Honeycombs

A Dissertation
Presented to
The Academic Faculty

by

Monique Sandra McIntosh

In Partial Fulfillment
of the Requirements for the Degree
Doctor of Philosophy in the
School of Materials Science and Engineering

Georgia Institute of Technology

April 2005

Mechanisms and Factors Affecting Chromium Oxide Particle Reduction in Iron-Chromium Honeycombs

Approved by:

Dr. Thomas H. Sanders, Jr., Chairman
Georgia Institute of Technology
Atlanta, GA

Dr. Janet M. Hampikian
Boise State
Boise, ID

Dr. Joe K. Cochran
Georgia Institute of Technology
Atlanta, GA

Dr. Henry Paris
Steward Inc.
Chattanooga, TN

Dr. Robert F. Speyer
Georgia Institute of Technology
Atlanta, GA

Date Approved: 18th April 2005

ACKNOWLEDGEMENTS

I would like to thank my parents, Mummy and Daddy, for their unfailing love and support. I also thank my sisters Marlene and Michele, my heroes who went before me as well as brothers El (the 4th kindest man I know) and Kawanish (big buddy) who have loved, protected, and covered me. I would like to mention my nephew Kamran because he is the future and with him here, life is more worthwhile. I thank my advisor Dr. Sanders who has not only supported me academically but has also looked out for me and went to bat for me several times. To Dr. Hampikian (committee member formerly known as advisor), who has supported me through the roughest times of my life. I am truly grateful. Words are not enough. I also thank my other committee members, Drs. Cochran, Speyer, and Paris for the various ways they have helped me along the way - a furnace here or a paper there. Also, a special thanks to Drs. Gokhale, Lee, Milam, Rosenstien, Thadhani, Snyder and Wang; and to James, Tim, Richard, and Yolande who have provided me with various forms of support and their expertise. To the MSE posse, who have collectively made this journey an interesting and inspiring one. Colleagues who have not only given me friendship but have also been there, giving me timely help when I was in need. Tammy (Methuselah's girl), Tracie, Chekesha, Ben, Matt, Matt, Ray, Mike, Mike, Iulianna, Scott, Arun, Shivonne and Simon (not by any means the least). Thank you. To the Beloved: my brothers and

sisters in the faith, especially the CHWC crew. I have found a home in you. Thank you to all my co-labourers who encouraged and strengthened me, who built me up and didn't tear me down. Thank you for seeing a diamond in me and not just walking by but chose to stop and see to it that I reach my full potential. To those who have always reminded me of God's promises and those who love me unfailingly, unconditionally, and in truth, thank you. If not for you, I wouldn't be here. Forgive me for not naming names. I fear if I name a few it would make the others feel small. You know who you are and I really appreciate you. Finally, I give thanks my Lord Jesus. You have never given up and You have never failed me. I have no other Friend like You. I am always amazed at how You make a way where there is no way and how You love in spite of it all. Lord, You are Lord. I am in awe. This material is based upon work supported by the National Science Foundation under Grant No. DMR-9624927.

TABLE OF CONTENTS

LIST OF TABLES

LIST OF FIGURES

SUMMARY

In the production of iron chromium honeycombs, iron oxide and chromium oxide mixtures are reduced by hydrogen at elevated temperatures to produce a metallic alloy. The complete reduction of the iron oxide occurs prior to the reduction of the chromium oxide. The reduction of the chromium oxide particles within the iron matrix is affected by factors that include the diffusion of the reduced chromium away from the chromium oxide particle into the iron matrix, the diffusion of the gaseous reactants and products to and from the chromium oxide particles, and the porosity of the iron matrix, which changes as a result of sintering. The type of heat-treatment used, (isothermal or non-isothermal, i.e., holding at a specific temperature versus using a steadily increasing temperature) plays a vital role in how these factors will affect chromium oxide reduction.

Experimental data were used in conjunction with sintering and dissolution models to obtain an understanding of the environment in which the chromium oxide particles reduce as a function of heat-treatment. This understanding will assist in the development of more effective processing steps for the reduction of metallic honeycombs from oxide mixtures.

CHAPTER 1

INTRODUCTION

Metallic honeycomb structures have numerous potential applications because they combine the desirable properties of their constituent alloy with the light weight provided by the open structures. Applications for metallic honeycomb structures include lightweight load-bearing structures, sound and thermal insulation components, and structural light-weighting for increased buoyancy. The use of honeycomb materials is expected to increase owing to their high stiffness-to-weight ratio and their flexibility in materials selection [1]. Metallic honeycombs can be fabricated to produce a form composed of one or a combination of a variety of metals. The target alloy in this research is chromium-containing steel.

Chromium-containing steels are important because of their high temperature properties. Their oxidation and creep resistance makes them well suited for applications such as exhaust systems or wherever high temperatures and pressures are experienced. The presence of chromium in the alloy also provides a protective passive layer of chromium oxide on the surface. Depending on overall chromium content, the alloy develops excellent corrosion resistance.

This research involves chromium-containing steels in honeycomb structures that are produced by the reduction of extruded oxides of iron and chromium. It is therefore

important to investigate the reduction kinetics of iron and chromium oxide mixtures extruded into honeycomb structures.

Traditionally honeycombs are fabricated from foils that are shaped and then joined by various methods [1]. However, these shaping and joining processes limit the selection of alloys that can be used, only to those that exhibit sufficient ductility to be formed. A recent technique for fabricating honeycomb structures involves a room temperature extrusion process [2, 3]. Extrusion is a forming method that permits shaping of a paste or a metal at elevated temperatures into a linear form of constant cross-section [4, 5]. The honeycomb product produced in this way is therefore a complete unit. Eliminating the joining step is beneficial in that differences in electrochemical potentials between the weld and base metal are removed. It is also no longer necessary to account for the mechanics of having a joint that is dissimilar with the rest of the structure.

Metallic honeycomb structures are best fabricated by reducing the extruded oxide pastes, rather than by extruding metal pastes because extruding a metal would require prohibitive temperatures and pressures to form a thin-wall structure from a high temperature alloy such as iron-chromium. Powder processing of metals also has its drawbacks, in that on such a fine scale, the reactivity of metals may produce explosive conditions and oxide coatings that form during processing become a major contamination because of the powder's high surface are to volume ratio. Also, the particle sizes of metallic powders are typically much larger than their oxide counterparts, making it more difficult to produce pastes as well as to extrude fine walled honeycombs with several grains across the thickness.

Both the art and science of extruding simple and extremely complicated forms from oxide pastes have been around for many years. Oxide powders are generally in their most inert state and they can easily be processed into fine, high quality, well-mixed powders with minimal impurities. As a result, reducing oxide honeycomb pre-forms to the metallic alloy is the optimal way to produce metallic honeycomb structures.

However, the kinetics of the reduction and sintering processes is not known quantitatively at this time. Previous work [6] has shown that the iron-chromium steels produced by this technique do so in two stages. The first involves the reduction of the iron oxide to iron. This stage is believed to be complete before the second stage occurs. The second stage involves the reduction and dissolution of the chromium oxide that remains with the reduced iron matrix. This research is concerned with the second stage and will examine the mechanisms and factors affecting the chromium oxide particle reduction in the pre-reduced iron matrix of iron-chromium honeycombs.

CHAPTER 2

BACKGROUND

The reduction of iron and chromium oxide has been extensively studied over the years, both separately [7-12] and as alloys [6], [13-17]. Several factors need to be considered when the oxide mixture is reduced. Iron oxide reduces to form iron at a much faster rate and at a lower temperature and higher oxygen partial pressure than chromium oxide reduces to form chromium. It has been observed that the iron oxide completely reduces to iron before the chromium oxide begins to reduce [6, 14].

When iron oxide reduces, it tends to follow the reduction path shown below:

$$Fe_2O_3 \rightarrow Fe_3O_4 \rightarrow FeO \rightarrow Fe \qquad [2.1]$$

The Ellingham diagram [18] Figure 2.1 shows that all the successive oxidation reactions of iron going to Fe_2O_3 are well above the reaction of chromium to Cr_2O_3 so that thermodynamically chromium would more favorably oxidize than iron. Conversely, this means that the reverse, the successive reduction of Fe_2O_3 to Fe is more favorable than the reduction of Cr_2O_3 to chromium and so iron oxide reduction should be complete before chromium oxide reduction begins.

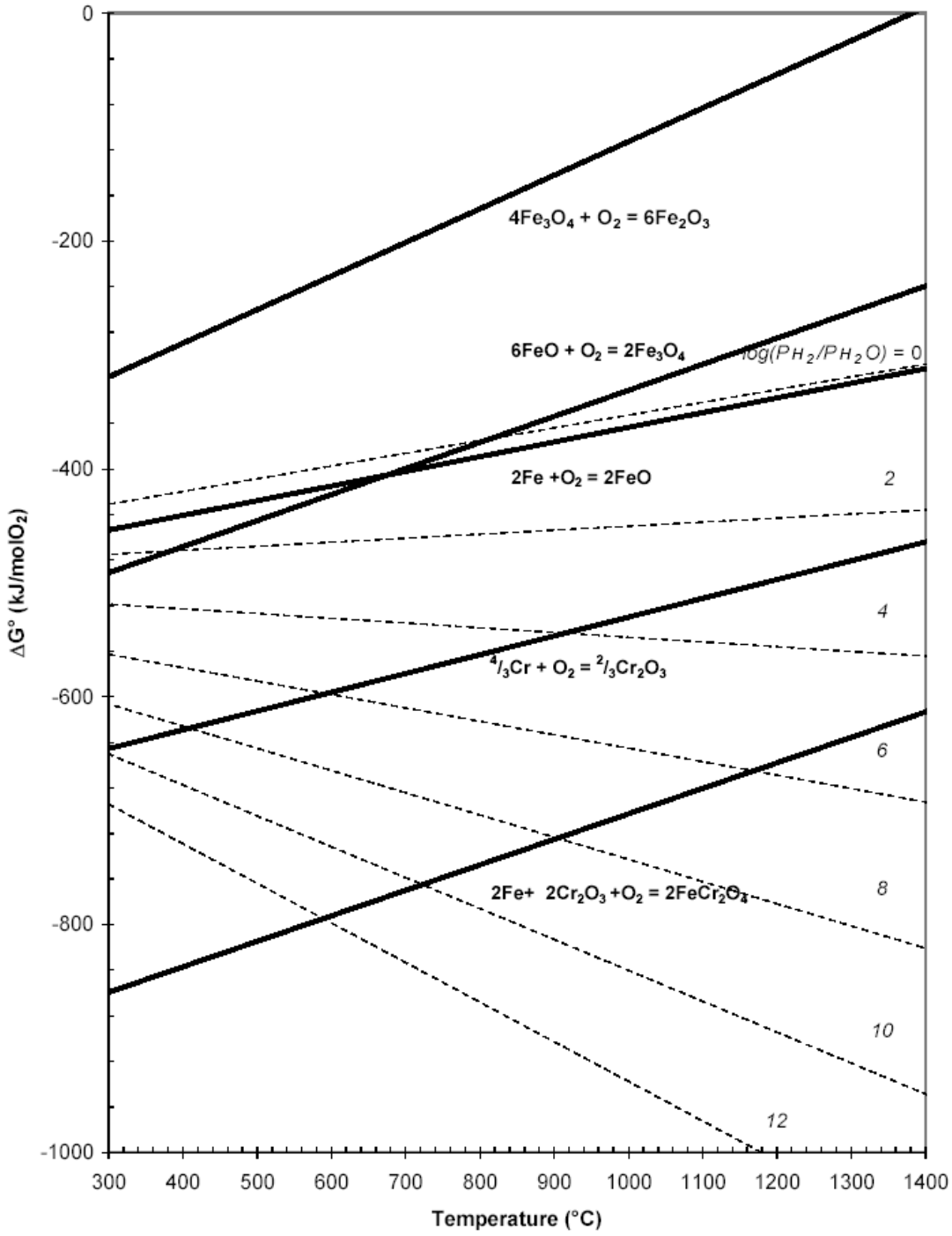

Figure 2.1: Ellingham diagram, compiled with data from different sources [19, 20], showing the standard free energy ($\Delta G°$) of the formation of Cr_2O_3, $FeCr_2O_4$ and the stages of formation of Fe_2O_3 with temperature. Thin dashed lines represent equilibrium for the formation of H_2O at different P_{H_2}/P_{H_2O} ratios.

In the proposed research and in the work of Nadler [6, 16, 17, 21], the oxides are reduced using H_2 gas as a reducing agent. The various reduction reactions thus proceed as follows:

$$M_2O_3 + 3\ H_2 \rightarrow 2M + 3\ H_2O \qquad [2.2]$$

where M is either the iron or chromium metal in this equation.

For the reaction in equation [2.2] to go to completion, the flow of H_2 in and the removal of H_2O throughout the oxide need to be permitted. The extruded and dried iron oxide/chromium oxide body is very porous. The porosity in the samples allows for transport of the reactant and product gases throughout the oxide. Upon the complete reduction of the iron oxide to iron, however, sintering initiates in the reduced metal. The resulting densification produces a reduction in of porosity and therefore a reduction of the free transport of H_2 and H_2O gases. Transport of these gases therefore has to occur increasingly by diffusion through the iron matrix. Diffusion of the gases could occur through the bulk or via grain boundaries. As the iron matrix is polycrystalline and the gaseous molecules are somewhat large (on the order of 0.1 nm), it is thought that diffusion to and from the chromium oxide particles occurs primarily by grain boundary diffusion. Coincidentally, the chromium oxide particles tend to lie along the iron grain boundaries.

2.1 Iron Oxide Reduction

Reduction of iron oxide to produce metallic iron has been performed for many centuries using several methods. Some of these methods include iron reduction by carbon in air (which is the oldest known method) [22, 23], as well as by carbon in an inert atmosphere and, of course, by hydrogen [12].

Additions of other materials, particularly certain oxides, can affect the reduction of iron oxide. El-Geassy studied the roles that CaO and MgO play in iron oxide reduction [7, 8]. These materials promote porosity and therefore increase the free transport of gaseous products and reactants of the reduction reaction of the oxide. Also according to Khalafalla, *et al.*, CaO also renews itself in the reduction process, thus becoming essentially a catalyst for oxide reduction [11]. Gleitzer [9] and Gougeon, *et al.*, [10] both discuss how doping with an alkali such as potassium accelerates the reduction of iron oxide even in very small amounts. Also, according to experiments done on nanocomposite powder mixtures by Laurent, *et al.*, it is interesting to note that Cr_2O_3 is an oxide that performs better than others in helping ensure that the iron oxide is fully reduced [24]. They found that when they partially reduced various oxide mixtures, no Fe^{3+} ions were found in the metal oxide product alloyed with just Cr_2O_3.

In the scope of this investigation, however, the assumption is made that the iron oxide is completely reduced to iron and only the kinetics of the subsequent reduction of the chromium oxide will be studied. Under hydrogen, iron oxide is completely reduced to iron by 600°C [25, 26]. This is also shown by the dilatometer study performed by Nadler [6] and corresponding phases (shown with arrows) in Figure 2.2.

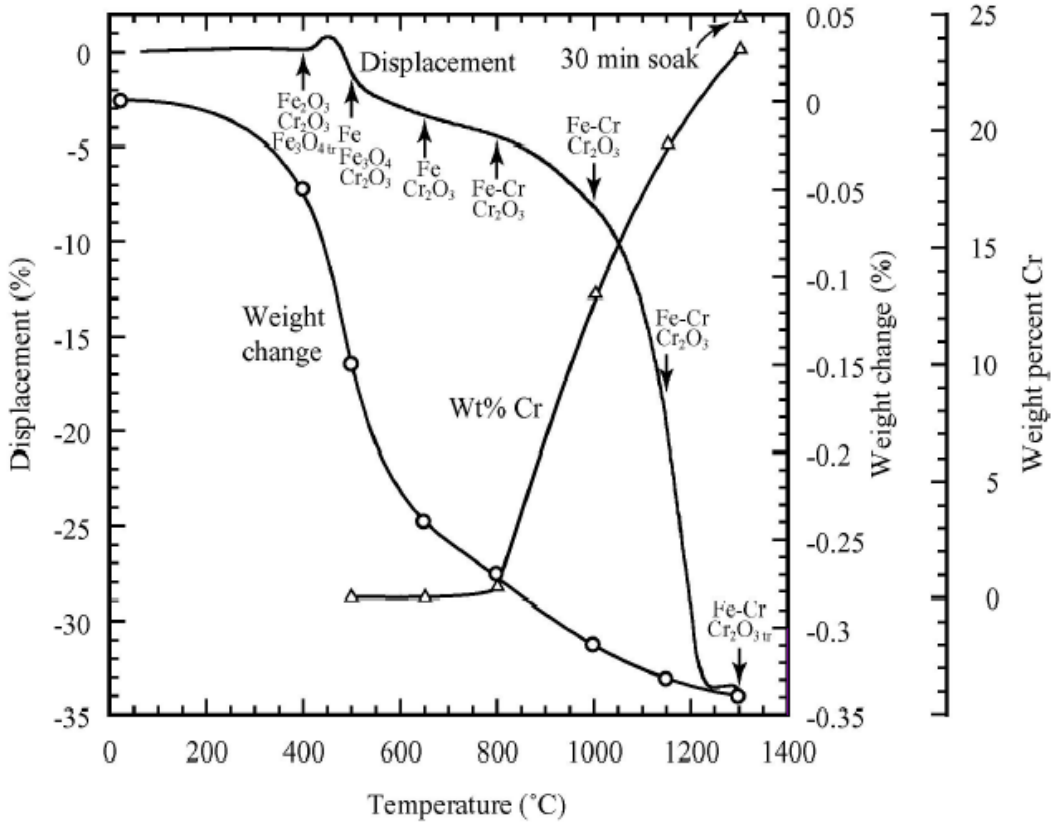

Figure 2.2: Displacement, weight loss, and concentration of chromium in iron-chromium solid solution during the heat treatment of 25 wt% Cr_2O_3 mixtures. Measured weight changes and ss compositions were based on heating to specified temperatures in flowing H_2, followed by furnace cooling in flowing He. Arrows along the displacement trace indicate quench temperatures at which the labeled phases were identified via XRD. Trace amounts are indicated by the subscript “tr" [6].

2.2 Chromium Oxide Reduction

Chromium oxide may be reduced by the use of gaseous reactants [13, 27]. Among these reactants are both hydrogen and carbonaceous gases. Rich [28], Rohn [29] and Alexander [30] have all published patents for chromium oxide reduction by hydrogen. It is very difficult for chromium oxide to be completely reduced by itself under direct gaseous reduction and it is nearly impossible below temperatures of 1300^{o}C to 1400^{o}C [27]. Even at these temperatures low yields are experienced. In fact, instead of reducing the oxide to the metal, using a route that includes other chromium compounds such as carbides and chlorides can be more favorable [27].

Some of the limitations that hinder direct reduction are the relatively high vapor pressure of chromium [31, 32], the dimensions of the sample being reduced, and the amount of water vapor that is present in the reducing atmosphere [27]. The high vapor pressure of chromium [32] is an obstacle to complete reduction because, at the temperatures that chromium oxide reduction takes place, volatile chromium species can be deposited on the oxide, sealing up porous channels and forming a dense metal barrier to reduction [6].

Chromium oxide is in stable equilibrium with only relatively small amounts of water. Ohmi *et al.* actually used a hydrogen atmosphere with water vapor and trace oxygen present, to grow a high quality chromium oxide film on chromium containing alloys. The presence of water vapor in the system caused the growth of the oxide despite the reducing hydrogen atmosphere. In other words, the reverse of equation [2] has taken place. The reducing atmosphere was used to suppress growth of an oxide of poorer quality [33].

It has been shown that chromium oxide reduces more readily when the resulting chromium metal is able to alloy with another metal, in this case iron [14, 16, 27]. The chromium metal produced as the reduction product can then diffuse away from the Cr_2O_3 interface. As a result, the chromium metal does not form a limiting barrier around the oxide and therefore does not seal the particle off from the reducing gas.

2.3 Chromium Oxide Reduction within the Iron Matrix

To determine the best yield of chromium from Cr_2O_3, three possible reduction paths were considered [6, 21]. The first is that these oxides can form a solid solution that is then reduced:

$$(x\text{Fe}, y\text{Cr})_2O_3 + 3\ H_2 \rightarrow 2[x\text{Fe},y\text{Cr}] + 3\ H_2O \qquad [2.3]$$

The second path is that the oxides remain separate, forming no solid solution and reduce together:

$$x\text{Fe}_2O_3 + y\text{Cr}_2O_3 + 3\ H_2 \rightarrow 2[x\text{Fe},y\text{Cr}] + 3\ H_2O \qquad [2.4]$$

The third path assumes that the iron oxide is first completely reduced to iron, and Cr_2O_3 subsequently reduces in the presence of iron metal:

$$2x\text{Fe} + y\text{Cr}_2O_3 + 3y\ H_2 \rightarrow 2[x\text{Fe},y\text{Cr}] + 3y\ H_2O \qquad [2.5]$$

The free energy of the reaction, ΔG_{RXN}, was calculated for each scenario such that

$$\Delta G_{RXN} = \Delta G_{OSS} + \Delta G_{Fe\text{-}Cr} + \Delta G_{RDX} + \Delta G_{H_2O} \quad [2.6]$$

where ΔG_{OSS} is the free energy of mixing the oxide solid solution, $\Delta G_{Fe\text{-}Cr}$ is the free energy of forming the iron-chromium solid solution, ΔG_{RDX} is the free energy of reducing the oxides to the metal and $\Delta G^{o}_{H_2O}$ is the free energy of H_2O formation. ΔG_{OSS} is equal to zero for equations [2.4] and [2.5] since no oxide mixing takes place for these scenarios. For equation [2.5], ΔG_{RDX} is merely the free energy of the fraction of chromium oxide reduced as the iron is already reduced.

The composition of chromium, *y*, for which ΔG_{RXN} is equal to zero is calculated and is the maximum yield of chromium that can be reduced. The results of this calculation for each of these three cases over various H_2 partial pressures have shown that the scenario where completely reduced iron is in the presence of reducing chromium oxide produces the largest maximum yield, *y*, of chromium metal transformed, as shown in Figure 2.3.

Results from experiments measuring the amount of chromium going into solution with the reduced iron metal, compared to starting compositions, show eventual yields that would most likely occur if the third scenario was the mechanism occurring (see Figure 2.4). These results show that yields of up to 50wt% chromium are possible. The calculations (Figure 2.3) show that 50wt% is barely reached by the first two scenarios and even then, only at very high hydrogen partial pressures. As a result, this

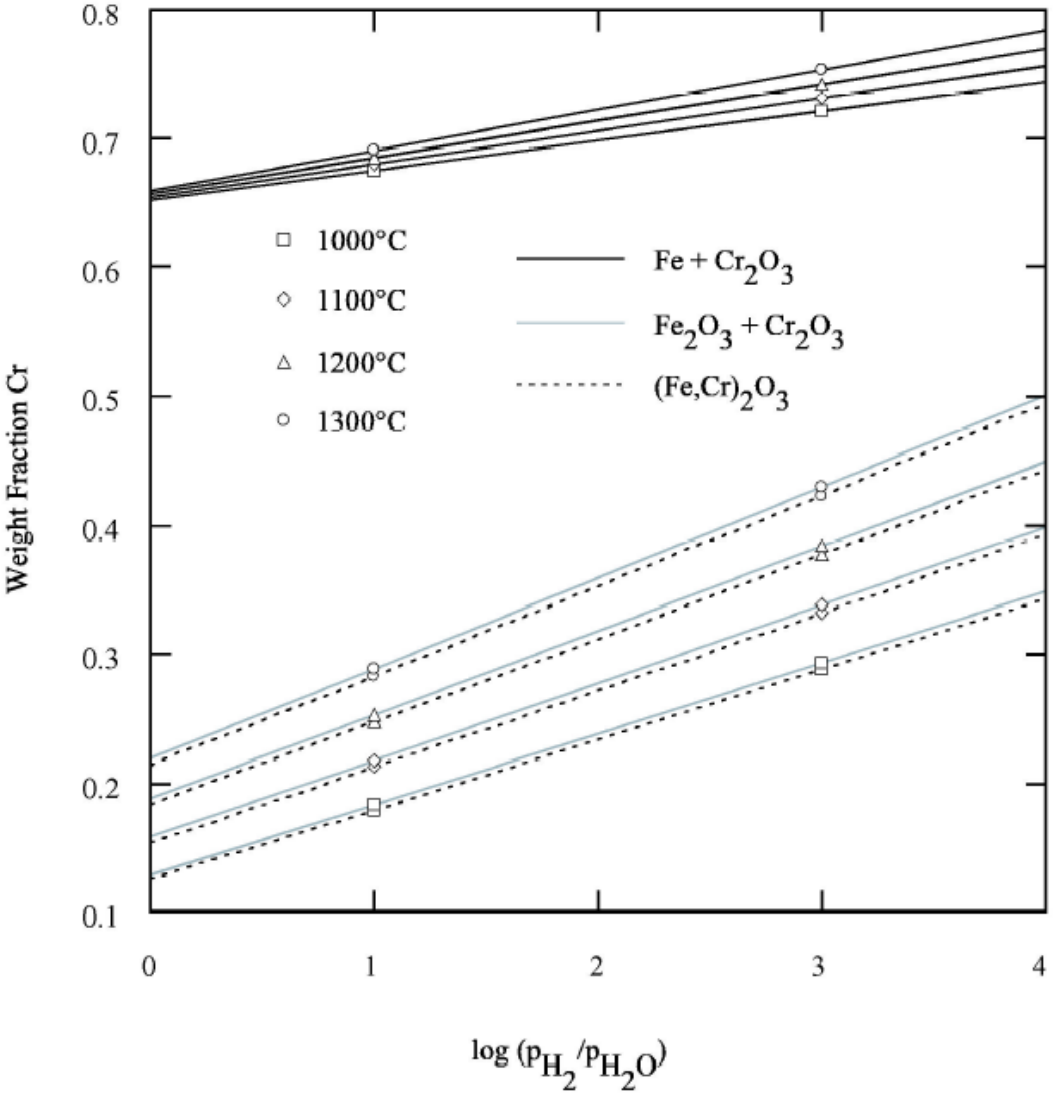

Figure 2.3: $y(\Delta G_{RXN} = 0)$ versus P_{H_2}/P_{H_2O} for initial conditions $Fe+Cr_2O_3$ (Equation [2.5]), $Fe_2O_3+Cr_2O_3$ (Equation [2.4]) and $(Fe,Cr)_2O_3$ (Equation [2.3]). Each condition is shown for four temperatures: 1000, 1100, 1200, and 1300°C [6].

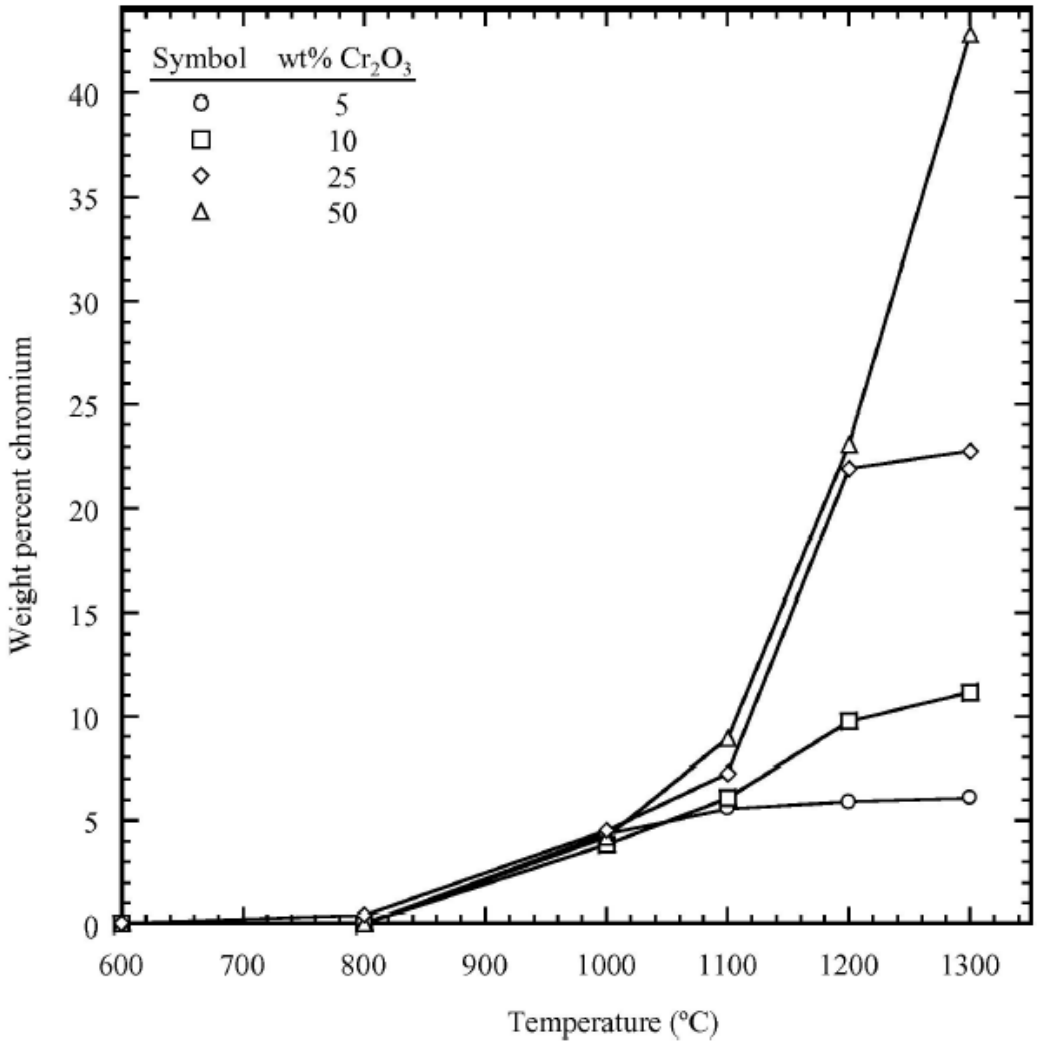

Figure 2.4: Concentration of chromium in iron-chromium solid solution for various compositions as determined via XRD, after quenching at different temperatures [6, 17].

also provides credibility to the assumption that all the iron reduces before chromium oxide reduction proceeds. This will be the main assumption in this research.

As mentioned previously, it is difficult for pure chromium oxide to be fully reduced. It is even difficult for iron/chrome oxide at very high concentrations of chromium oxide to be fully reduced [6]. This is because the volatile chromium species tends to form a sufficiently dense layer over the remaining oxide such that gaseous transport is successfully inhibited, so that no further reaction takes place. In lower chromium oxide concentrations, this does not appear to be a problem. It is thought that this is because chromium metal, when formed, has the opportunity to diffuse away from the chromium oxide/metal interface, through the iron matrix. Since diffusion of chromium through the iron matrix is important to the continued reduction of the chromium oxide particles, the ability of chromium to diffuse through the metal matrix will have an effect on the reduction process. Inter-diffusion coefficients for chromium in iron are shown in Table 2.1

Table 2.1: Diffusivity Data for chromium in α and γ iron [34].

	D_0, mm^2/s	Q, kJ/mol
α Iron	240 +14/-13	239.8 +/-4.2
γ Iron	6.27 +0.46/-0.42	252 +/-18.4

One of the factors affecting the transport of reducing chromium through the iron matrix is the extent of a chromium oxide particle's attachment to the matrix. The

greater the contact area that a particle can have with the matrix, the greater the surface area through which diffusion can occur. This increases the flux of chromium diffusing away from the particle/iron interface. Also affecting the rate of transport of chromium through iron metal is the α/γ transformation that occurs above 840°C (Figure 2.5) [35]. If the ability of chromium to diffuse through the iron matrix has an effect on chromium oxide particle reduction, then the change in chromium diffusivity in this region [34] would also show a marked change in the reduction behavior of the chromium oxide particles. Diffusivities and activation energies of chromium in both α and γ iron are shown in Table 2.1. The more open structure of the α iron allows for a greater diffusivity with respect to γ iron.

The ability of chromium, to diffuse into the iron matrix is a key to continued reduction of chromium oxide. Also important are factors such as porosity, and the gaseous diffusion of both the reactants and products of the reaction through the bulk of the iron matrix. Porosity in the iron matrix allows free gaseous diffusion to and from reducing chromium oxide particles. As the reduction continues at high temperatures, sintering of the iron matrix becomes more prominent. The decreasing porosity implies that there are fewer interconnected channels for gaseous reactants and products to move, which decreases the likelihood of reduction. As a result, the effect of the changing porosity should be evident in the reduction behavior of the chromium oxide particles. As the porosity in the sintering matrix decreases, transport of gaseous reactants and products, occur more heavily through the bulk of the iron matrix. As a result, the effusion of gaseous reaction products should also be influenced by the changing porosity.

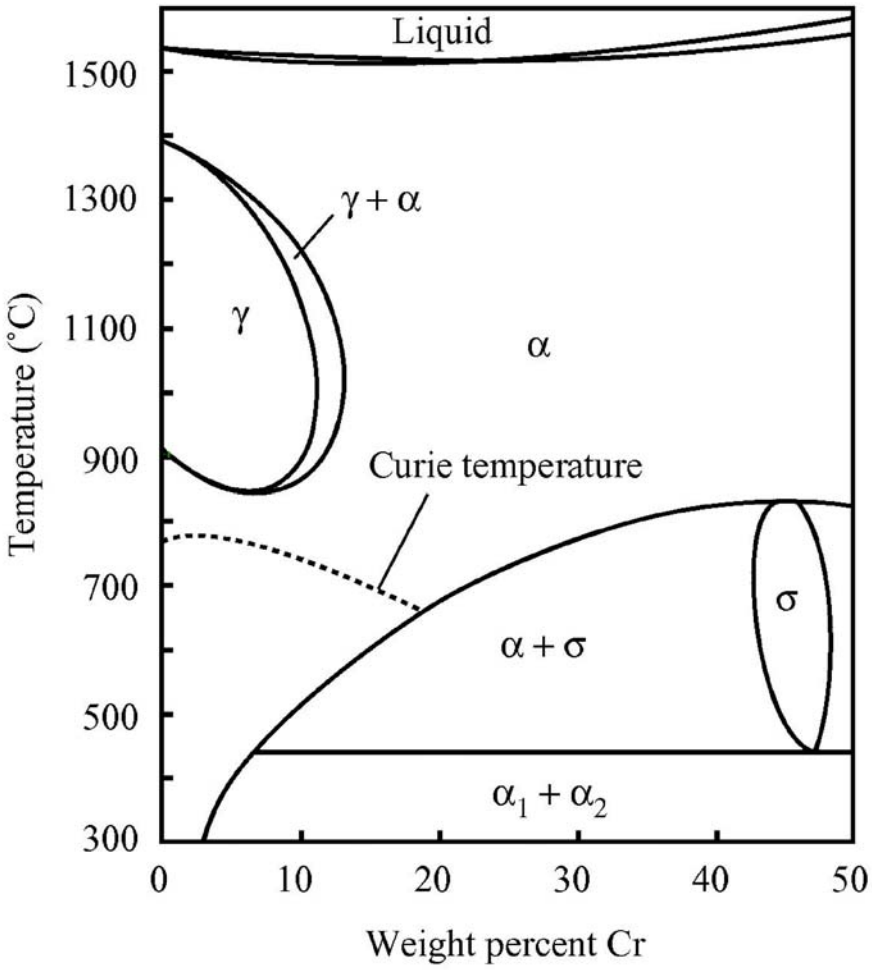

Figure 2.5: Portion of the iron-chromium phase diagram [35], as taken from Nadler [6].

2.4 Sintering

Sintering of the iron matrix occurs by solid-state diffusion. The temperatures that are reached in the scope of this experiment are well below the melting temperature of the alloy (see Figure 2.5), so no liquid phase sintering is expected. The binder additives used in preparing the extrudate do enhance its green strength, but since it decomposes and is burned off above 250^{o}C [3], the effects that it may have on the sintering of the reduced iron is ignored even though the carbon monoxide and carbonaceous char released upon decomposition of the binders is known to promote reduction [6].

The iron matrix in this work is considered to start sintering by about 600^{o}C. The initial stage of sintering is generally thought to occur at 20-40% of the melting temperature of the powder, which would be around 310^{o}C to 620^{o}C, (see Figure 2.5). Work by Salak on iron powder compacts show that initial inter-particle bonds start forming above 400^{o}C [36]. In this work, however, it is at 600^{o}C that the iron oxide is fully reduced [6]. As a result, sintering of the iron is considered to take place at this temperature when the iron becomes available, (see Figure 2.2). Sintering of iron powder does not really start to produce a substantially dense structure until about 900^{o}C [36]. The majority of the inter particle bonds (necking) occurs by 800^{o}C, but the number and size of the necks and therefore strength of these specimen increase significantly beyond a temperature of 875^{o}C [36]. (See data set (3) in Figure 2.6).

For substantial densification to occur during sintering, diffusion must not only take place over the surface of sintering particles but also from within the bulk of the particle itself. The transport mechanisms that support densification are grain boundary diffusion and lattice diffusion [5, 31]. This is primarily why most of the densification

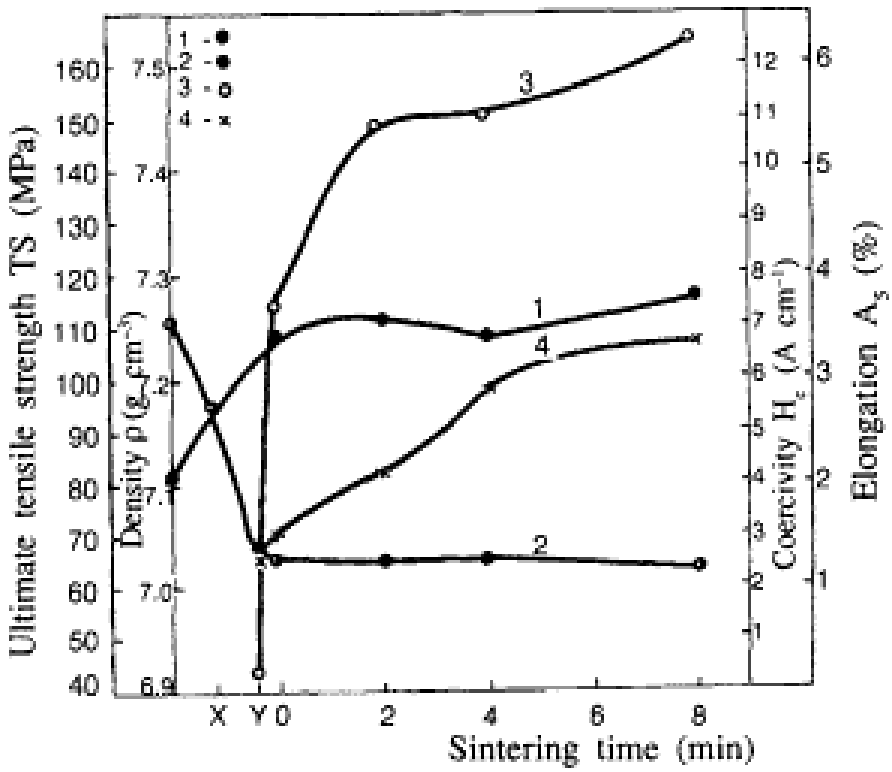

Figure 2.6: Dependence of 1) density, 2) coercivity, 3) tensile strength, and 4) elongation of specimens on sintering time at 875°C in hydrogen. On the Sintering time axis X is the time the specimen reached 400°C and Y is the time the specimen reached 800°C [36].

takes place in the second stage of sintering. Vacancies diffuse away from pores within the bulk causing them to shrink and the whole sample to densify. This stage is different from the first stage of sintering where necking between particles and surface smoothing occur.

In iron, sintering is initially dominated by surface diffusion and then subsequently by grain boundary diffusion [37]. To enhance densification during the sintering process, higher temperatures are desired in order to activate volume diffusion. The α to γ transformation at these higher temperatures (see Figure 2.5) inhibits sintering, though, which is the result of the decrease in diffusivity after phase transformation (see Table 2.1). Increasing chromium content in the iron matrix as the chromium oxide particles reduce may likely affect the sinterability of the iron matrix because the chromium composition affects the α to γ transformation.

2.5 Non-Isothermal Sintering

As will be discussed in a later section, the reduction in hydrogen atmosphere will take place under a constant heating rate. The majority of sintering studies are performed isothermally. Non-isothermal sintering may enhance densification as the heating rate may play a role in minimizing the effects of surface diffusion. Surface diffusion does not contribute to densification [38-40] but hinders the densification process by reducing the surface area and curvature of the particles, thereby removing the driving force for densification. As a result, coarsening rather than densification takes place. The reduction of surface area and curvature serves as a driving force for both densification and coarsening [5, 31, 37-39]. If surface diffusion is suppressed, then

the driving force for sintering still remains and is not spent in the competing process of coarsening. It is also proposed that the presence of a heating rate makes the sample more "flexible" [41]. Under isothermal conditions, the diffusion coefficient reaches a constant value and chemical equilibrium is established. The sample is more rigid and resistant to the flow of particles. Under non-isothermal conditions the constantly changing diffusion coefficient inhibits this equilibrium state thus increasing the ability of the sample to densify. The driving force for sintering is not increased with non-isothermal sintering, but the "rigidity" of the sample is decreased.

Roura *et al.* [40] calculated linear shrinkage rates for copper powder compacts heated at various rates, from the equations provided by Ashby *et. al.* [42, 43]. Their results, shown in Figure 2.7, show that faster heating rates produce faster shrinkage rates and therefore faster densification rates. Also noteworthy are calculations for shrinkage rate, made over heating schedules where powder compacts are heated at constant heating rates to various temperatures and are then held isothermally. These results show a sharp drop in shrinkage rate as the isothermal temperatures are reached. (See Figure 2.8).

The calculations by Roura *et al.* are corroborated by experimental data from Haglund *et al.* [41, 44] (see Figures 2.7 and 2.8). Their shrinkage rate was calculated from the equation

$$y' = \sum \frac{V_i}{\pi x^2} \qquad [2.7]$$

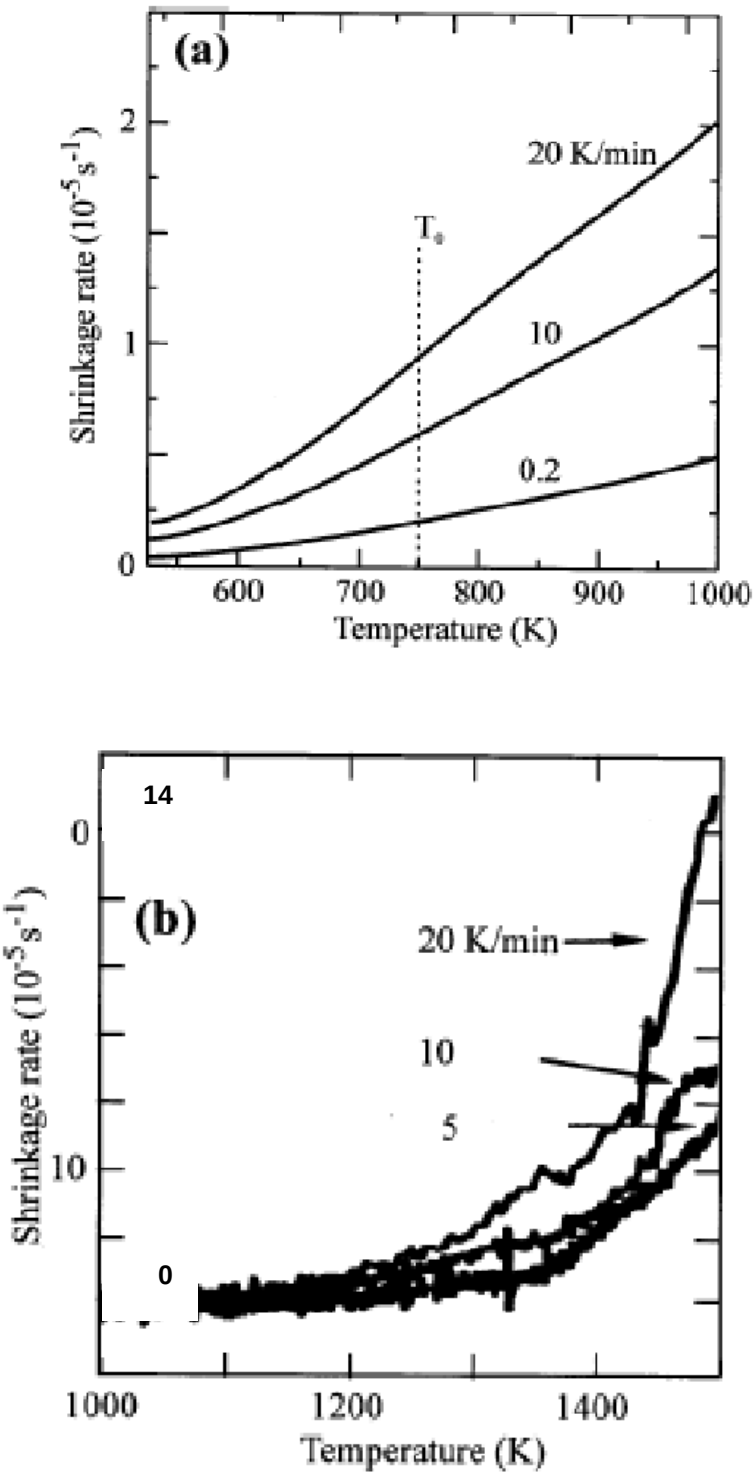

Figure 2.7: Figure (a) shows the calculated linear shrinking rate vs. temperature during heating at several constant rates [40]. Figure (b) shows shrinkage curves for three carbide samples heated at different heating rates [44].

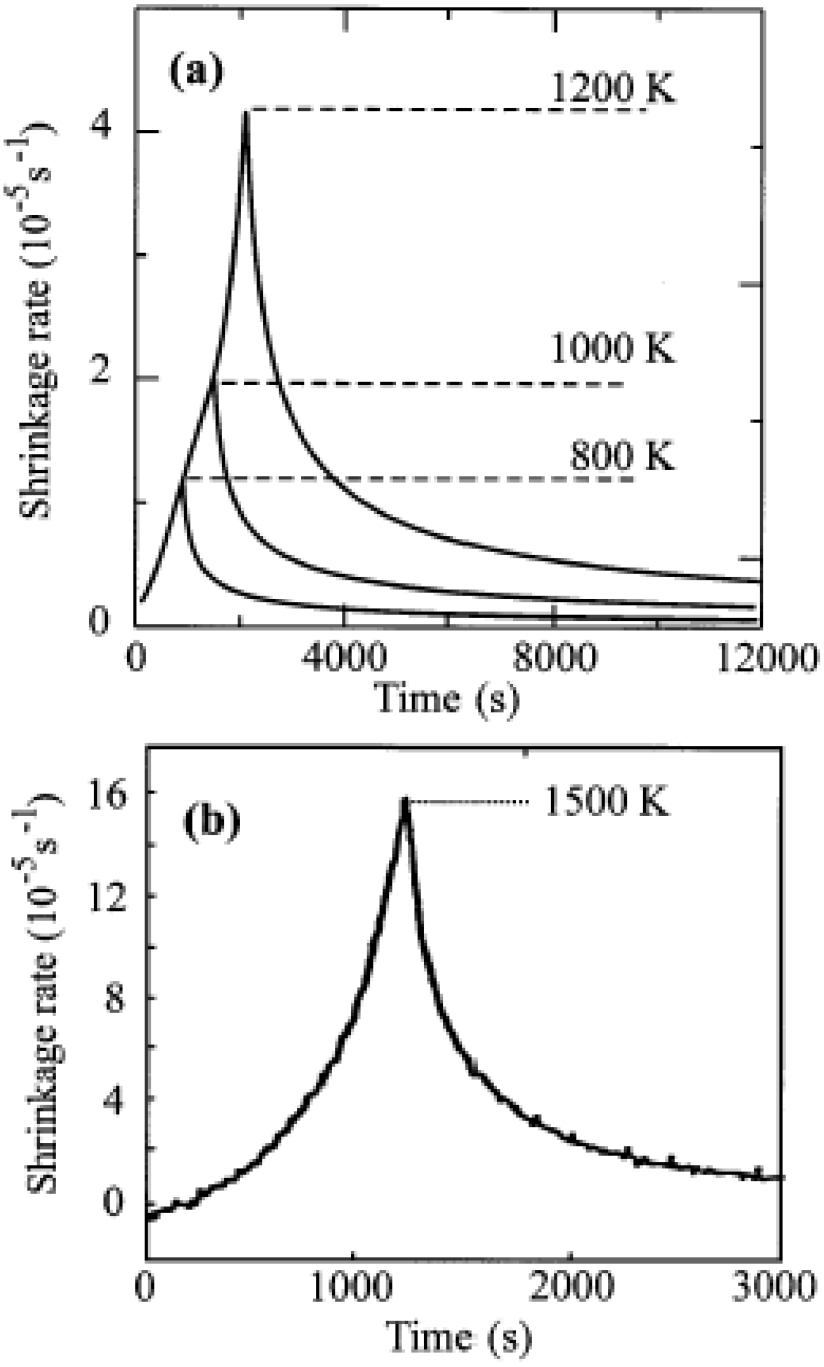

Figure 2.8: Figure (a) shows the calculated linear shrinking rate vs. time during heating at 20K s^{-1} up to several isotherms [40]. Figure (b) shows a shrinkage rate curve for a carbide sample heated at the same rate to 1500K then quenched [41].

where y' is the shrinkage rate and V_i is the flux of vacancies or atoms (diffusion) for different mechanisms i. The contributions from the different diffusion mechanisms that produce densification, grain boundary diffusion and lattice diffusion, are summed [42, 43]. The contributions from the diffusion mechanisms can be written as

$$V_i = D_i(T)\, f_i(\xi, T, T') \qquad [2.8]$$

where D_i is the diffusivity for each mechanism and f_i is a function of the state of the compact [40]. At any given temperature D_i is the same regardless of heating history so is not dependent on T', the heating rate. However, f_i will be dependent on the heating rate and not temperature. This is in spite of the fact that f_i is temperature actually through the dependence on the materials parameters on temperature. This is acceptable because the temperature dependence of V_i relies primarily on D_i, therefore the dependence of f_i on temperature can be ignored [40]. The equation can be written

$$V_i = D_i(T)\, f_i(\xi, T') \qquad [2.9]$$

showing that the flux of vacancies, V_i, is highly dependent on the heating rate.

In addition to the decrease in the rate of shrinkage upon switching form non-isothermal to isothermal heating, a temporary reversal of shrinkage may be experienced in the isothermal stage. This is indicated by an increase in porosity. One such example is shown in the work of Schoeler *et al.* [45]. Heat-treated molybdenum-alloyed steels were held isothermally at temperatures of 700°C and 1100°C after a constant heating

rate and Schoeler *et al.* observed this trend as seen in Figure 2.9. The value on the porosity % axis indicates the green body porosity before heat-treatment begins. The zero time value denotes the porosity of the sample at the end of the heating at a constant heating rate and the beginning of the isothermal hold. The time given is the time that the sample is held isothermally. Figure 2.9 shows an increase in porosity after the start of the isothermal heating for both the 700°C and 1100°C holds. The increase in porosity appears earlier in the 700°C sample than it does in the 1100°C sample.

The neck growth equations of Ashby *et al.* [42, 43] are used in this study in a manner similar to Roura *et al.* [40] to model the sintering behavior of the reduced iron matrix, though more emphasis is placed on using all of the sintering mechanisms. The unique characteristics of the iron compact that occurs as a result of the oxide being reduced to the metal are taken into account in this model. The sintering rate of a compact is highly dependent on the particle size of the powder. The smaller the particle size, the shorter the sintering time to densification. The interfacial processes of surface diffusion and grain boundary diffusion are most affected by the particle size because of the high interface area per unit volume that smaller particles have. Volume diffusion is less sensitive to the particle size because the surface area to bulk ratio is not a major factor in the mechanism.

After reduction of the iron oxide, the metallic iron forms into agglomerates made up of smaller particles. Therefore, two size classes of sintering spheres are considered. As a result of the particle size dependency of the sintering rate of a compact, two sintering regimes are experienced for a compact of agglomerates. The smaller particles within the agglomerates sinter faster, while the agglomerates

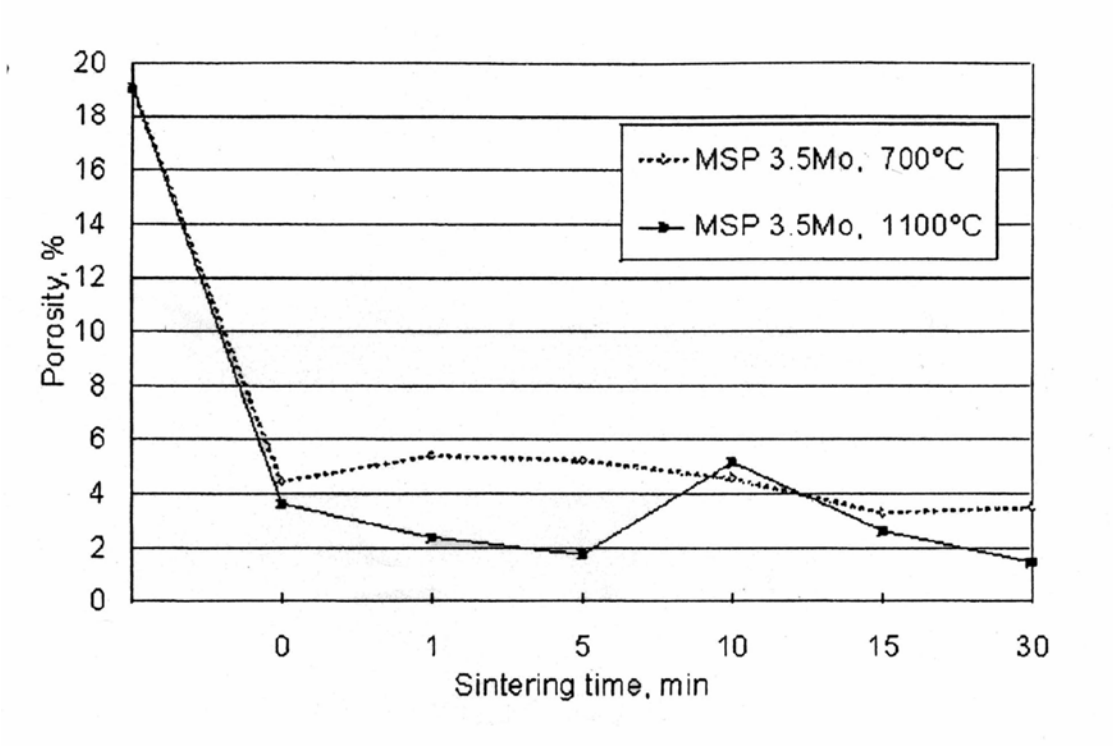

Figure 2.9: Porosity versus isothermal sintering time for a molybdenum-alloyed steel for hold-temperatures of 700°C and 1100°C. The sintering time axis measures the length of isothermal heating. The porosity of the green body before heating to the isothermal temperature is recorded on the porosity axis [45].

themselves, sinter at a slower rate (see Figure 2.10). The two rates of sintering take place concurrently. Appendix A contains details of the equations used to set up of this model.

The linear shrinkage rate of the sample can be related to its densification and as a result the reduction in porosity [46, 47]. Shrinkage can be related to densification by the equation

$$\rho_{rel} = \frac{\rho_o}{\rho_{th}} \times \left[1 - \frac{\Delta L}{L_o} \right]^{-3} \qquad [2.10]$$

where ρ_{rel} is the relative density, ρ_o is the original density ρ_{th} and is the theoretical density for the iron matrix and $\Delta L/Lo$ is the shrinkage. The fractional porosity P_p can be easily related to the relative density by the equation

$$\rho_{rel} + P_p = 1 \qquad [2.11].$$

By modeling the sintering behavior through tracking the linear shrinkage that results, the state or the compact can be determined.

2.6 Dissolution Modeling

In the scope of this research, the elimination of chromium oxide particles as chromium dissolves into the iron matrix will be studied. The oxide particles are not being dissolved into the iron matrix directly, but the reduction product, chromium

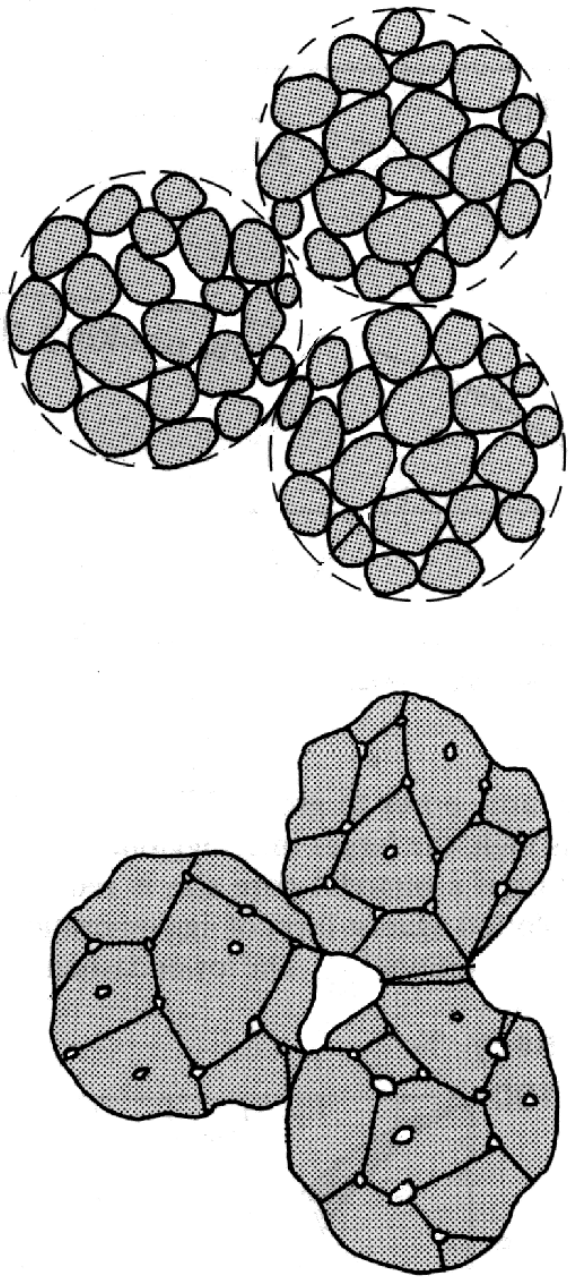

Figure 2.10: Representation of the sintering of agglomerates made up of smaller particles. The two particle regimes produce concurrent sintering at two different rates. This figure is adapted from German [31].

metal, is being reduced from the oxide particle and diffuses into the iron matrix. Consequently, the reduction of the chromium oxide particles to form chromium and their subsequent diffusion of chromium into the iron matrix must both be understood to formulate a dissolution model. Dissolution occurs when particles of a second phase dissolve and become incorporated into the more stable matrix, (see Figure 2.11). The particle-matrix interface recedes toward the center of the particle as the particle is eliminated, (see Figure 2.12). The rate of particle dissolution can be limited by either the rate of diffusion in the matrix (diffusion control) or the rate of reaction occurring at the interface (interface control) [48]. Diffusion control will be discussed first.

Dissolution kinetics is diffusion controlled when the rate at which solute can be transported away from the particle/matrix interface is the limiting step. This is usually the governing theory of dissolution, especially when the dissolving particles are still relatively large. The surface energy of the larger particles is such that atoms can more readily make the jump across the interface from these particles into the matrix.

Modeling a diffusion controlled transformation of an isolated particle in an infinite matrix requires that the following field equation be solved [49]:

$$D\nabla^2 C(r,t) = \frac{\partial C(r,t)}{\partial t} \qquad [2.12]$$

where D is the diffusion coefficient in the matrix and C(r,t) is the concentration field surrounding the particle at time t and a distance r away from the position of the particle. The following boundary conditions must also be satisfied.

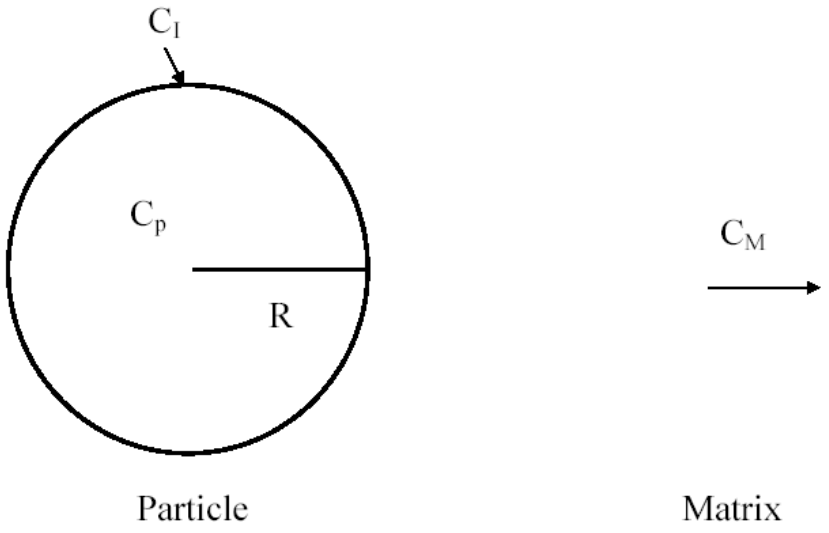

Figure 2.11: Representation of a chromium oxide particle in an iron matrix, with concentrations in and around the particle indicated.

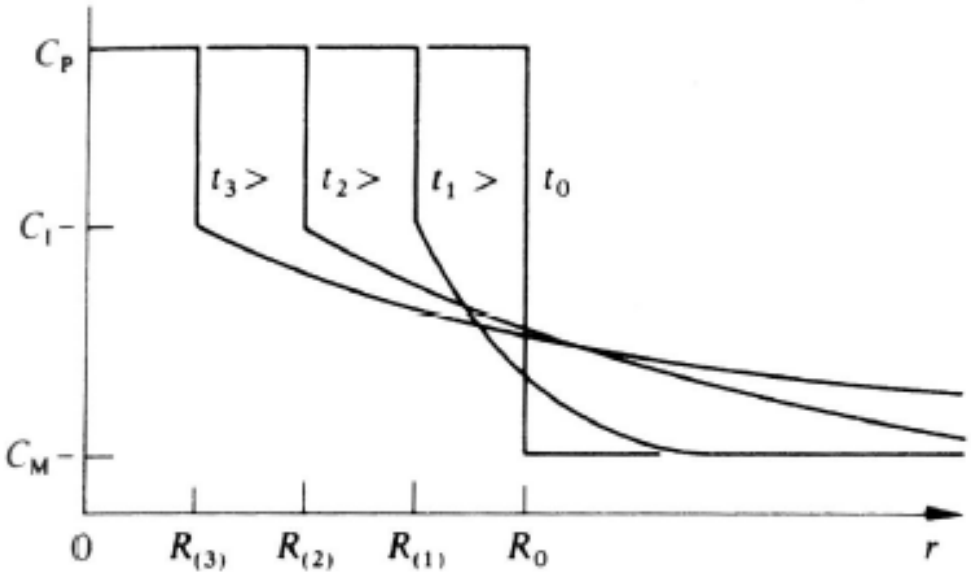

Figure 2.12: Evolving concentration profile of dissolving particles. C_p is particle composition, C_M is the composition of the matrix, C_I is the concentration at the interface and R is the particle radius [49].

$$C(r = R,t) = C_I \qquad 0 < t \leq \infty \qquad [2.13]$$

$$C(r,t = 0) = C_M \qquad r \geq R \qquad [2.14]$$

$$C(r = \infty,t) = C_M \qquad 0 \leq t \leq \infty \qquad [2.15]$$

$$\frac{\partial C(r,t)}{\partial r} = 0 \qquad r = 0;\ t \geq 0 \qquad [2.16]$$

$$\frac{\partial C(r,t)}{\partial r} = 0 \qquad r = \infty;\ t \geq 0 \qquad [2.17]$$

The following independent flux balance must also be satisfied if one is to allow for a moving interface.

$$\frac{(C_P - C_I)dR}{dt} = D\frac{\partial C(r,t)}{\partial r}\bigg|_{r=R} \qquad [2.18]$$

Here r = R (the radius of the particle) at the particle-matrix interface, C_I is the concentration of the matrix at that interface and C_M is the composition of the matrix far away from the particle. C_P is the composition of the particle that is assumed to be constant, independent of r and t.

To produce representative dissolution data with the framework of the particle array, the Murray-Landis [50] transformation is used:

$$dC_n/dt = \partial C_n/\partial r_n\,(dr_n/dt) + \partial C_n/\partial t \qquad [2.19]$$

which is the rate of change of concentration at a point n for a particular particle and

$$dr_n/dt = r_n/R(t)\ (dR/dt) \qquad [2.20]$$

which is the rate of travel of n relative to the interface velocity. R(t) is the position of the interface at time t and dR/dt is the interface velocity.

Interface controlled kinetics is a result of a slower interface reaction. In smaller particles this tends to take on more of a major role. Interface controlled kinetics also tends to be slower than diffusion controlled kinetics [48, 49, 51].

In any real system, several particles make up the distribution in the matrix. Therefore, dissolution models have been put forth [49, 50] that relate the previous equations to real systems by the use of particle arrays (Figure 2.13). The main assumptions when using particle arrays are that 1) all particles have the same size; and 2) they are all uniformly spaced within the matrix. This is not the case in real systems, but is a simplification. It is important to note that when employing a finite framework such as a cell array, the condition in equations [15] and [17] where $r = \infty$, physically translates to $r = L$, where L is some finite length that is the limit for the structure of the array. For the dissolution of spherical particles L is given by

$$L = \frac{R_o}{\sqrt[3]{y}} \qquad [2.21]$$

where *y* is the total fraction of chromium relative to iron in the sample. See Section 2.3.

Most dissolution treatments utilize dissolution control kinetics. Since dissolution of the chromium oxide particles does not occur directly but the outer layer

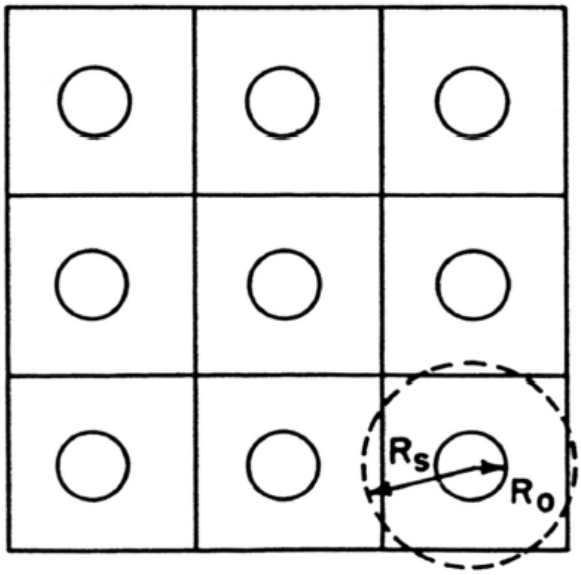

Figure 2.13: Representation of 2-D array of cells used to model a distribution of dissolving particles. R_0 is the original particle radius and R_s is the radius of a sphere with equivalent volume of the cell. [51]

reduces first to the metal, which is then diffused into the iron matrix, the mechanisms involved could possibly include an interface-controlled aspect to it. Nolfi *et al.* has put forth an analysis that treats both limiting cases as well as mixed control [51]. To determine whether dissolution was diffusion or interface controlled, they calculated the parameter σ:

$$\sigma = \left[\left(\frac{KR}{D} \right) + 1 \right]^{-1} \qquad [2.22]$$

where K is a reaction rate constant, and D is the solute diffusivity in the matrix. In this case, the diffusivity of Cr in Fe, and R is the radius of the particle. When σ is zero, then dissolution is diffusion controlled. When σ is unity, it is interface controlled. At intermediate values both diffusion and interface control operate, so dissolution is referred to as mixed control.

Previous studies of modeling dissolution in this system [6] have assumed that there is equilibrium at the interface and thus diffusion-controlled kinetics is dominant, i.e., it was assumed that σ = 0. As mentioned earlier, both gaseous and Cr diffusion are important and may be limiting factors in the dissolution of the reducing chromium oxide particles. Also the reduction reaction of chromium oxide to chromium at the particle matrix interface itself may be a limiting factor. As a result, mixed control is an important aspect that should be considered.

Other assumptions made in the Nadler study include the mixture of a uniform distribution of chromium oxide particles in the iron matrix and that porosity and grain

boundary features are irrelevant. However, the sintering of the iron matrix is likely to cause particles to lie in a non-uniform distribution, primarily on grain boundaries. Measurements of chromium oxide particle size and spatial distributions obtained at various stages in reduction would provide insight of the true distributions and allow a more realistic model to be developed. Composition profiles of Cr away from the reducing chromium oxide particles will provide diffusivity data that would already include the effects of porosity, grain boundaries and other features existing in the iron matrix. This would provide more accurate data for input into a dissolution model.

The diffusivity data will be calculated from the composition profiles using the Boltzman-Matano analysis [52, 53] shown in the following equation:

$$D = -\frac{1}{2t} \cdot \frac{\partial x}{\partial N_A} \int_{N_{A_0}}^{N_A} x dN_A \qquad [2.23]$$

where D is the diffusivity, x is the distance away from the chromium oxide particle/iron matrix interface, N_A is the composition at x, N_{A0} is the composition at $x = 0$, and t is the isothermal time.

The diffusivity data obtained for input into the model will be primarily for ascertaining a time scale. In the case of particles dissolving under isothermal conditions, the shape of the dissolution curves and the composition profiles are the same. Only the time over which dissolution occurs varies. A non-dimensional time, τ parameter is used in the modeling program. It is related to actual time by the diffusivity coefficient and the original particle radius.

$$\tau = \frac{Dt}{R_o^2} \qquad [2.24]$$

2.7 Summary

In the production of iron chromium alloy honeycombs, the oxides of both metals are mixed with water, binders and lubricants and formed at room temperature into the desired shape. Complete oxide reduction is desired in order to produce a high quality product. Deleterious effects are commonly the result of the presence of unreduced oxide inclusions. Reduction of the oxide mixture occurs such that the iron oxide is reduced completely to the metal before chromium oxide reduction begins. The residual chromium oxide particles are then reduced and the chromium metal incorporated into the iron matrix. The focus of this work is to study the reduction and elimination of the residual chromium oxide particles and the environment in which this occurs.

Chromium oxide reduction is aided by its coupling with the iron matrix because this allows the transport of the reduced chromium metal through the matrix away from the oxide particle. The ability of hydrogen and water vapor to be transported through the iron matrix to and away from the chromium oxide particle, respectively, also affects the process of chromium oxide particle reduction. The gaseous transport through the iron matrix is affected mostly by the porosity contained within the iron matrix and as chromium oxide reduction takes place, the iron matrix is concurrently sintering. As a result the porosity of the compact is also decreasing. Consequently, the ability of the

gaseous reactants and products to be transported is affected. The environment in which reduction takes place is changing. The densification of the iron matrix achieved during the sintering process is affected by the heating rates that the sample undergoes. Models of the processes of the dissolution of the chromium oxide particles and of the sintering of the iron matrix are presented.

CHAPTER 3

MODELLING

As established earlier, iron oxide is reduced before chromium oxide, forming residual chromium oxide in an iron matrix. Continued heat-treatments in hydrogen after iron oxide reduction have two effects. The iron matrix undergoes sintering and the chromium oxide particles reduce and are dissolved into the matrix. Models were used in this study to compare predicted results with experimental data and to help understand both of these processes. These models were adapted from existing sintering [42, 43] and dissolution [48, 49, 54] models. The set up and parameters of both models are given below.

3.1 Sintering Model

The equations in the following sections govern the sintering of an aggregate of spheres. These equations were taken from Ashby *et al.* [42, 43]. Model parameters with typical values are given in the Table 3.1. Most of the values are taken from Swinkels and Ashby [43], but the values for lattice diffusion was taken from Alberry and Haworth [34]. In their model the sintering behavior is broken up into three stages: stage 0, stage 1, and stages 2 and 3 (considered a single stage).

Table 3.1 Model parameters used in the equations presented by Ashby *et al.* [42, 43] that model sintering behavior for a compact of spheres.

Parameter	Description	Values for iron and nickel		
		α	γ	Ni
a	Initial particle radius (m)	5 to 10 μm		
x_0	Initial neck size (m) (radius of disc connecting two particles)	This is a function of the initial particle size (see equation (1))		
x	Neck size radius (m)			
x_f	Final neck size (m)	0.74a		
$\dot{x}$	Neck growth rate (m/s)	See equations (12) & (16)		
y	Half of the interpenetration distance between two particles (m)	See equation (13)		
$\dot{y}$	Shrinkage rate (m/s)	See equation		
γ_s	Surface free energy (J/m^2)	2.1	2	2
μ	Shear Modulus (N/m^2)	6.4E+10	8.1E+10	7.65E+10
Ω	Atomic Volume (m^3)	1.18 E-29	1.21 E-29	1.09 E-29
Δ_0	Theoretical density (kg/m^3)	7620	7650	8900
K_1, K_2, K_3, K_m	Curvatures (m^{-1})	See equations (9) – (11) & (17)		
$\delta_s D_s$	Surface diffusion coefficient multiplied by the effective thickness (m^3/s)	$\delta_s D_{s0}$ = 2.5E-9 Q = 232 kJ/mol	$\delta_s D_{s0}$ = 1.1E-9 Q = 220 kJ/mol	$\delta_s D_{s0}$ = 4.4E-11 Q = 199 kJ/mol
$\delta_g D_g$	Grain boundary diffusion coefficient multiplied by the effective thickness (m^3/s)	$\delta_g D_{g0}$ = 1.12E-12 Q = 174 kJ/mol	$\delta_g D_{g0}$ = 7.5E-14 Q = 159 kJ/mol	$\delta_g D_{g0}$ = 3.5E-15 Q = 115 kJ/mol
D_v	Bulk diffusion coefficient (m^2/s)	D_{v0} = 2.4E-4 Q = 239.3 kJ/mol	D_{v0} = 6.27E-6 Q = 252 kJ/mol	D_{v0} = 6.0E-5 Q = 271 kJ/mol
N	Dislocation density (m^{-2})	1E-14 (approximate)		
ρ	Radius of curvature of the neck (m)			
k	Boltzman's Constant (J/K)	1.38 E-23		
R	Gas constant (J/K)	8.314		
T	Temperature (K)			

3.1.1 Stage 0

When particles are packed, inter-atomic forces between them cause small necks to form. The rate of this neck growth is so rapid and the final neck size is so small that for the purpose of this model, only the final neck size of this stage is taken into account. The time it takes for the neck to be formed is ignored. The final neck size of this stage is used as the initial neck size, $x_{0,}$ and is given by the following equation [42]:

$$x_0 = \left(\frac{\gamma_s a^2}{10\mu} \right)^{\frac{1}{3}} \qquad [3.1]$$

3.1.2 Stage 1

The mechanisms that produce stage 1 sintering are as follows: (1) surface diffusion from a surface source; (2) lattice diffusion from a surface source; (3) vapor transport from a surface source; (4) grain boundary transport from a boundary source; (5) lattice diffusion from a boundary source; and (6) lattice diffusion from dislocation sources [42, 43]. All of these mechanisms contribute to neck growth, but only mechanisms 4 to 6 contribute to densification of the compact. This is because densification only occurs when material is transported from the bulk of the material and deposited onto the neck. In this way the particle centers are allowed to move closer together [31]. Those mechanisms that only transport material from the surface of the particle to the neck cannot, therefore, produce densification. These stage 1 mechanisms are outlined in Figure 3.1.

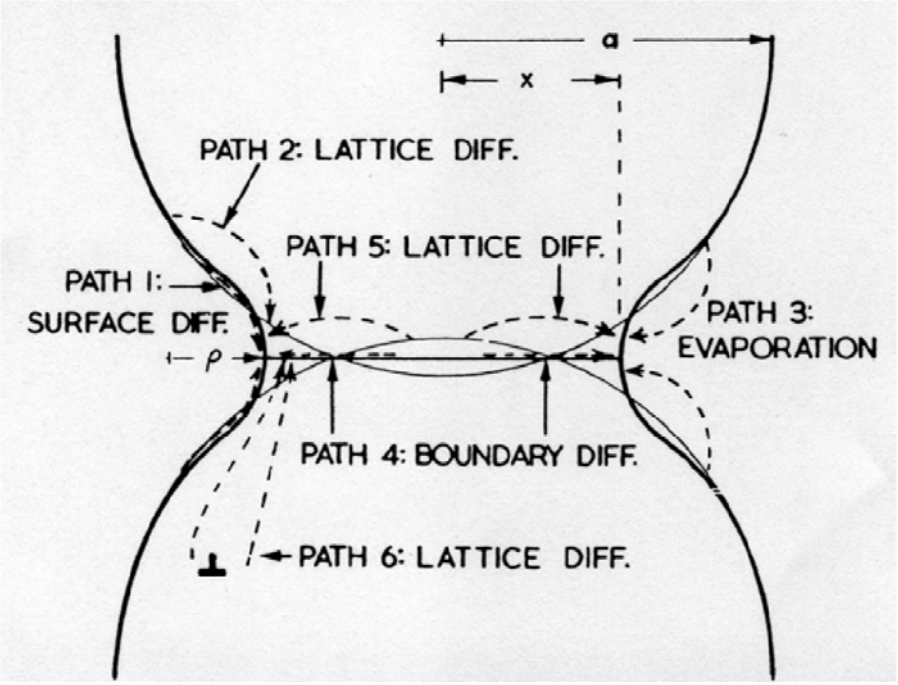

Figure 3.1: The different sintering mechanisms graphically represented and identified by number (defined in text) [43].

The equations for the rate of neck growth for an aggregate of spheres due to each mechanism are given below.

$$x_1^{'} = 2\delta_s D_s F K_1^3 \qquad [3.2]$$

$$x_2^{'} = 2D_V F K_1^2 \qquad [3.3]$$

$$x_3^{'} = 2P_V F K_1 \left(\frac{\Omega}{2\pi\Delta_0 kT} \right) \qquad [3.4]$$

$$x_4^{'} = \frac{4\delta_g D_g F K_2^2}{x} \qquad [3.5]$$

$$x_5^{'} = 4D_V F K_2^2 \qquad [3.6]$$

$$x_6^{'} = \tfrac{4}{9} D_V F K_2 N x^2 \left[K_2 - \frac{\frac{3}{2}\mu x}{\gamma_s a} \right] \qquad [3.7]$$

where F is defined by

$$F = \frac{\gamma_S \Omega}{kT} \qquad [3.8]$$

As sintering progresses the curvature decreases and the neck size increases. As a result, the term in brackets for mechanism 6, lattice diffusion (see equation [3.7]) quickly goes to zero and then becomes negative when using numerical calculations. This would produce a negative neck growth rate, which would mean that the compact would expand with continued sintering. For the purposes of this model, this mechanism is set at zero upon reaching zero.

This model takes into account the redistribution mechanism that is required in order to maintain the sintering driving force. This means that material is deposited from region A to region B, Figure 3.2. This redistribution is governed by the difference in the curvatures K_1 and K_2, so the following equations allow the balance between K_1 and K_2 to be maintained.

$$\frac{\Delta K}{K_1} = \frac{\delta_g D_g}{2\delta_s D_s} \frac{\ln(2)}{\ln\left(\frac{x+\rho}{\rho} - \frac{3}{4}\right)} \qquad [3.9]$$

$$K_m^2 = K_1 K_2 = \left[\frac{1}{x} - \frac{1}{\rho}\right]^2 \qquad [3.10]$$

where

$$\Delta K = K_1 - K_2 \qquad [3.11]$$

The total neck growth rate is the sum of the contribution from each mechanism for neck growth. This is given by

$$x' = \sum_{i=1}^{6} x_i' \qquad [3.12]$$

In the early stage of sintering, there is a good correlation between the neck size and the shrinkage. The shrinkage rate of the compact is therefore given by the following equation derived from [31]:

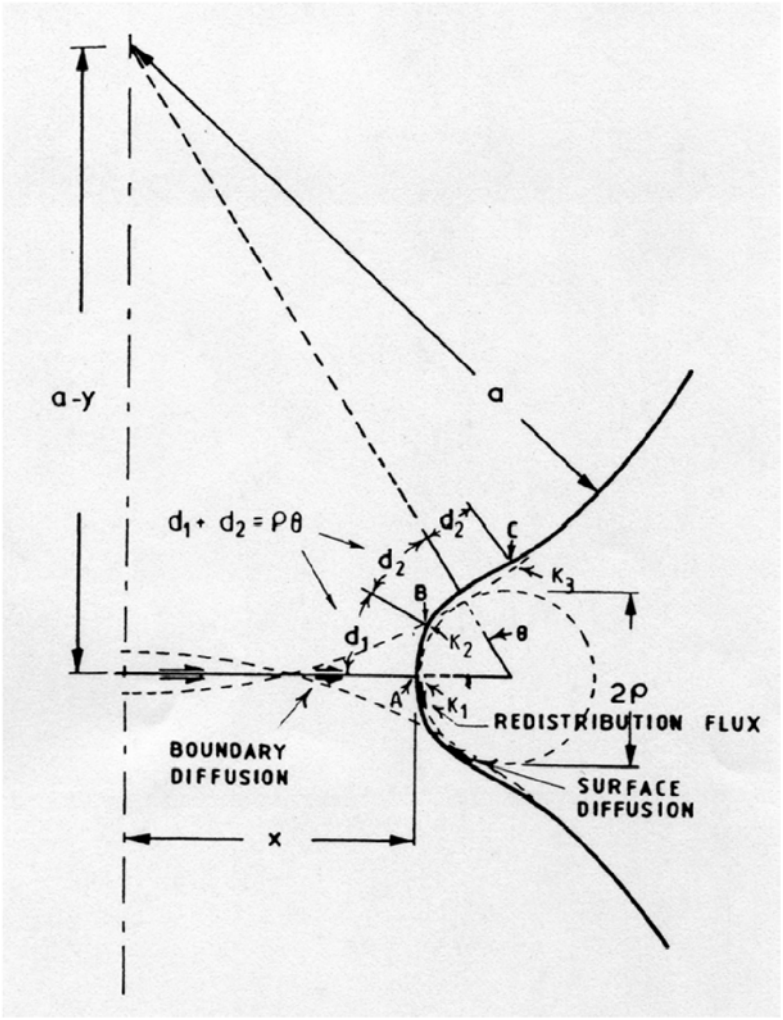

Figure 3.2: Diagram showing the dimensions of two particles in contact and also showing the redistribution flux, which deposits material from region A to region B in order to maintain the sintering driving force [43].

$$y' = \frac{\left(x - x'\right)}{a} \qquad [3.13]$$

For iron, mechanism (4), grain boundary transport, dominates the rate of neck growth during the early portion of stage 1, as shown in Figure 3.3. As the temperature increases past 400°C, mechanism (1), surface diffusion, becomes dominant. Mechanisms (2) and (5), lattice diffusion from a surface source and from a boundary source respectively; play a small but moderate role. The contribution of mechanism (6), lattice diffusion from dislocation sources is quickly eliminated early on. Mechanism (3), vapor transport, only makes a small contribution.

3.1.3 Stages 2 & 3

Stages 2 and 3 are generally considered a single stage for the sintering of spheres. The transition from stage 1 to stage 2 (and stage 3) sintering is denoted by the change in the pores between the particles. The pores become cylindrical channels along grain edges, then spherical pores at grain corners [31]. Figure 3.4 illustrates the difference in pore structure between the stages.

In this model, when the radius of curvature of the neck ρ_1 (calculated for stage 1) coincides with the pore radius ρ_2 (calculated for stages 2 & 3), the sintering equations were modified. Mechanisms (1) to (3) and (6) no longer applied in this stage and mechanisms (4) and (5) are calculated differently. Mechanisms (4) and (5) will now be referred to as mechanisms (7) and (8) to avoid confusion, since they now have the following equations:

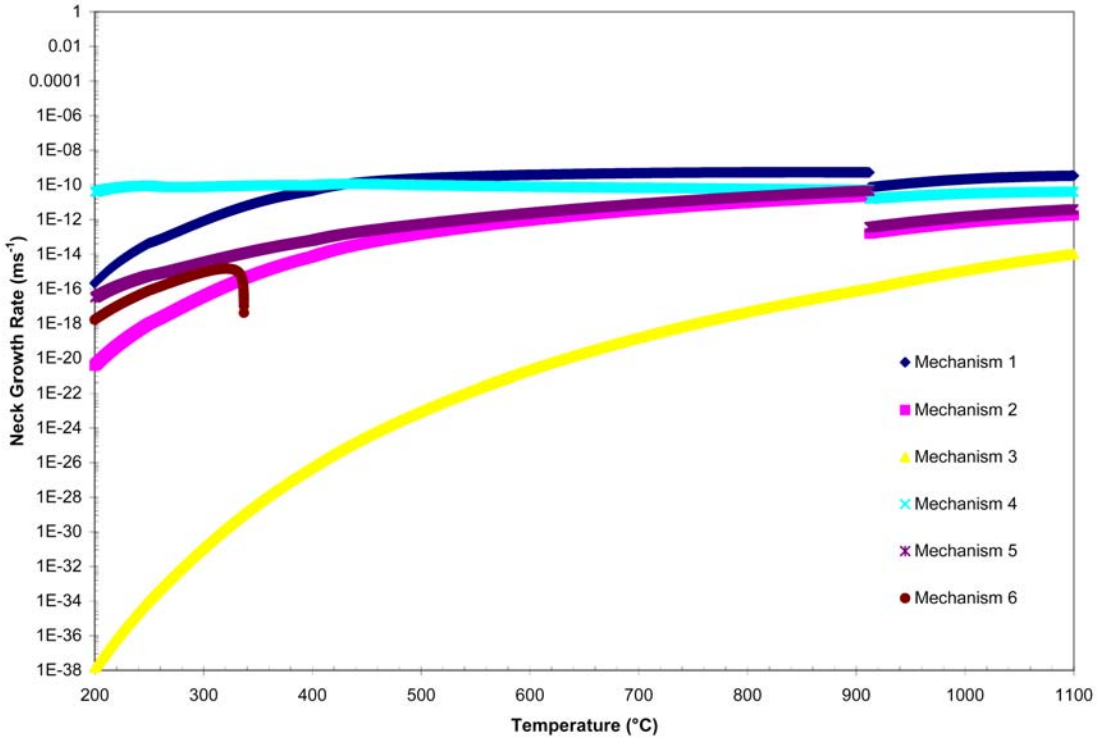

Figure 3.3: The neck growth rate contributions from mechanisms (1) to (6) are plotted against temperature for stage 1. The data were obtained from the sintering model run with the parameters of a compact of iron spheres.

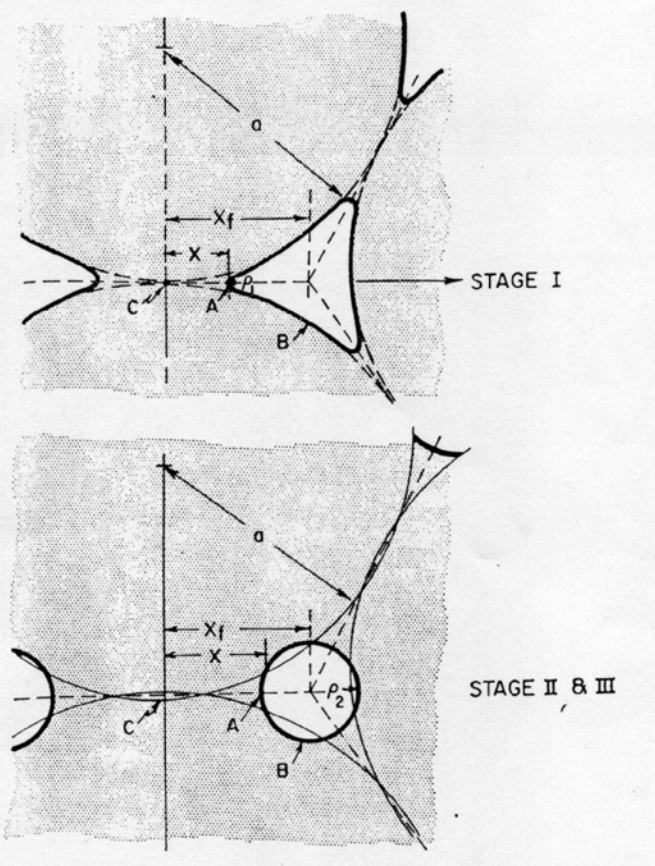

Figure 3.4: The difference in pore structure during sintering for stage 1 and stages 2 and 3 [42].

$$x_7^{'} = \tfrac{1}{16}\delta_g D_g F K_3^3 \left[\ln\left(\frac{x+\rho}{\rho} - \frac{3}{4} \right) \right] \qquad [3.14]$$

$$x_8^{'} = \tfrac{1}{16} x D_V F K_3^3 \left[\ln\left(\frac{x+\rho}{\rho} - \frac{3}{4} \right) \right] \qquad [3.15]$$

The total neck growth rate for this stage is then simply given by the sum of the contributions

$$x^{'} = x_7^{'} + x_8^{'} \qquad [3.16]$$

Although this is a later stage of sintering, the shrinkage rate will be approximated using equation (13), as in stage 1. The curvature K_3, that is included in equations that govern stages 2 & 3, is given by the following equation:

$$K_3 = \frac{2}{x_f - x} \qquad [3.17]$$

At the start of this stage of sintering mechanism (7), grain boundary transport, dominates and continues to do so until the γ to α transformation, which occurs at 1394°C. At this point the neck growth rate rapidly increases due to the increase in diffusivity. Mechanism (8), lattice diffusion, then takes over dominance since the activation energy for volume diffusion increases as a result of the γ to α transformation while the activation energy for grain boundary diffusion decreases. This can be seen in Figure 3.5.

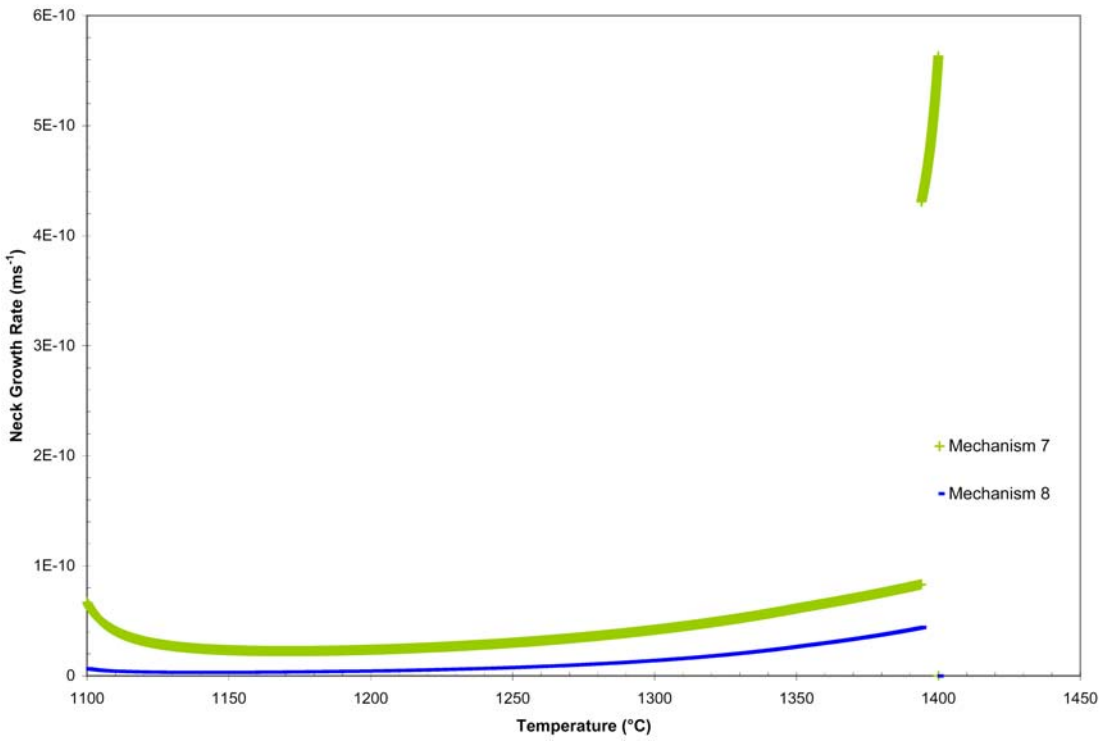

Figure 3.5: The neck growth rate contributions from mechanisms (7) and (8) are plotted against temperature for stages 2 & 3. The data were obtained from the sintering model run with the parameters of a compact of iron spheres. The discontinuity is due to the phase change from γ to α.

Visual Basic was used to write the code for this model. The program is given in Appendix A.

3.2 Particle Dissolution Model

The dissolution of the chromium oxide particles in an iron matrix was modeled using the following mathematical equation that works for the diffusion-limited case:

$$\frac{dR}{dt} = -k\left[\frac{D}{R} + \left(\frac{D}{\pi t}\right)^{\frac{1}{2}}\right] \qquad [3.18]$$

Equation 3.18 is a simple model, which calculates the dissolution rate of the chromium oxide particle with respect to its size R, the diffusivity of chromium in iron D, time t and a parameter k, which is given by [48, 49, 54]:

$$k = \frac{2(C_I - C_M)}{(C_P - C_I)} \qquad [3.19]$$

where C_I is the relative concentration of chromium the iron matrix at that interface, C_M is the relative composition of the matrix far away from the particle and C_P is the relative composition of the particle (see Section 2.6). The equation used in this model does not take into account the fact that there are particles of several sizes in any given system. Therefore, only the largest particle measured is input into the model. Since the largest particle would be the last to dissolve, the time to complete dissolution of that particle is the time to dissolution of all the particles in the sample. The composition values in

weight fraction used in this model for C_I, C_M and C_P are 0.1, 0 and 1, respectively. The largest particle is estimated to have a radius of 15μm.

Two heat-treatment regimes were modeled. Those performed at a 1000°C isothermal hold and those performed with a constant heating rate of 5°C/min. The effect of the different heat-treatments was represented by the diffusivity of chromium in iron. The diffusivity for the case of the isothermal heat-treatment was taken to be 0.05 $\mu m^2/s$ rather than 0.035 $\mu m^2/s$, as would have been calculated by data in the literature [34] (see Table 2.1). This value is a mid-range average taken from Boltzman-Matano [52, 53] calculations performed on concentration gradients that were measured on some of the samples heat-treated with a 1000°C hold (see Equation 2.23 in Section 2.6). The diffusivities for the case of a heat-treatment with a constant heating rate were calculated using literature values [34] for the diffusion coefficient and the activation energy for convenience.

Mathlab was used to write the code for this model. The program code is given in Appendix B.

CHAPTER 4

EXPERIMENTAL PROCEDURE

The subsequent reduction of Cr_2O_3 particles after complete iron oxide reduction is a result of the environment that the oxide particles inhabit. The factors that affect Cr_2O_3 reduction in partially reduced Fe-Cr honeycombs are the following: 1) the iron matrix porosity which is dynamic; 2) gaseous transport of H_2 through the iron matrix to, and gaseous transport of H_2O from, the Cr_2O_3 particles; and 3) diffusion of Cr through iron matrix away from the reducing Cr_2O_3 particles.

4.1 Extrusion

Pastes of iron and chromium oxide were prepared in the method described by Hurysz [3]. The desired end compositions were input into a program [3] that calculates the oxide, binder, lubricant and water compositions in order to produce the desired solids loading of 48% by volume. Compositions of the oxide pastes were made to produce 5, 15 and 25wt% chromium in iron upon reduction. These pastes consist of Fe_2O_3 and Cr_2O_3 powders mixed with water; Methocel A4M as a binder, with a 3:1 water to binder ratio; and 100S Pegosperse as a lubricant, with a 15:1 binder to lubricant ratio. The dry Methocel binder was first blended with the oxides before water was added to allow even mixing without clumping. The lubricant was added to the

water, and that mixture was then added to the dry oxide–binder mixture and blended further. The powder granules formed were made into a paste using a Buss kneader. These pastes were extruded into honeycombs of 0.3mm wall thickness (see Figure 4.1). The extruded pieces were cut into the desired lengths and dried at room temperature for at least 48hrs. The resulting samples were labeled for the alloy composition they would produce. For example, an iron oxide chromium oxide honeycomb that would produce an alloy containing 5wt% chromium when reduced was simply labeled a 5wt% sample.

4.2 Heat-Treatments

4.2.1 Sample Preparation

The dried iron oxide chromium oxide honeycombs of compositions 5, 15 and 25wt% were prepared for heat-treatment by cutting them into lengths of 1cm. The cut edges were sanded using 800-grit SiC paper then air dusted to remove the oxide and SiC powder debris from within the honeycomb cells.

4.2.2 Calcination

The samples were calcined in air before being heat-treated in order to burn out the carbonaceous compounds from the binder and lubricant additions that would aid in the reduction process. It was desired that reduction would take place only as a result of reaction with hydrogen. The cut honeycombs were placed in a Keith bottom-loading furnace and were calcined to 500°C at a heating rate of 0.4°C per min. After reaching

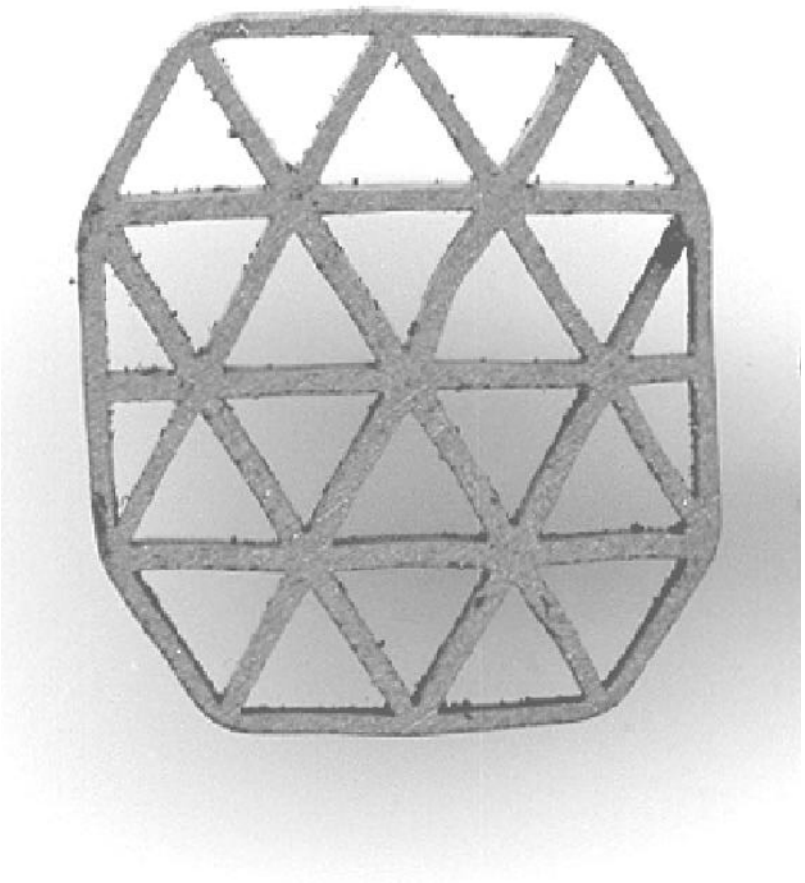

Figure 4.1: Typical section of an extruded honeycomb. Section is perpendicular to extrusion axis.

500°C, the samples were allowed to furnace cool. Special care was taken when handling the samples after this step because they became fragile as a result of binder being removed.

4.2.3 Reduction Experiments

The calcined samples were heat-treated in a gold infrared image furnace to various temperatures, under flowing He and H_2. The samples were placed lengthways on alumina sample trays with the axis of the honeycomb parallel to the gaseous flow, as shown in Figure 4.2. The sample was placed in contact with the sheath of the thermocouple, which was coated with powder of the same composition as the sample. Heat treatment schedules consisting of heating ramps of 5°C min^{-1} to 250°C and 2°C min^{-1} to 400°C, both under pure He, then 5°C min^{-1} to the desired heat-treatment temperature under pure H_2, followed by a quench to 20°C at a rate of 100°C under pure He were performed. There were no hold times after any of the heating ramps. The gaseous flow-rate for both the He and the H_2 was 1 liter min^{-1}.

4.2.4 Diffusion Experiments

Calcined samples of each of the three compositions were heat-treated to 800°C and 1000°C, using the same heating schedules and gaseous flow parameters that were used for the reduction experiments except, hold times of 10 and 100 mins were performed upon reaching the target temperature. The isothermal holds were performed under pure H_2 with a flow rate of 1 liter min^{-1}. Concentration distribution data was obtained from these samples via EDS line scans, which were taken of the matrix,

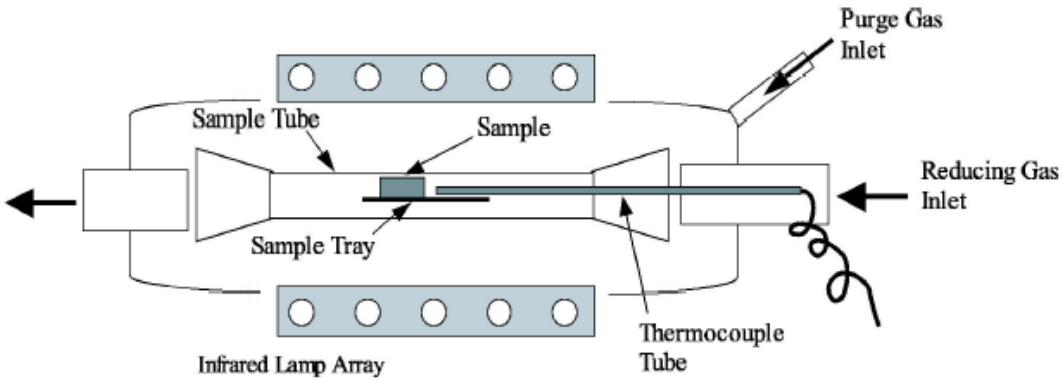

Figure 4.2: Schematic of the gold infrared furnace set up showing sample positioning [6].

radiating outward from the chromium oxide particles. The Boltzmann-Matano analysis was used to calculate diffusivities from the concentration profiles and to help ascertain what mode of dissolution was taking place. (See Section 2.6).

4.3 Sample Characterization

4.3.1 Vacuum Impregnation

Portions of the heat-treated samples were vacuum impregnated in Epo-Heat epoxy and hardener. The epoxy and hardener were mixed to manufacturer's specifications and poured over the samples, which were placed in molds. The samples were placed standing with the axis of extrusion being vertical. They were then placed under vacuum until the majority of the air was expelled from the sample. This occurred when the surface of the epoxy became transparent again. Air was slowly introduced into the chamber at this point until atmospheric pressure was reached. It is the atmospheric pressure that forces the epoxy to impregnate the sample. The impregnated sample was then cured for the time and temperature specified by the manufacturer. Vacuum impregnation was necessary for these samples because the samples heat-treated to lower temperatures were weaker as they had less opportunity to sinter. Vacuum impregnation allowed the microstructural integrity of the sample to be retained for analysis after polishing

4.3.2 Polishing

The vacuum impregnated samples were polished on a polishing wheel using SiC paper decreasing in coarseness from 800-grit to 4000-grit. To avoid excavation of the

softer, more porous areas between the harder features of the weaker samples, the final fine polish was performed using nylon napless polishing cloths. Alumina slurries were used on the polishing cloths with particles decreasing in size from 1μm to 0.5μm.

4.3.3 SEM Analysis

A LEO 1530 scanning electron microscope was primarily used to obtain images of the polished samples. The electron-backscatter detector was used to obtain the best contrast between the chromium oxide particles and the surrounding matrix. The backscattered images obtained were analyzed with image analysis software to quantify pore and particle distribution characteristics. The EDS capabilities of both the LEO 1530 and the Hitatchi S-800 microscopes were used to obtain concentration distribution information for dissolution studies and compositional maps of notable regions in the samples. Both microscopes were operated at 15keV.

4.3.4 Image Analysis

The backscattered images were analyzed to obtain the pore and chromium oxide particle characteristics of the heat-treated samples. Area fractions of the pores and of the particles, as well as the areas of sectioned the particles, were measured using Zeiss KS400 image analysis software, Version 3.0.

For particle size analysis, Saltykov's method [55] was used to obtain particle size distributions from the measured areas of the particle sections. The diameters of the particle sections were calculated and separated into size classes. A minimum of seven to a maximum of fifteen size classes was used. The interval of each size class was a

function the number of size classes used and the size of the largest particle measured. Saltykov's method was applied using the coefficients to calculate the number of particles per unit volume for each size class. (See Appendix C for more details on using Saltykov's method). In the situations where the calculated number density of particles for any size class turned out to be a negative number, the number of particles in each size class for that particle size distribution was adjusted, first by multiplying by the sum of positive numbers and then by dividing by the total sum. The size classes, which contained negative numbers, were set to zero [56] and this became the new particle size distribution.

4.3.5 X-Ray Diffraction Analysis

Phase analysis was performed on the 15wt% samples heat-treated to each temperature and on the 5wt% and 25wt% samples heat-treated to 800°C and 1000°C. Nelson- Riley plots [57, 58] were used to calculate the precise lattice parameter of each sample. The lattice parameter values were used to determine the increasing chromium content in the iron matrix as reduction of the chromium oxide particles takes place. The lattice parameter values were determined using the measurements of Pearson *et al.* [59]. They measured the lattice parameters for a series of iron-chromium compositions and determined that the relationship between lattice parameter and composition deviated from Vegrard's law. Figure 4.3 shows this measured relationship. The lower composition portion of data was fit to a 5^{th} degree polynomial, as seen in Figure 4.4, in order to obtain the chromium composition in iron from the lattice parameters measured

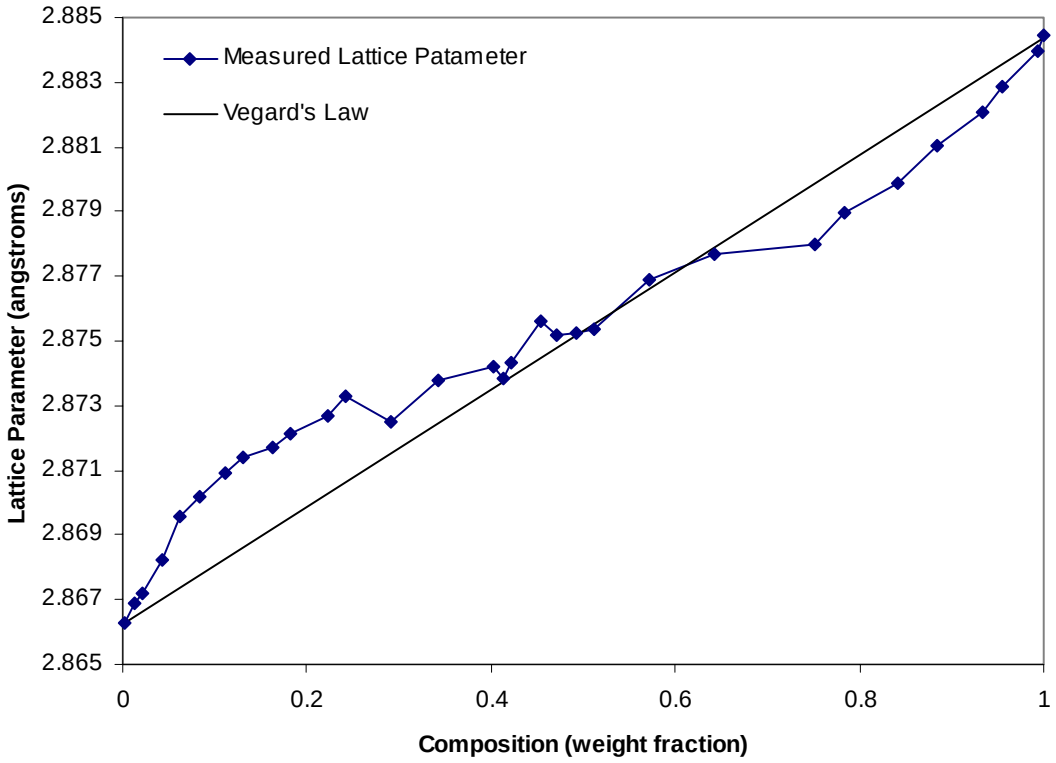

Figure 4.3: Lattice parameter data as measured by Pearson is plotted with respect to iron-chromium composition [59]. These data are compared to those predicted by Vegard's law.

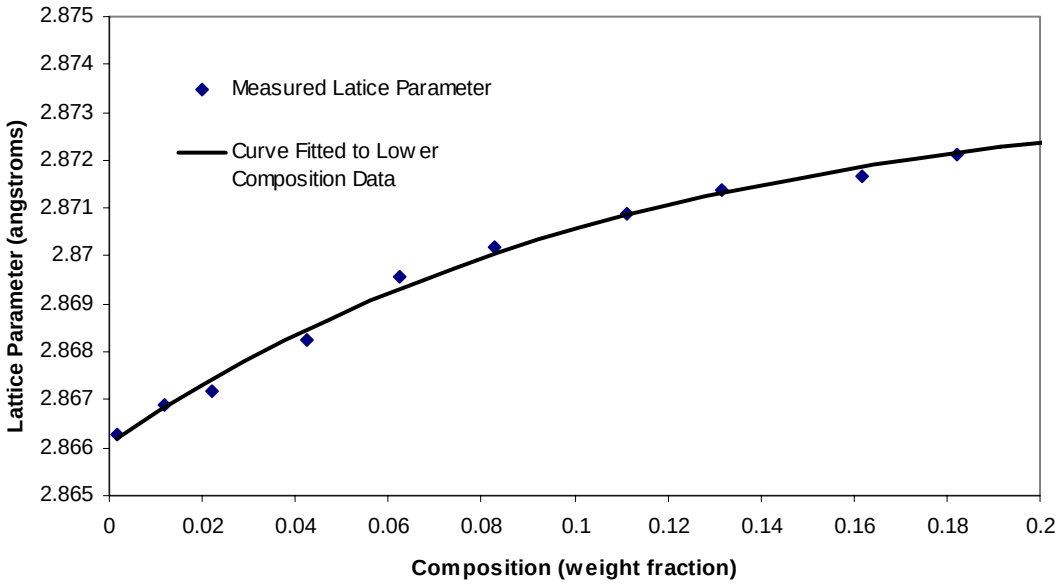

Figure 4.4: Lattice parameter data presented in Figure 4.3 over the range 0 - 0.2wt fraction chromium were fitted to a 5th degree polynomial. The results were used to determine the composition of chromium in the iron matrix from measured lattice parameters in this work.

for these samples. Weaker samples were ground into powder for this analysis. In the cases where the samples could not be ground, their outer walls were X-rayed.

4.4 Sintering Model

When reducing oxide honeycomb structures to produce iron-chromium alloys, the iron oxide is first reduced to the metal as mentioned earlier, forming an iron matrix around the unreduced chromium oxide particles. The iron matrix starts to sinter as the chromium oxide particles proceed to reduce. The densification of the matrix around the particles becomes a barrier to further reduction because the iron slows diffusion of H_2 to the chromium oxide particles as well as H_2O away from the reducing particles. The sintering of the matrix will be modeled by applying sintering equations that model the sintering of an aggregate of spheres while taking into account the state of the iron matrix being sintered.

The unique characteristics of this system that would make the sintering process differ from that of a regular compact of metal powder are (1) that the iron in this system has been reduced from the oxide; and (2) that there are also chromium oxide particles still present and being reduced as sintering takes place. The reduction of iron oxide to iron metal results in a compact of agglomerates composed of smaller iron powder particles. As mentioned previously, the rate of sintering of any powder compact is highly dependent on the particle size. As a result, the smaller particles within the agglomerates sinter at a faster rate while the larger agglomerated particles sinter more slowly. This produces bimodal sintering, since two sintering regimes are taking place.

The combined effect of intra- and inter-agglomerate sintering, contributes to the overall shrinkage of the compact.

For the model that will be presented, the bimodal sintering behavior is taken into account as well as the changes in sintering kinetics that occur when iron undergoes phase changes from α to γ then back to α. The model will be compared to experimental results for iron that has been reduced from its oxide without the presence of chromium oxide.

For the model to account for the presence of chromium oxide, one would have to consider that reduction of chromium oxide to the metal would naturally contribute to the shrinkage of the compact. In addition, sintering in the matrix is delayed with increased chromium oxide composition in the sample. This is because increasing the amount of chromium oxide present produces increased interconnectivity of the chromium oxide particles in the matrix so that the reduced iron is more separated and has less opportunity to come into contact with each other. This delay persists until enough chromium oxide has reduced to the metal in order to allow the iron particles to come into contact. All these factors would then have to be described in the model.

The model was also run for a compact of nickel oxide in order to ascertain its validity. The results of the model were compared to data obtained from a pellet of nickel oxide that was heat-treated under hydrogen in a dilatometer. The pellet was heat treated to 200°C at 5°C/minute then to 1200°C at 3°C/minute. The pellet was held isothermally at that temperature for 100 minutes then cooled. No phase changes occur in nickel as it is heated so a simplified version of the model was used.

The model will consider the following stages of sintering: Stage 0 = adhesion, the rearrangement and initial contact of particles; Stage 1 = initial stage neck growth, where the contact area and the bonds between particles become larger and stronger; and Stages 2 & 3 = intermediate and final stages, where pore reduction and elimination produces a densified structure. The equations and parameters used to create the model are explained in Chapter 3.

The computer program is written in Visual Basic and uses the input of an initial start temperature, heating schedule and various material constants to calculate for each time step using the parameters given by the equations above. Initially a heating rate must be used since the start temperature must be lower than the standard sintering temperatures. The model has the capability to accommodate an isothermal hold once the desired temperature is reached.

Sintering is considered to be complete for an aggregate of spheres when the neck size x, is 74% of the initial particle size a, i.e., when $x = 0.74a$. At this point the compact has reached full density. The program terminates when the neck size has reached this value or when the specified heating schedule has ended. The outputs are sintering parameters such as neck size and shrinkage rate, which can be plotted versus temperature or time.

CHAPTER 5

RESULTS AND DISCUSSION

In this study, iron oxide and chromium oxide paste mixtures were formed into honeycomb structures and subsequently reduced. It is well understood that when coupled in a hydrogen atmosphere, iron oxide will completely reduce before chromium oxide does [6, 14]. This results in chromium oxide being distributed in an iron metal matrix. The reduction of the chromium oxide particles and the dissolution of the resulting chromium metal into the iron matrix were studied in this work. The densification of the iron matrix, the contact between the chromium oxide particles, the reduction of chromium oxide to chromium and the subsequent diffusion of chromium were all examined. Thus the role that the iron matrix plays in the elimination of the chromium oxide particles was investigated. A sintering model was used to follow the changes occurring in pure metal powders, as affected by heat-treatment.

5.1 Sintering Model for Single Metallic Powder

The sintering equations developed by Ashby *et al*. [42, 43] were adapted and used to describe the shrinkage that occurs in a iron powder compact, similar to the matrix in these experiments. The rate of sintering, as predicted by the model, shows that the time it takes to densify is very sensitive to the initial particle size. For small particle

sizes, on the order of 1 μm, the sintering rates are magnitudes faster than for larger particles and agglomerates. This is illustrated in Figure 5.1, where results of the model for various particle sizes are shown. One can see that there is a large difference in the absolute shrinkage the model calculates for compacts of different initial particle size. The shrinkage calculated for a compact of 1 μm particles has reached its maximum at about 700°C, with the transition between Stage 1 and Stages 2 & 3 occurring at about 650°C. No further sintering takes place. For a compact of 10 μm particles, the end of the heating schedule is reached before sintering is complete. The transition between Stage 1 and Stages 2 & 3 occurs at about 1350°C. For a compact of 100 μm particles, minimal shrinkage is achieved and the transition from Stage 1 to Stages 2 & 3 has not occurred before the end of the heating schedule.

To describe the sintering of the iron matrix, which has been reduced from the oxide, the results from two particle size regimes, 5 and 9 μm, were used. As mentioned earlier, the reduced iron in the honeycomb is distributed, as agglomerates composed of smaller particles. Because of the dependence of sintering rate on the size of the particles, sintering of the smaller particles within the agglomerates reaches completion before the sintering of the agglomerates themselves. The shrinkage due to each of the two particle size regimes contributes to the overall shrinkage of the compact.

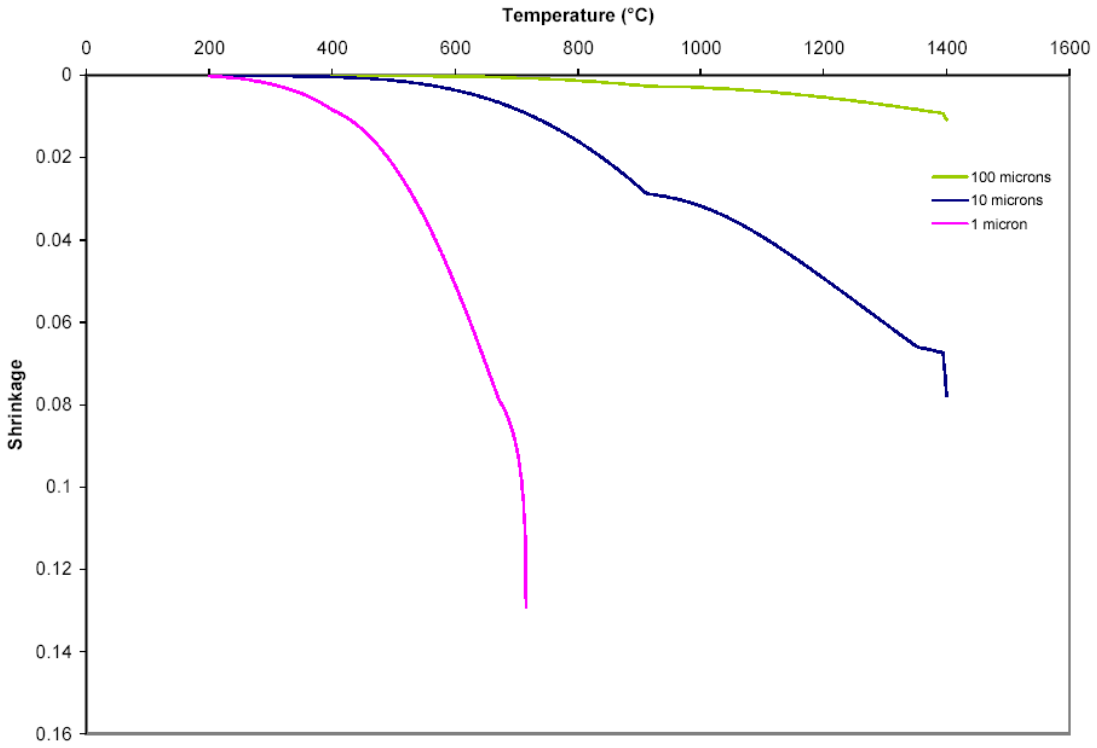

Figure 5.1: Results of the sintering model for pure iron with different initial particle sizes. The heating schedules used in the experimental data were applied here.

5.1.1 Sintering Model Results for a Controlled Heating Rate

The program was run with values for the state of a compact of iron powder of particle radius 5 μm and for a compact with agglomerate radius 9 μm to account for the two size classes present. An initial temperature of 200°C was used with a heating schedule of 5°C/minute to 250°C, 3°C/minute to 400 and 5°C/minute to 1400°C, in keeping with the work done by Nadler [6]. The changes in the properties of iron for the α to γ and γ to α transformations were accounted for in the rate equations. Shrinkage results from this model (Figure 5.2) were compared to experimental shrinkage data for an iron honeycomb run in a dilatometer. The complete experimental data are shown in Figure 5.3 [6].

The shrinkage and the rates of shrinkage due to sintering are depicted in the model results. At 912°C and 1394°C, the iron changes from the α phase to the γ phase then back to the α phase, respectively. The model does not account for the large volume change due to the α to γ and γ to α transformation. As a result, there are noticeable shrinkage changes that appear in the experimental data at these temperatures that do not appear in the model results. At 912°C there is a volume decrease as the iron transforms from α to γ, which causes a surge in shrinkage in the experimental data that is not observed in the model results, (see (A) in Figure 5.2). Likewise, at 1394°C there is a volume increase as iron changes from γ to α that produces an apparent slow down in the shrinkage rate of the experimental data that is not shown in the model results (see (B) in Figure 5.2).

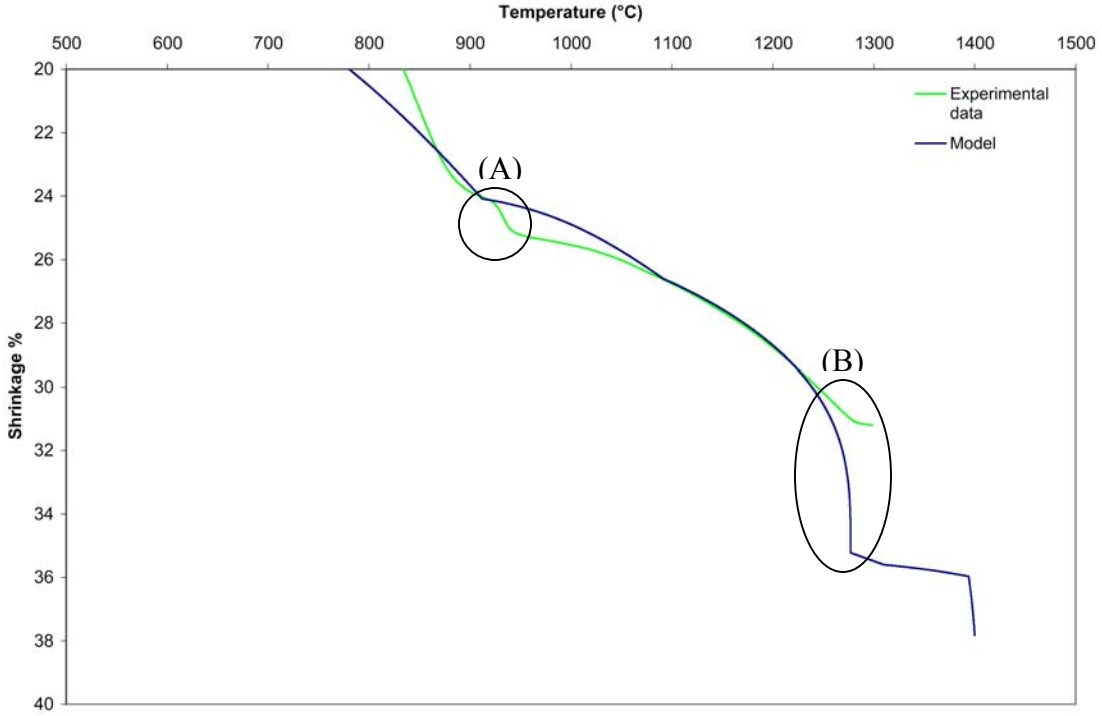

Figure 5.2: Results of the sintering model for pure iron with the combined sintering regimes compared to experimental shrinkage data for the same system. The shrinkage of the model is adjusted to the sintering portion of the experimental data, as shrinkage due to reduction is not included in the model. The portion labeled (A) shows the shrinkage increase due to the α to γ transformation in the experimental results that is not shown in the model results. The portion labeled (B) shows the decrease in shrinkage due to the γ to α transformation in the experimental results that is not shown in the model results. The heating schedules used in the experimental data were applied here. Experimental data are taken from [6].

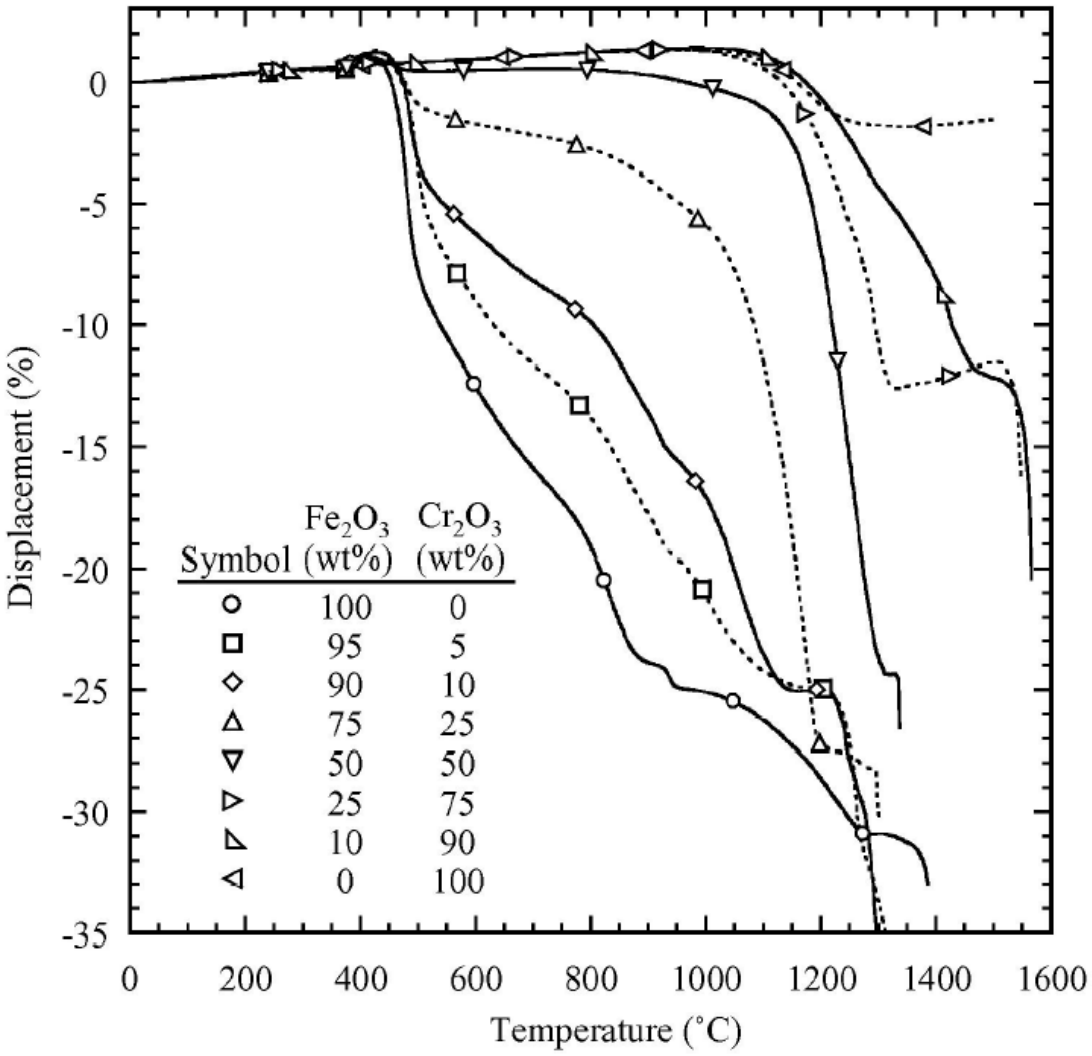

Figure 5.3: Dilatometer shrinkage data for various compositions of iron-chromium honeycomb [6, 17].

The results in Figure 5.4 show the comparison between the shrinkage rates for the model and the experimental data. The complete experimental data are shown in Figure 5.5 [6]. The discontinuities shown are due to the fact that the model treats the transitions between α to γ and γ to α and the changes from Stage 1 to Stages 2 & 3 as discontinuous. As a result the shrinkage rates appear to jump from one transition to the other unlike the experimental data. The values for the rates of shrinkage from the model do not consistently align with those calculated from experimental data, but they follow the same trends and often intersect. It is interesting to note the discontinuity in the model due to the change from Stage 1 to Stages 2 & 3 for the smaller particles. At the same time, there is a corresponding change in the sintering rate of the experimental data. At this time the larger particles are still experiencing Stage 1 sintering.

Despite the discontinuities in the rates of shrinkage shown in the model due to the different conditions experienced, the predicted shrinkage due to sintering does compare well with experimental data. The model accounts for the changes in sintering rate due to the phase changes that iron undergoes, though it does not account for the change in volume as a result of this change. The model also accounts for the differential shrinkage rates experienced due to the different size classes present. The faster shrinkage rates of the smaller iron particle as well as the slower shrinkage rates of the agglomerates both contribute to the overall shrinkage of the compact.

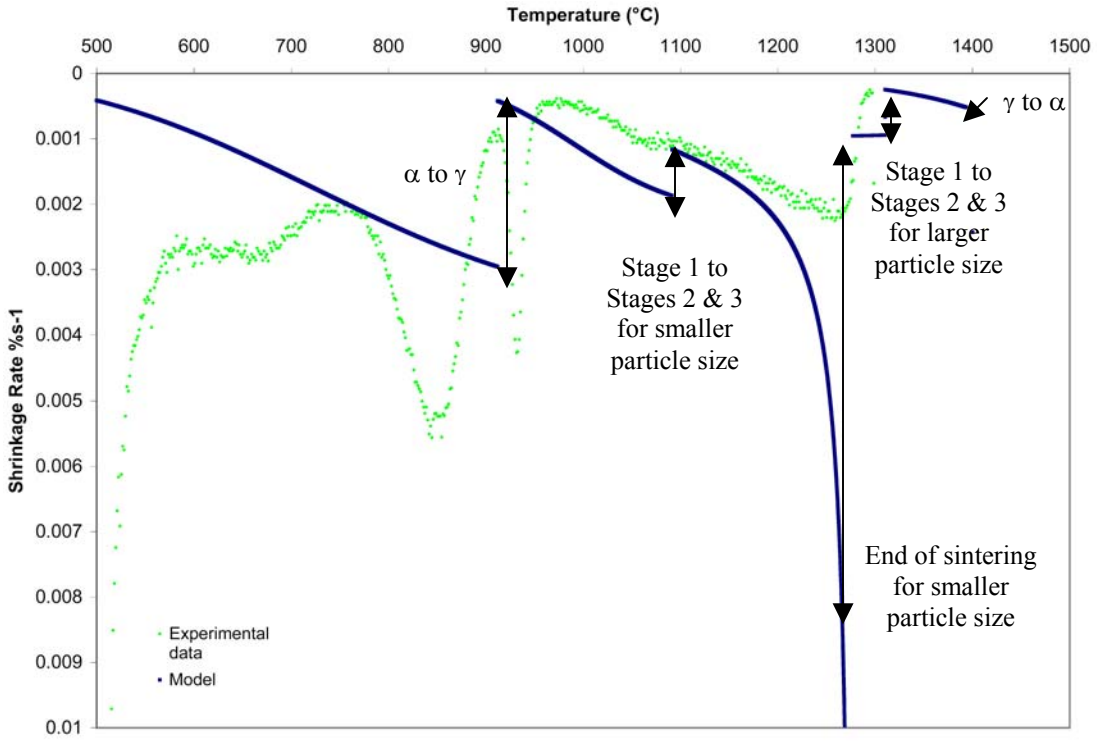

Figure 5.4: Shrinkage rates obtained from the sintering model shown with experimental shrinkage rates for an iron oxide honeycomb that was reduced to iron and is experiencing sintering of iron after the temperature of 600°C. Experimental data taken from [6].

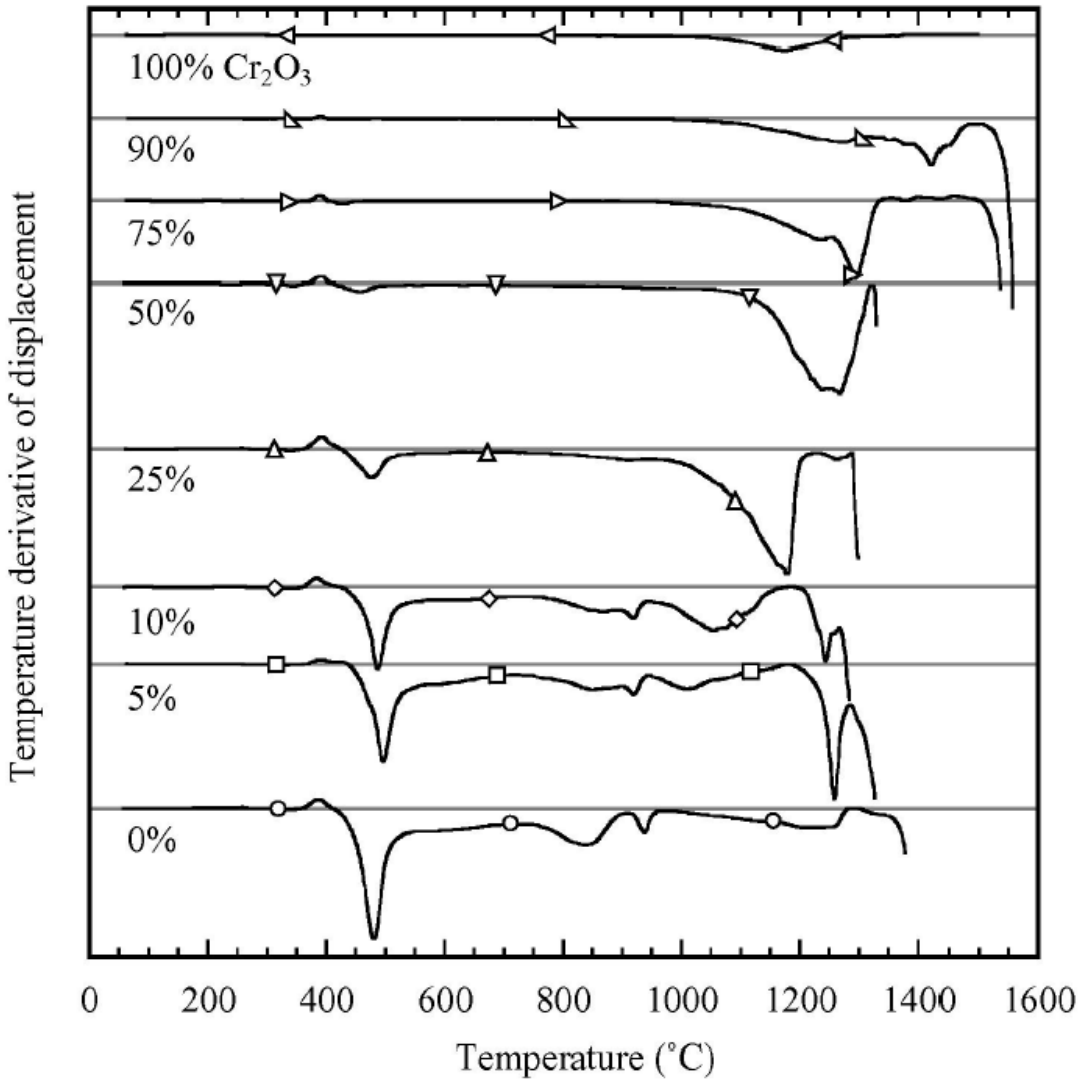

Figure 5.5: Temperature derivatives of dilatometer traces from Figure 5.3 [6, 17].

5.1.1.1 Sintering Model Results for Nickel Oxide Compact

The program was run with values for the state of a nickel compact with a small particle size of 3 μm and agglomerate size of 8μm. An initial temperature of -50°C was used. This was in order to suppress a large jump in the contribution of mechanism (4) (grain boundary diffusion) that occurs as soon as the program starts (see Figure 5.6). The values of the parameters given for nickel caused an immediate jump in the neck size that terminated the program before data could be calculated. The model used a heating rate of 5°C/minute to a temperature of 250°C and then a heating rate of 3°C/minute to 1200°C. The sample was held at that temperature for 100 minutes. Shrinkage results of the model are given in Figure 5.7 along with experimental data that was obtained from a nickel oxide pellet that underwent the same heat-treatment as above. The shrinkage data obtained from the model was adjusted to account for the shrinkage due to reduction that is experienced by the compact in the experiment. The portion of the Figure 5.7 labeled (A) denotes the end of fine particle sintering while the portion labeled (B) indicates both the point at which sintering transitions from stage 1 to stages 2 and 3 and at which shrinkage is still occurring while the temperature is being held constant.

The results of the sintering model for a compact of reduced nickel oxide does show a reasonably good correlation with experimental data, though not as well as it did for the case of iron oxide. This is most likely due to the fact that the model does not accommodate small initial particle sizes without using a very cold initial temperature. This model can still be very useful for predicting the sintering behavior of various metallic powders given the appropriate materials parameters.

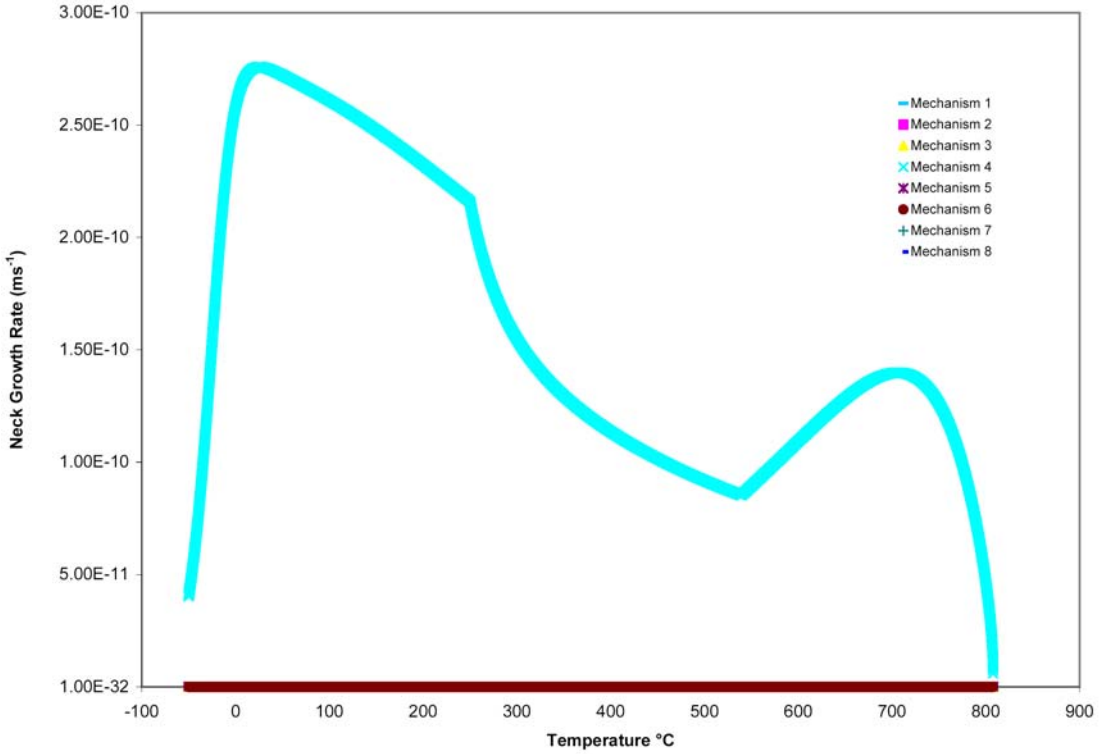

Figure 5.6: The neck growth rate contributions from mechanisms are plotted against temperature. Mechanism (4), grain boundary diffusion from a boundary source, dominates. The data were obtained from the sintering model run with the parameters of a compact of nickel spheres.

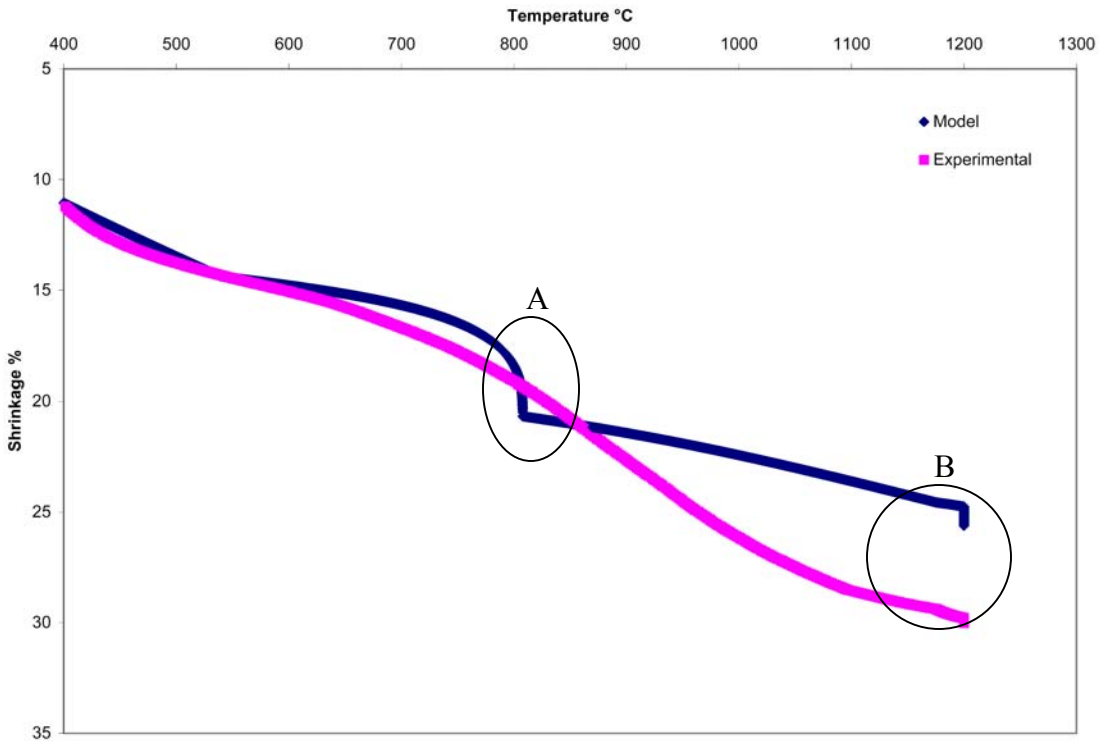

Figure 5.7: Results of the sintering model for pure nickel with the combined sintering regimes, as compared to experimental shrinkage data for the same system. The shrinkage of the model is adjusted to the sintering portion of the experimental data, as shrinkage due to reduction is not included in the model.

5.1.2 Sintering Model Results for a Controlled Heating Rate with an Isothermal Hold

As discussed in Section 2.5, sintering is enhanced when a heating rate is used. The steady increase in the shrinkage rates achieved under these conditions is quickly lost when an isothermal hold is applied. The program was run with the same initial values and heating rates for iron as before but an isothermal hold at 1000°C was incorporated into the parameters. Figure 5.8 shows the shrinkage results of the model when an isothermal hold is applied compared to results from just using a steady heating rate. At 1000°C, which for simplicity occurs at time equals zero, the shrinkage predicted for each heat-treatment regime deviates from each other. The results of the model for non-isothermal parameters show an increasing rate of shrinkage as the experiment progresses. The model results for the isothermal parameters show shrinkage that is still increasing, but at a decreasing rate. The relaxation in the shrinkage due to holding at a specific temperature is very apparent using this model.

The model was representative of the sintering experienced by an iron powder compact that is in a state similar to iron that has been reduce from the oxide by hydrogen. The incorporation of chromium oxide into the compact has the overall effect of decreasing the sintering that occurs in the iron matrix. This effect increases as the amount of chromium oxide increases and the interconnectivity of the iron matrix is reduced. However, the effect that the heat-treatment regime has on the sintering of the iron matrix remains. Therefore the heat-treatment regime used when reducing iron oxide/chromium oxide honeycombs affect the environment in which the chromium oxide particles reduce.

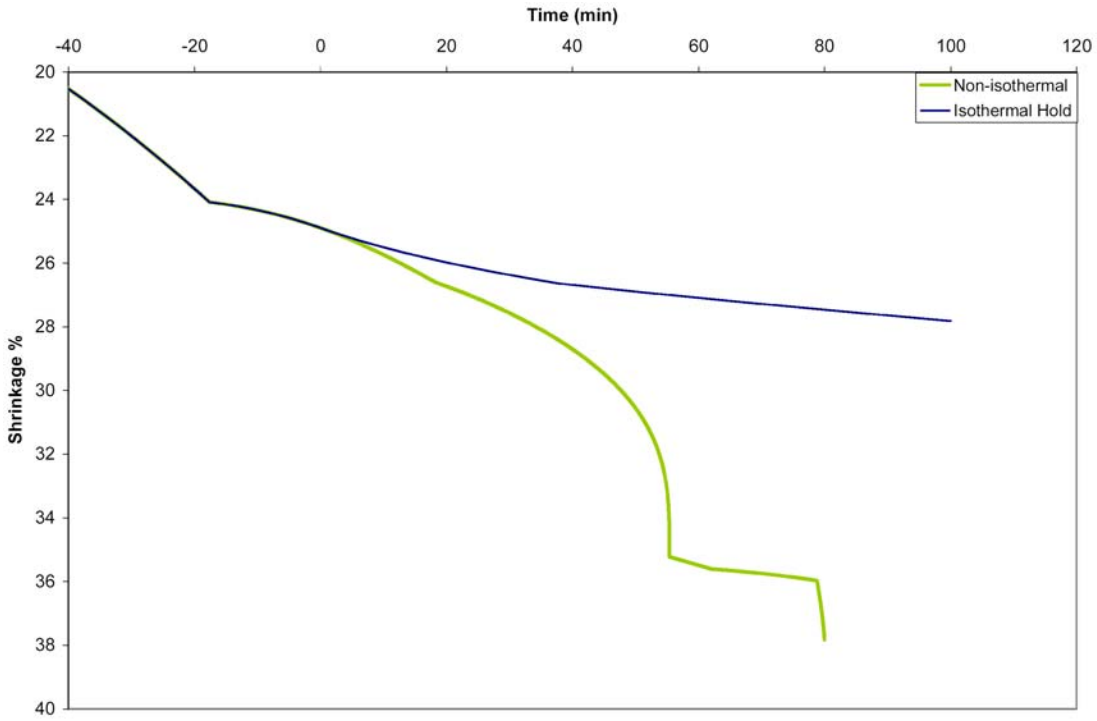

Figure 5.8: Results of the sintering model that shows the shrinkage rate with time for iron sintered under a heating rate of 5°C per minute to 1400°C (non-isothermal) and iron sintered at 5°C per minute to 1000°C and then held for 100 minutes (Isothermal Hold). The time measured starts when the sample reaches 1000°C. Negative time is related to the shrinkage that has occurred before the temperature of 1000°C is reached.

5.2 Heat-Treatments Using a Heating Rate

5.2.1 Microstructural Development

The cross-section microstructures of 5wt% samples that were heat-treated to various temperatures then quenched were studied. A series of these microstructures are shown in Figure 5.9. The most striking change in the microstructure occurs between heat-treatment temperatures of 700°C and 800°C. The chromium oxide particles become easier to identify at 800°C and above. The samples at 600°C and 700°C show particles that are not easily distinguishable from the rest of the sample without EDS mapping, as shown in Figure 5.10. Only subtle grey scale gradients differentiate the chromium oxide from the iron. The large amount of porosity that remains in the matrix prevents the different phases from being adequately resolved. This is shown in Figure 5.11. At 800°C the sample is sufficiently sintered so that the particles can be visually distinguished using a backscatter detector, Figure 5.12. It is also observed that the chromium oxide particles in the samples heat-treated to 800°C and above are not as porous as they are at lower heat-treatment temperatures. They become intimately imbedded into the matrix. In fact, the pores within the chromium oxide particles appear to be filled with the iron matrix, which is a result of the enhanced sintering that takes place in these heat-treatments. This will be discussed further in Section 5.4.

Samples of compositions 15wt% and 25wt% were heat-treated in the same manner. These samples differed from the 5wt% samples in that the reduction and sintering processes are delayed by the increase in chromium oxide content. This is a result of the increased interconnectivity of the chromium oxide phase. As the amount of chromium oxide in the sample is increased, the interconnectivity of the oxide phase is

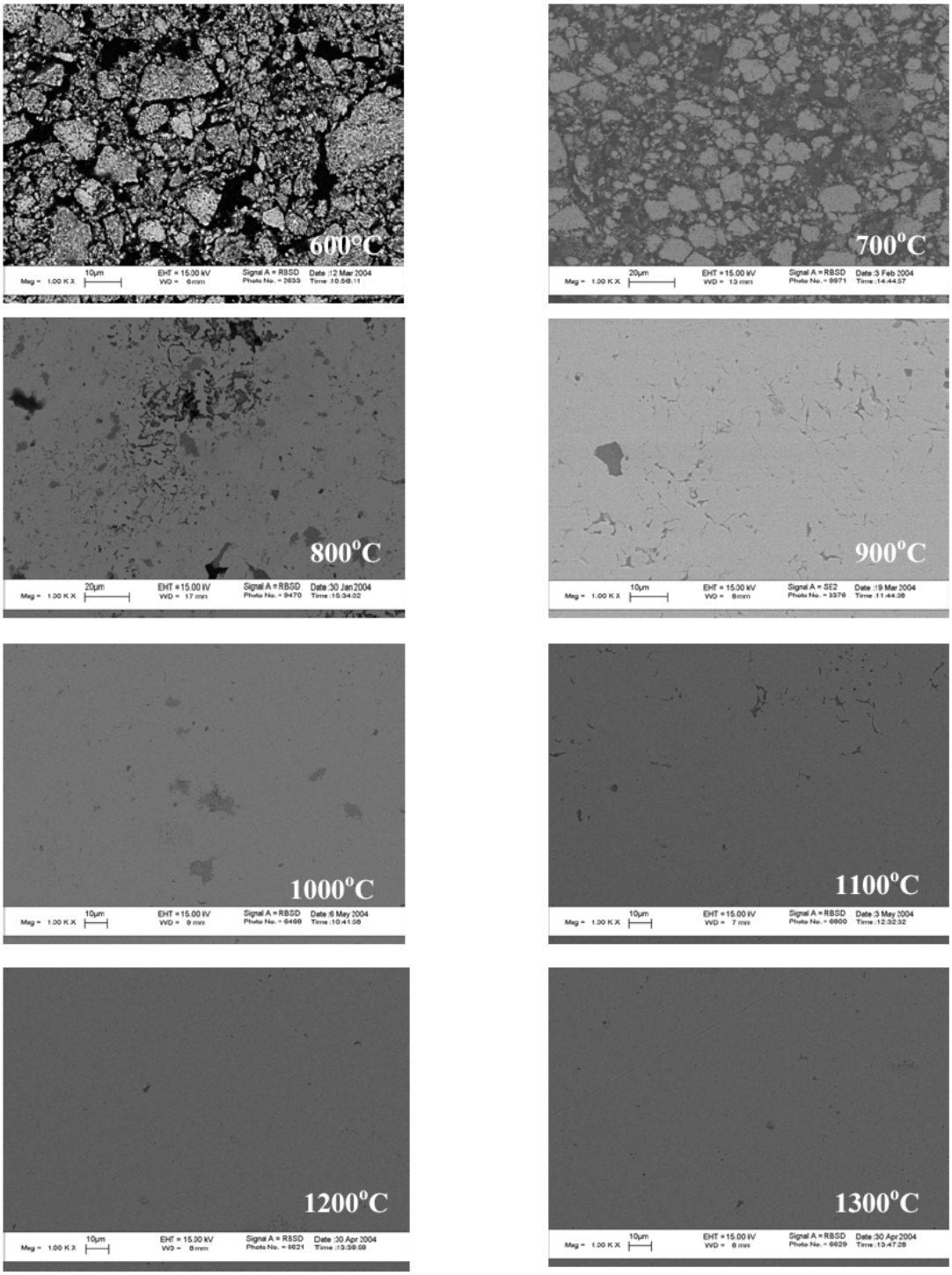

Figure 5.9: SEM polished cross-section images of iron-chromium samples (5wt% chromium). Each sample was heat-treated to the temperature indicated.

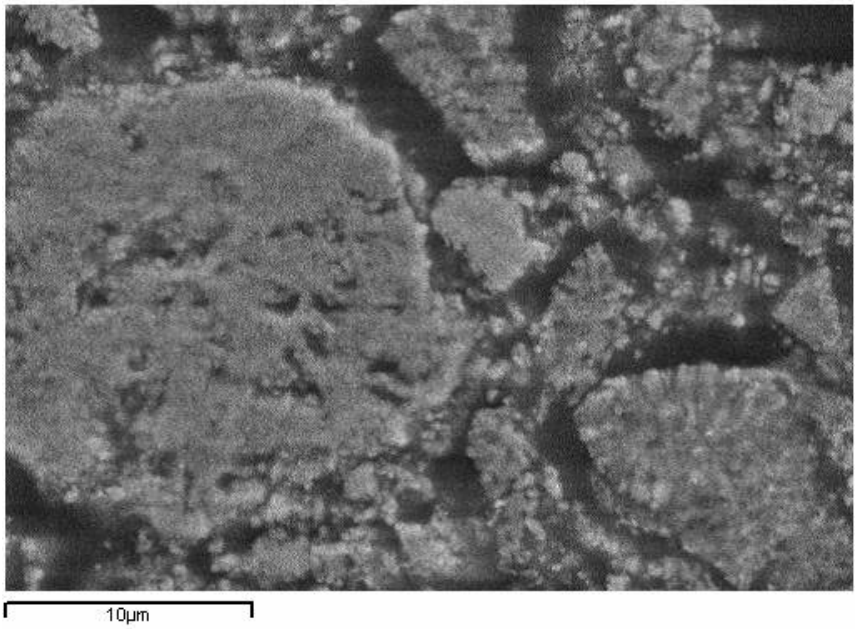

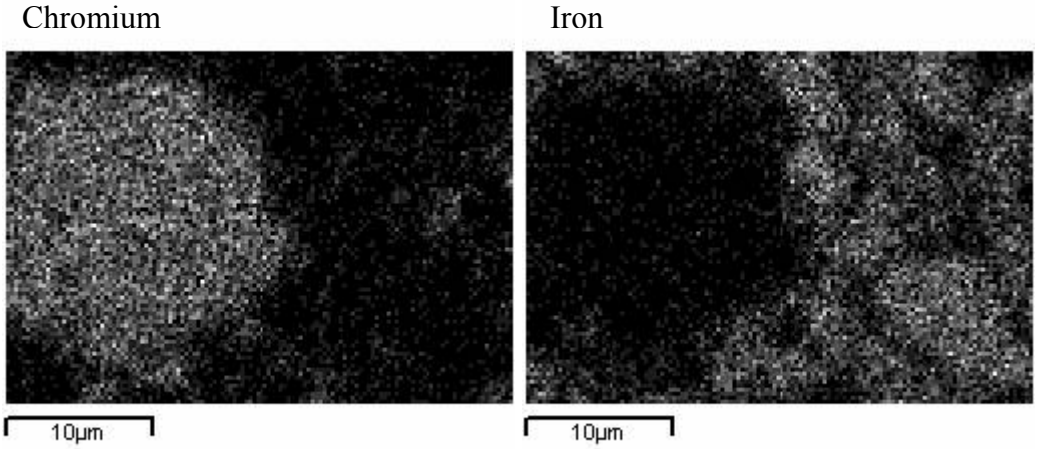

Figure 5.10: SEM image of a cross-section of a partially reduced iron-chromium sample (5wt% chromium) heat-treated to 600°C with corresponding EDS maps for chromium and iron.

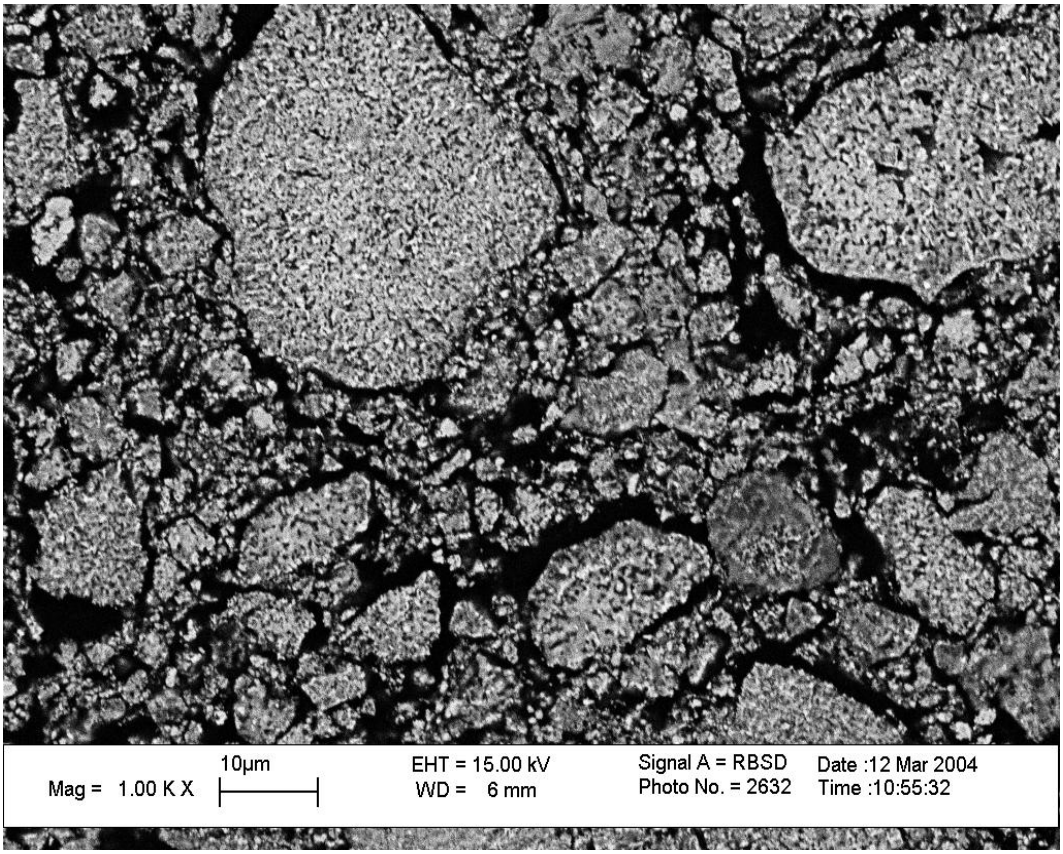

Figure 5.11: Polished cross-section of a partially reduced iron-chromium sample (5wt% chromium) heat-treated to 600°C.

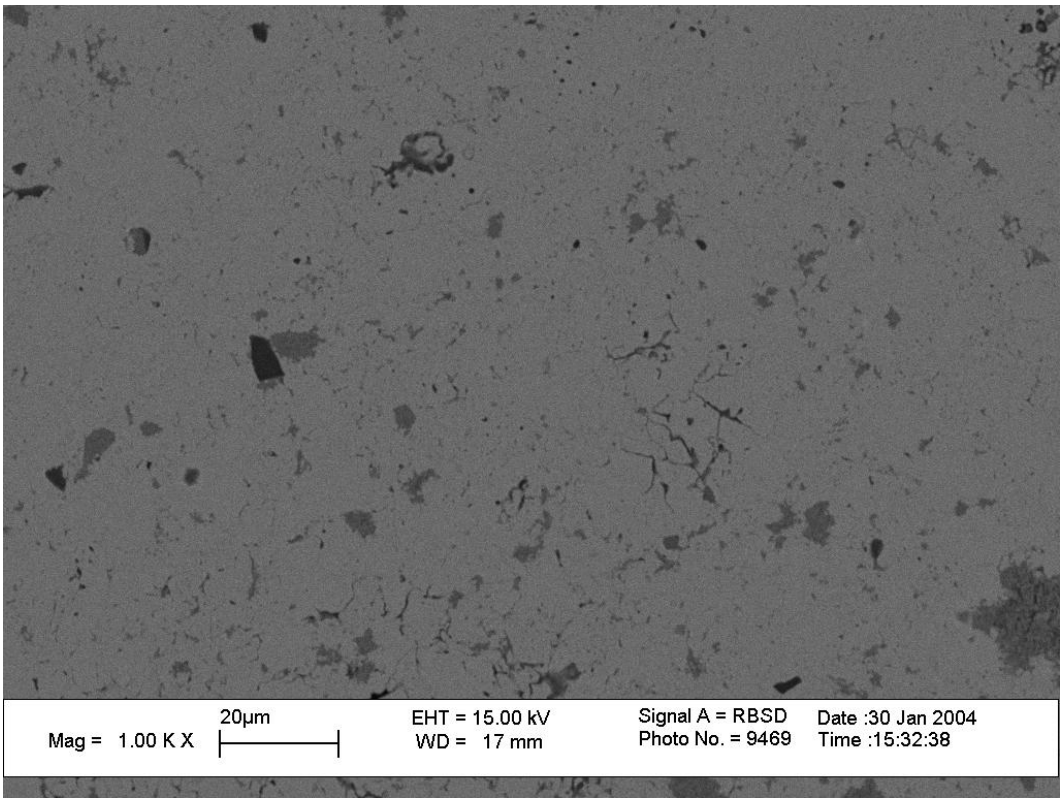

Figure 5.12: Polished cross-section of a partially reduced iron-chromium sample (5wt% chromium) heat-treated to 800°C.

also increased. This interconnectivity inhibits the sintering of the reduced iron phase so that sufficient densification of the iron phase is delayed. This continues until enough chromium oxide is reduced so that the interconnectivity is eliminated. Reduction is also inhibited because a smaller ratio of the existing chromium oxide is in contact with the iron matrix. As a result, the ability of the presence of iron to aid in chromium oxide reduction [14] by transporting chromium away from the unreduced chromium oxide is limited.

In the 15wt% samples, the iron matrix did not sinter enough to be significantly differentiated from the chromium oxide until about 900°C, although this was observed at 800°C for the 5wt% samples. At 900°C the visual differences between iron and the chromium oxide became more obvious (see Figure 5.13), although the chromium oxide present is still very interconnected. This is because the islands of iron matrix separated by the chromium oxide became denser. The microstructure of the 25wt% samples heat-treated to 1000°C was still similar to that of the 5wt% sample heat-treated to 700°C (see Figure 5.14). This was also a result of the interconnectivity of the chromium oxide phase, which occurs to a greater extent in these samples than in the either the 5wt% or the 15wt% samples.

Also interesting to note is that no chromium oxide particles were found in the 5wt% samples at 1100°C and above (see Figure 5.1), while some particles remained up to a heat-treatment temperature of 1300°C for both the 15wt% and 25wt% samples. This observation corroborates results obtained by Nadler [6], as shown in Figure 2.4. The amount of chromium that was in solution for the 5wt% samples reached a

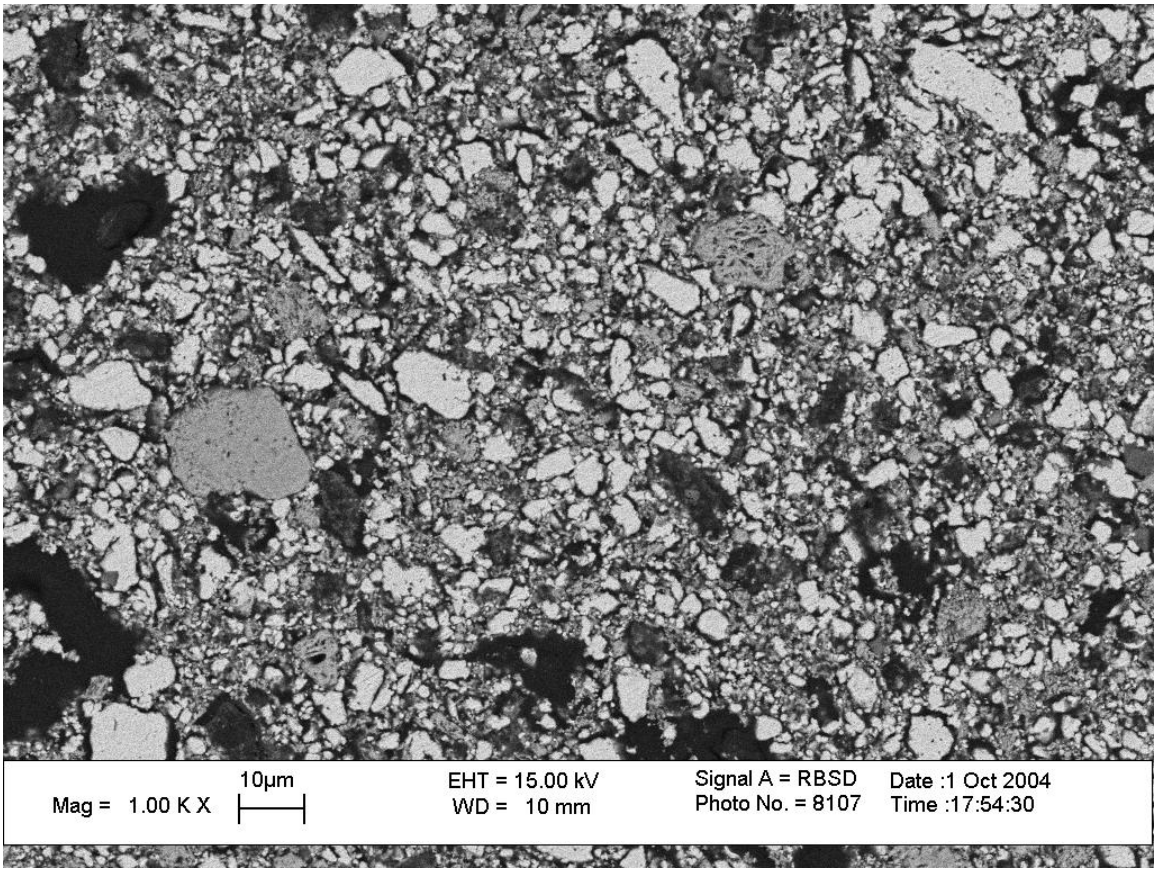

Figure 5.13: Polished cross-section of a partially reduced iron-chromium sample (15wt% chromium) heat-treated to 900°C.

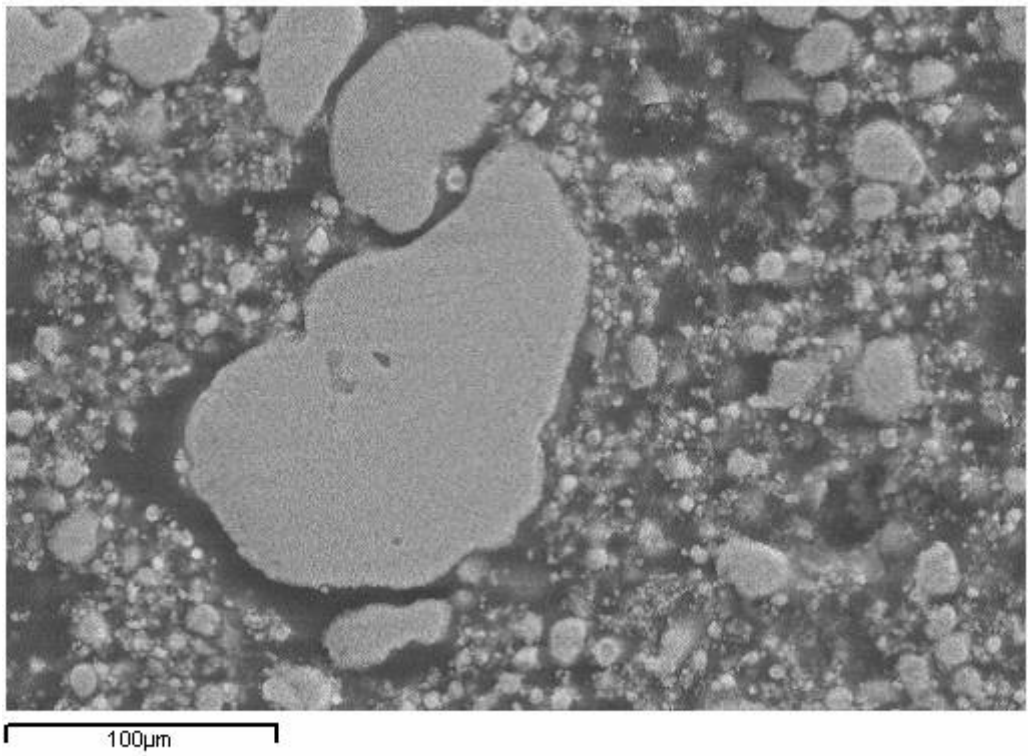

Figure 5.14: Polished cross-section of a partially reduced iron-chromium sample (25wt% chromium) heat-treated to 1000°C.

maximum by 1100°C, whereas this was not the case for samples with a higher input concentration of chromium oxide.

The densification of the iron matrix was affected by the amount of unreduced chromium oxide present. Increasing the chromium oxide content decreases the ability of the iron matrix to sinter. In addition, increasing the chromium oxide content means that the interconnectivity of that phase was increased, especially at lower heat-treatment temperatures. As a result, the contact that the oxide had with the iron matrix was limited. Any way in which the presence of iron aids the reduction of chromium oxide was therefore suppressed. This was seen from the fact that all of the oxide present in the 5wt% samples was reduced by 1100°C, and this was not the case for the higher compositions. Oxide particles remained past heat-treatment temperatures of 1300°C in the samples of higher composition because other factors such as sintering in the iron matrix and interactions with impurities inhibited reduction. These issues will be discussed in Sections 5.4 and 5.5.

5.2.2 X-Ray Diffraction

X-ray diffraction was performed on the 15wt% samples heat-treated to each temperature. Precise lattice parameter analysis of the resulting diffraction patterns showed an increasing lattice parameter with increasing heat-treatment temperature. The lattice parameters calculated for the samples at each heat-treatment temperature were converted to chromium composition in iron using the work of Pearson [59]. This trend is shown in Figure 5.15. Table 5.1 gives the values used in this plot. The increasing

Table 5.1 Composition of chromium in the iron matrix at each heat-treatment temperature derived from the measured lattice parameters.

Heat-treatment Temperature (°C)	Lattice Parameter (Å)	Composition (weight fraction)
600	2.8667	0.00898
700	2.8668	0.0111
800	2.8669	0.0128
900	2.8678	0.0302
1000	2.8706	0.1005
1100	2.8717	0.1559
1200	2.8716	0.1492
1300	2.8718	0.1578

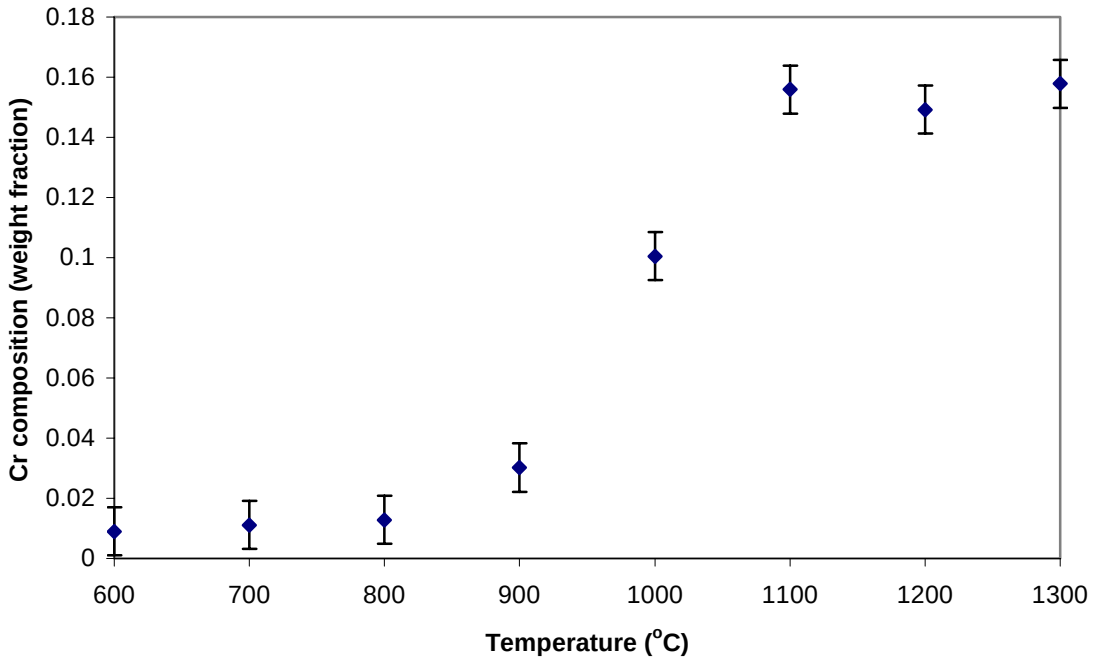

Figure 5.15: Plot of the composition of chromium in iron vs. heat-treatment temperature for 15wt% samples. The composition was calculated from lattice parameter measurements using data obtained from the work of Pearson [59].

chromium content of the iron matrix is a result of the product of chromium oxide particle reduction being incorporated into the iron matrix. The rate of uptake of chromium into the iron was also shown to be increasing with increasing heat-treatment temperature. This is a result of increasing reduction kinetics occurring at the higher temperatures. The intake of chromium into the iron matrix plateaus after 1100°C due to factors limiting the complete reduction of the remaining oxide. The inhibition of the reduction reaction comes as a result of the sintering of the iron matrix around the particle and the interaction of the particle with impurity compounds.

5.3 Effect of Matrix Sintering on the Composition at the Chromium Oxide/Iron Interface

As the density of the iron matrix increases around the chromium oxide particles, the ability of the gaseous reactants and products to diffuse to and away from the particle is hindered. This results in the partial pressure ratios of hydrogen to oxygen (P_{H_2}/P_{H_2O}) decreasing at the reducing interface as the matrix density increases.

Gurevich *et al*. [14] has presented equilibrium equations for the reduction of chromium oxide in contact with iron. These equations have been used to relate concentration of chromium in iron that is in equilibrium with reducing chromium oxide to (P_{H_2}/P_{H_2O}) at different temperatures. Figure 5.16 shows the results of these equations. As the temperature increases, the equilibrium chromium composition increases for the same P_{H_2}/P_{H_2O}. Included on these plots are the compositions of chromium in iron measured at the interface of an iron and chromium oxide diffusion couple at different temperatures by Nadler [6]. When the measured composition at the

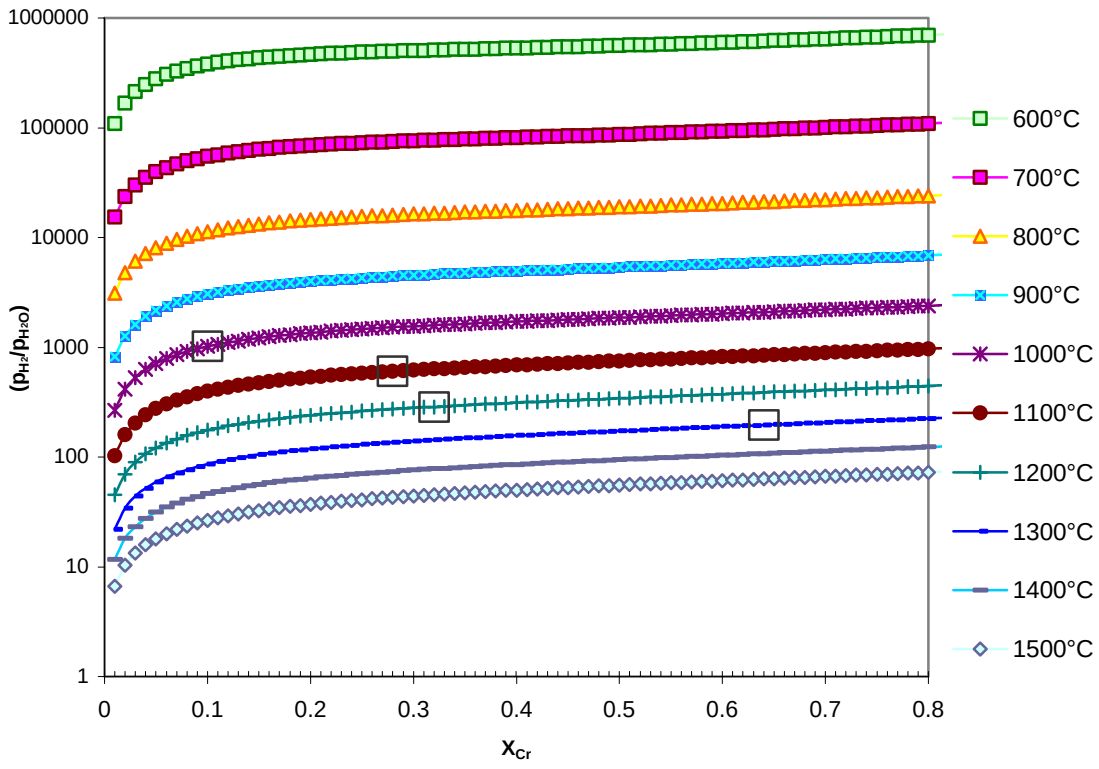

Figure 5.16: The compositions of chromium in iron that is in equilibrium with water, hydrogen and reducing chromium oxide. The equilibrium composition is plotted for changing partial pressures of hydrogen and water, P_{H_2}/P_{H_2O} at various temperatures. The equations for these plots are taken from [14]. The black squares denote measured interface composition values for a diffusion couple of reducing chromium oxide and iron at various temperatures. These data points are taken from Nadler [6].

interface and the equilibrium composition of chromium in iron for different P_{H_2}/P_{H_2O} were related, the P_{H_2}/P_{H_2O} at the site of reduction was shown to decrease as the temperature increased. This is shown more clearly in Figure 5.17, as this relation is plotted as P_{H_2}/P_{H_2O} versus temperature.

These results show that in this system, the P_{H_2}/P_{H_2O} at the chromium oxide iron interface decreases as the heat-treatment temperature increases. This is a result of the fact that the sintering of the iron matrix prevents hydrogen from being transported to the reduction site and the H_2O produced from escaping. This matrix environment therefore affects the interfacial composition, which would also affect the dissolution of the chromium oxide particle.

5.4 Isothermal vs. Non-Isothermal Heat-Treatments

5.4.1 Sintering Effects

Heat-treatments were performed with the heating rates outlined in Section 4.2 to temperatures of 800°C and 1000°C. Hold times of 0, 10 and 100 minutes were used. Microstructural observations show a marked difference in the interaction of the chromium oxide particle with the iron matrix between samples that have not experienced isothermal holds and those that have.

In Figure 5.18, one can see that chromium oxide particles in the sample that has been heat-treated to 1000°C without undergoing an isothermal hold are imbedded

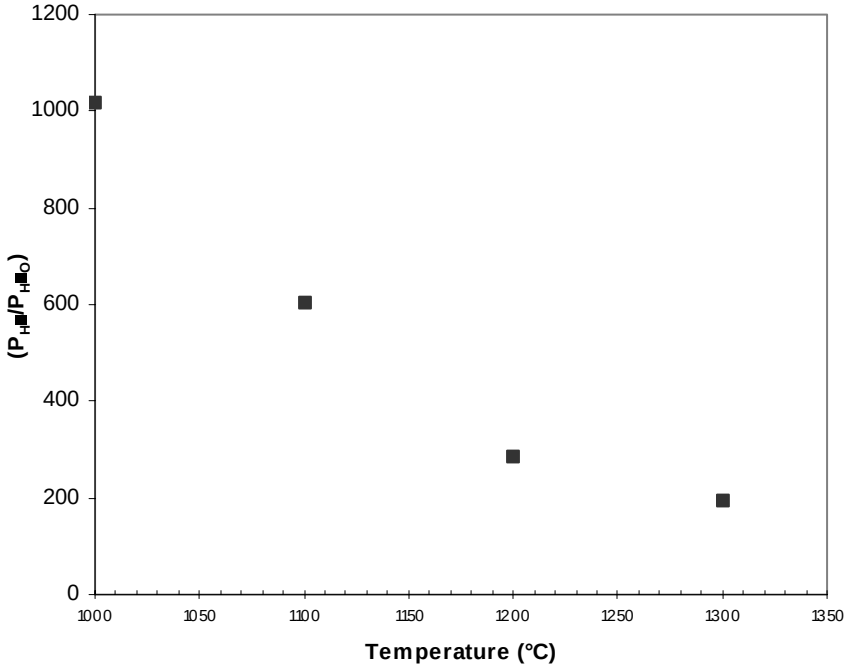

Figure 5.17: The equilibrium partial pressures of hydrogen and water, P_{H_2}/P_{H_2O} at the site of chromium oxide particles being reduced in iron at various heat-treatment temperatures.

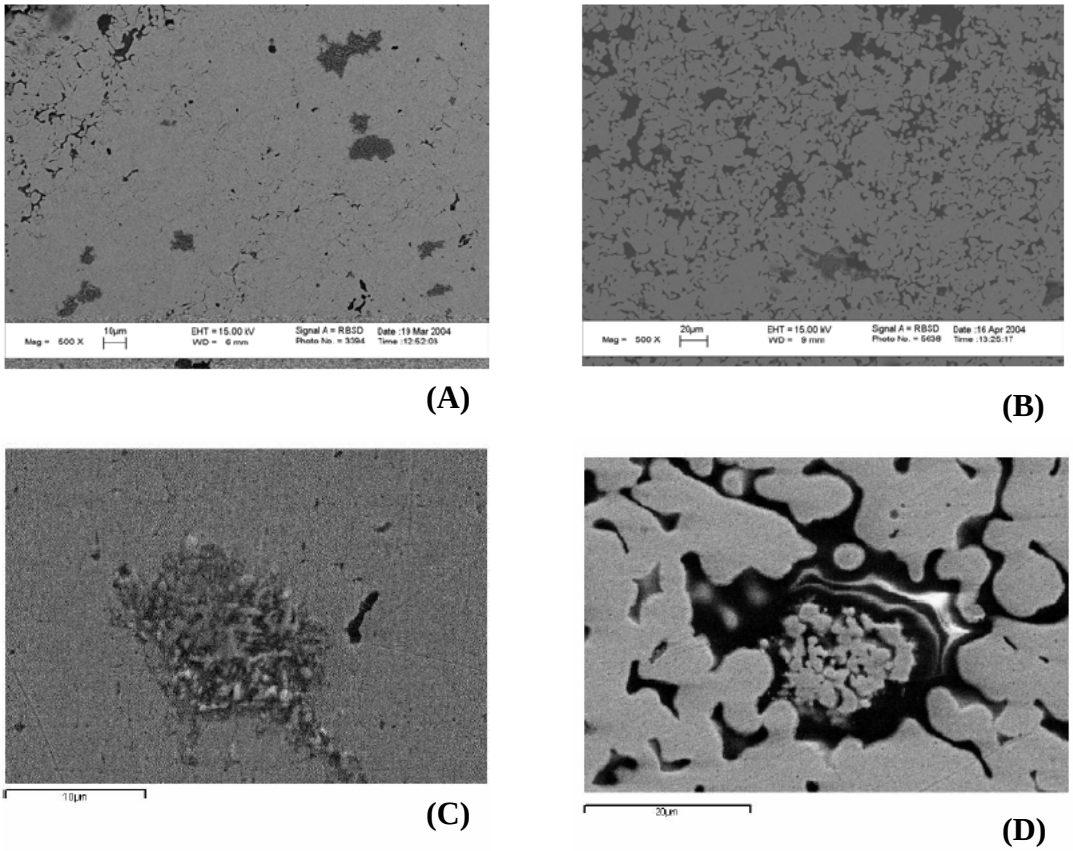

Figure 5.18: Iron-chromium samples (5wt% chromium) heat-treated to 1000°C. (A) and (C) are from the sample that had no hold time. (B) and (D) are from the sample held isothermally for 10 minutes. (A) and (B) reveal the microstructure of each sample and (C) and (D) images show magnified views of individual particles from each sample, respectively.

firmly into the iron matrix. On the other hand, the sample with a subsequent isothermal hold shows chromium oxide particles that are much more loosely attached to the surrounding matrix. As the chromium oxide continues to reduce at a constant temperature, the particles are observed to shrink away from the surrounding matrix. The relaxation in the sintering of the iron matrix upon reaching isothermal conditions (see Section 2.5) has allowed the shrinkage due to the reduction of the chromium oxide particle to overtake the shrinkage of the surrounding matrix upon the particle.

5.4.2 Reduction Effects

Image analysis was performed to obtain the volume fraction of chromium oxide particles remaining in various samples. Some of these samples were heat-treated at a rate of 5°C/minute to 1000°C, 1100°C, 1200°C and 1300°C then quenched, while others were heat-treated to 1000°C then held isothermally. Figure 5.19 shows the results of the change in volume fraction of chromium oxide particles with heat-treatment time both for samples held isothermally and those that are not. The heat-treatment time for each sample is measured after a temperature of 1000°C is reached.

These results show that initially, over the same time period, the decrease in the volume fraction of chromium oxide particles is larger for samples heat-treated isothermally from 1000°C than for those whose temperatures are continuously increasing. Despite the increasing temperatures, which would normally increase reduction kinetics, the samples that are heat-treated under non-isothermal conditions show a smaller reduction of chromium oxide content. Compared to the output from a

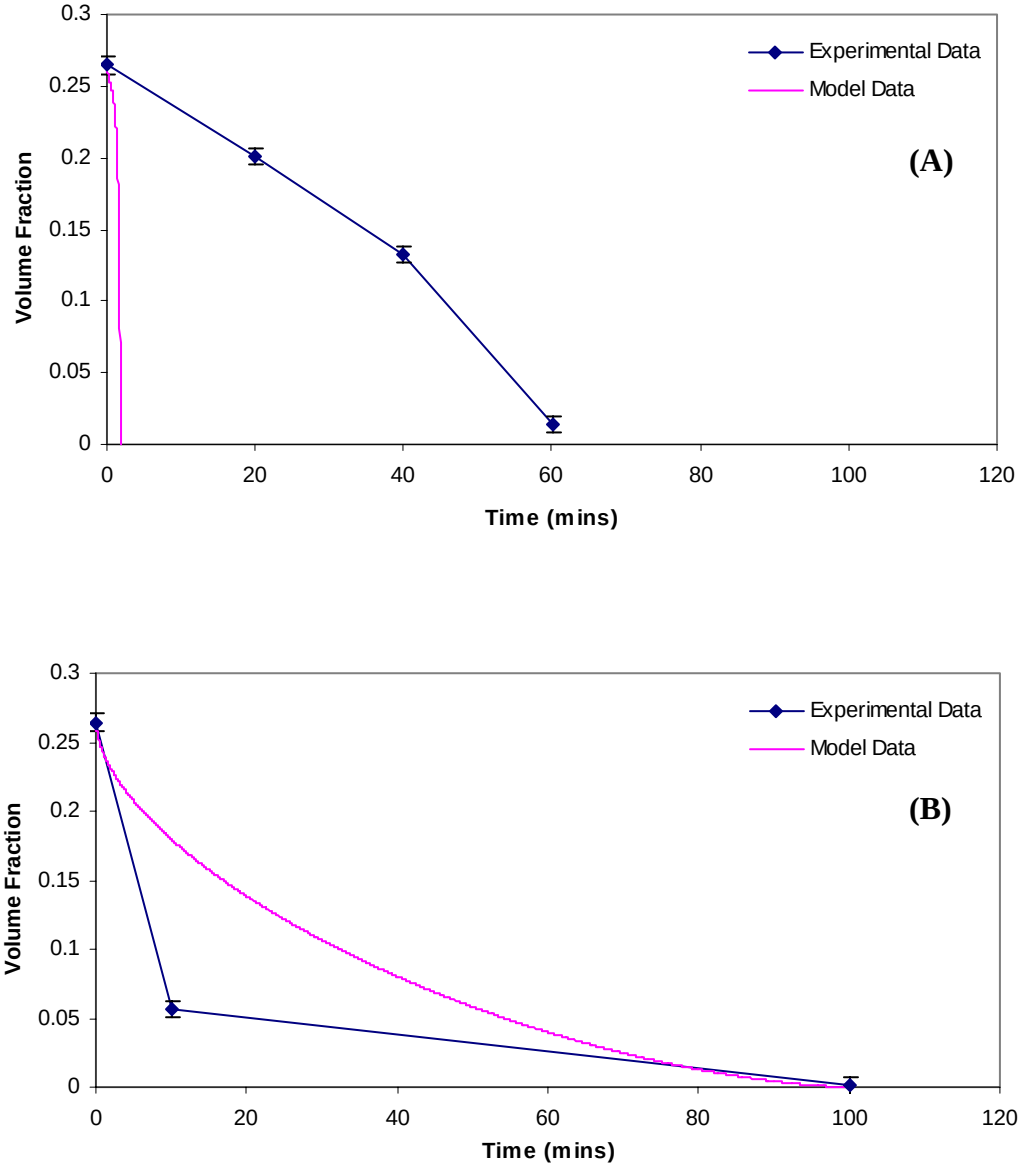

Figure 5.19: The change in volume fraction of chromium oxide for (A) samples heat-treated under a constant heating rate of 5°C/min from 1000°C and quenched at 1000°C, 1100°C, 1200°C and 1300°C and (B) samples heat-treated at 1000°C isothermally and quenched at 0, 10 and 100 minutes. The time for each sample is measured after a temperature of 1000°C is reached.

simple dissolution (also shown in Figure 5.19), these results show that the reduction of the chromium oxide is not based solely on dissolution kinetics.

The model, as explained in Appendix B, calculates the rate of dissolution of a particle based on the particle size and the diffusivity of chromium (the diffusing species) in the iron matrix. Since all the particles are assumed to have the same size, the change in particle radius is easily converted to change in volume fraction.

The results of the model for samples that were heat-treated non-isothermally show that the particles should have dissolved far sooner than they actually did. For the samples that were heat-treated isothermally, the dissolution time of the model, almost matches the dissolution time obtained experimentally. It should also be noted that the though the model predicted the time to complete dissolution very well, the experimental values lie below the curve generated by the model. This is due the fact that the model only takes into account one particle size when in reality there is a distribution of particle sizes present, as will be discussed in Section 5.4.2.1. To generate these results, the largest particle size was used in order to predict the most accurate final dissolution time. The dissolution rate of each particle is dependent on the size of the particle, with smaller particles dissolving at a faster rate than larger particles. Therefore, the experimental volume fractions decreased faster than the predicted values at intermediate times as the smaller particles present are more quickly eliminated.

One of the reasons the model predicted dissolution of the particles in the samples heat-treated isothermally better than those heat-treated under a constant heating rate is that there are different rates of sintering experienced by the iron matrix for each heat-treatment regime. As shown in Figure 5.8, the densification of the iron

matrix achieved is greatly enhanced by having an increasing heat-treatment temperature versus having an isothermal hold. As a result, the porosity surrounding the chromium oxide particles in the iron matrix is greatly reduced. This means that the ability of hydrogen and water vapor to be transported to and away from the chromium oxide particle is hindered. Therefore, though the temperature is increased, the reduction kinetics is slowed. As a result, the dissolution of the chromium oxide particle into the metal is hindered.

Though increasing temperatures should produce increasing reduction kinetics of chromium oxide in iron, the sintering effects of having a heating rate on the iron matrix means that reduction can occur more readily when holding at an intermediate temperature. The increased densification of the iron matrix due to having a heating rate means that the matrix densely surrounds the oxide particle. More of the surface of the particle is in contact with the iron, but gaseous transport essential for reduction is hindered. Conversely, having an isothermal hold means that the particle surface is not extensively in contact with the iron matrix, but the porosity does allow for better gaseous transport.

5.4.2.1 Chromium Oxide Particle Reduction Under Isothermal Conditions

Using image analysis software, the particle size distributions of the heat-treated samples were obtained. The particle size distributions for the 15wt% samples heat-treated to 1000°C and held for 10 and 100 minutes are discussed here. Heat-treatments without a hold times and at 800°C with a hold time of 10 minutes were also performed,

but the interconnectivity that remained in the chromium oxide phase prevented particle size analysis to be performed.

The number and size of the largest particles are drastically reduced from the sample heat-treated for 10 minutes to the sample heat treated for 100 minutes. Appendix C contains the particle size distribution data for these conditions. The average particle size obtained from using Saltykov's method though is larger for the longer heat-treatment time, 4.815μm for 100 minutes, as opposed to 1.523 μm for 10 minutes. One reason for this may be the limitations of the image analysis software and the ability of Saltykov's method to account for these limitations. For the longer heat-treatment time, the smallest size class used is smaller that the smallest particle size that can be measured with the image analysis software. This is true even when using the smallest recommended number of classes. The size of the class is the size of the largest particle divided by the number of classes that will be used. On the other hand, for the heat-treatment of 10 minutes, with the largest particles being as large as they are, the maximum number of classes is used without the smallest class being smaller than the smallest measurable particle. Also, far fewer particles remain after the 100 minutes heat-treatment, so the statistical accuracy of the particle size distribution after this heat-treatment is much smaller with respect to the 10 minutes heat-treatment.

That said, the results here are not inconsistent with results of dissolution experiments where a distribution in particle sizes is present. The dissolution velocity of a particle is given by [48, 49, 54]:

$$\frac{dR}{dt} = -k\left[\frac{D}{R} + \left(\frac{D}{\pi t}\right)^{\frac{1}{2}}\right] \qquad [5.1]$$

This equation is for the diffusion-limited rate of dissolution of a particle in a matrix. The particle's dissolution speed depends on the size of the particle. Appendix C contains more information on this equation and how it is used to model dissolution later in this Section. This equation shows that smaller particles would dissolve faster than larger particles. This is because the smaller particles have a much larger surface area to volume ratio. As chromium oxide is reduced to chromium metal, a larger ratio of chromium atoms can be detached from a smaller particle surface and dissolved than from a larger particle.

Even though the largest particles present in the 10-minute heat-treatment are much larger than those in the 100-minute heat-treatment, there are far more of the smallest particles. Therefore, the mean of the particle size distribution is weighted heavily on the side of the smaller particle. As these smallest speedily dissolve and are eliminated, the larger particles don't decrease in size as quickly. As a result, the average particle size can be expected to increase, although the size of each particle, and the number of particles, is drastically reduced. Figure 5.20 shows the chromium oxide particle size distributions for each of the hold times. The wider size distribution of the 10-minute heat-treatment is shown with the majority of particles being smaller in size. The narrower size distribution of the 100 minutes heat-treatment is also shown. The number of smaller particles relative to larger particle is greatly reduced and the mean particle size increases.

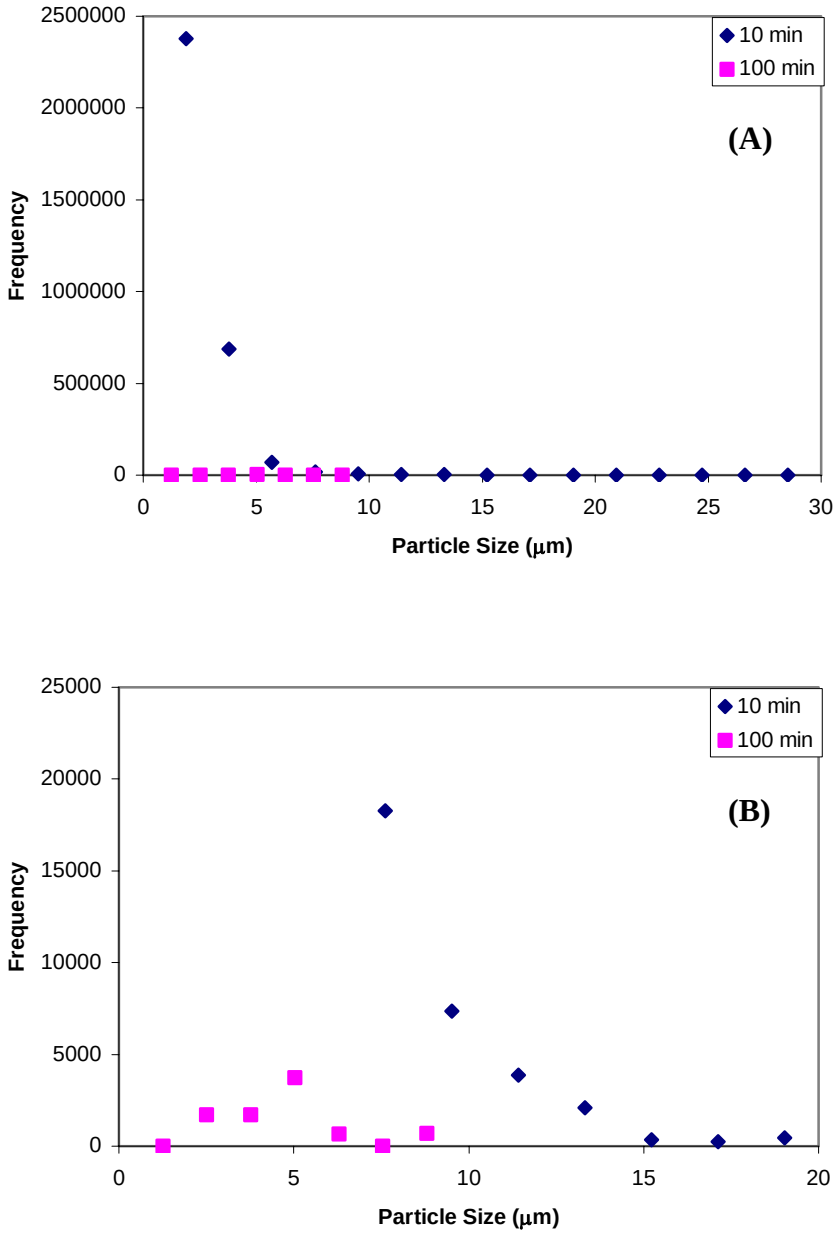

Figure 5.20: The relative frequencies of chromium oxide particle size for 15wt% samples heat-treated at 1000°C for 10 and 100 minutes are shown. **(B)** is an enlargement of **(A)** since the number of particles for the 100 minutes heat-treatment is far smaller that the number of particles for the 10 minutes heat-treatment.

5.5 Role of Impurities in the Reduction of Chromium Oxide Particles

For the 15wt% sample heat-treated to 1300°C, a few chromium oxide particles were found to remain. EDS mapping revealed that silicon and calcium impurities were concentrated in areas surrounding unreduced particles, as shown in Figure 5.21. The chromium oxide particle appears to be sealed off from complete reduction as a result of the presence SiO_2 and CaO.

There are eutectic reactions present in the iron-silicon system that could produce a liquid at temperatures as low as 1203°C [35], see Figure 5.22. During heat-treatment at this temperature the eutectic liquid formed would coat the chromium oxide particle, effectively sealing it off from the iron matrix. Also, with enhanced sintering, as a result of the present liquid phase, the region around the chromium oxide particle would be densified such that porous channels around the chromium oxide particle are sealed off, inhibiting hydrogen from reaching the particles and H_2O from leaving. Final densification of iron while there still remains unreduced chromium oxide particles has been shown to be an effective barrier to gaseous transport in samples of thicker dimensions [16, 60].

In the Cr_2O_3-CaO system there exists a eutectic reaction that occurs at 1022°C. [61], (see Figure 5.23). This temperature is lower than the temperature at which the eutectic reaction in the iron-silicon system occurs. It is therefore possible that a chromium oxide particle that comes into contact with a CaO particle can react to form a pocket of liquid in the compact that later solidifies on quenching.

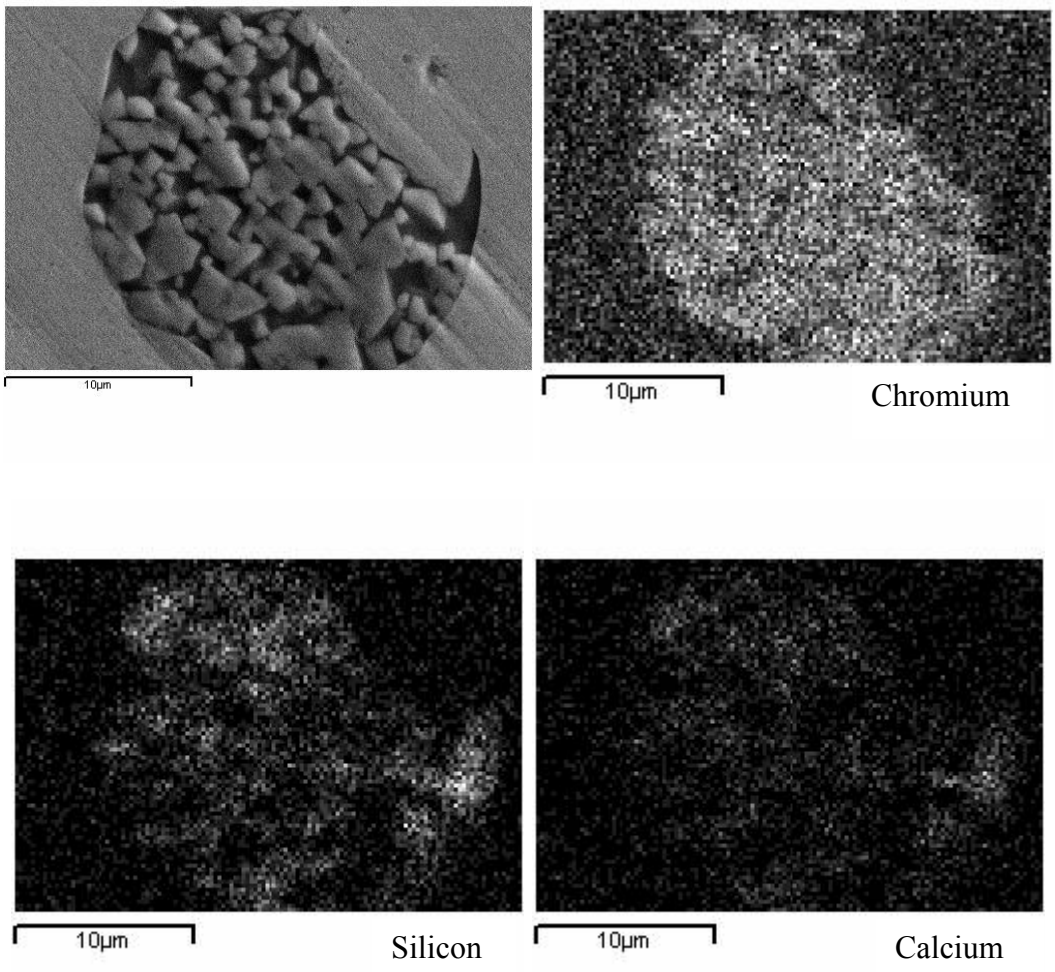

Figure 5.21: SEM image and EDS maps of chromium, silicon and calcium, respectively, in the region of a chromium oxide particle for a 15wt% sample heat-treated to 1300°C.

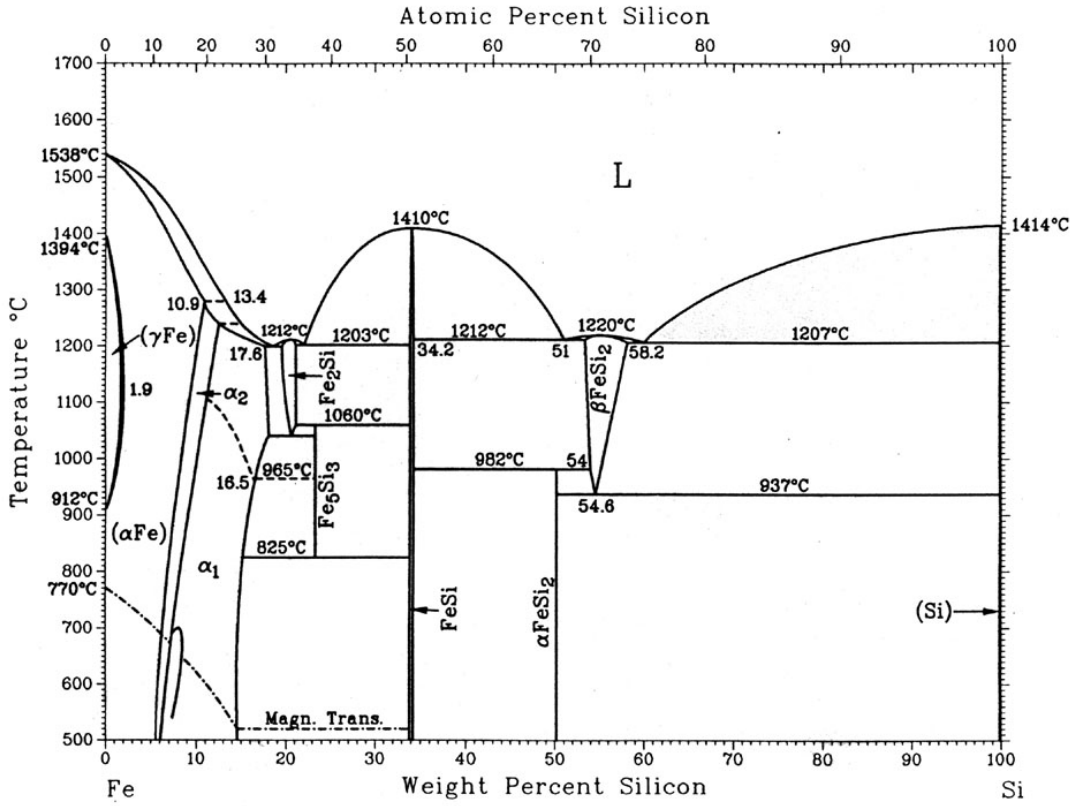

Figure 5.22: Phase diagram of the iron-silicon system taken from the ASM Handbook [35].

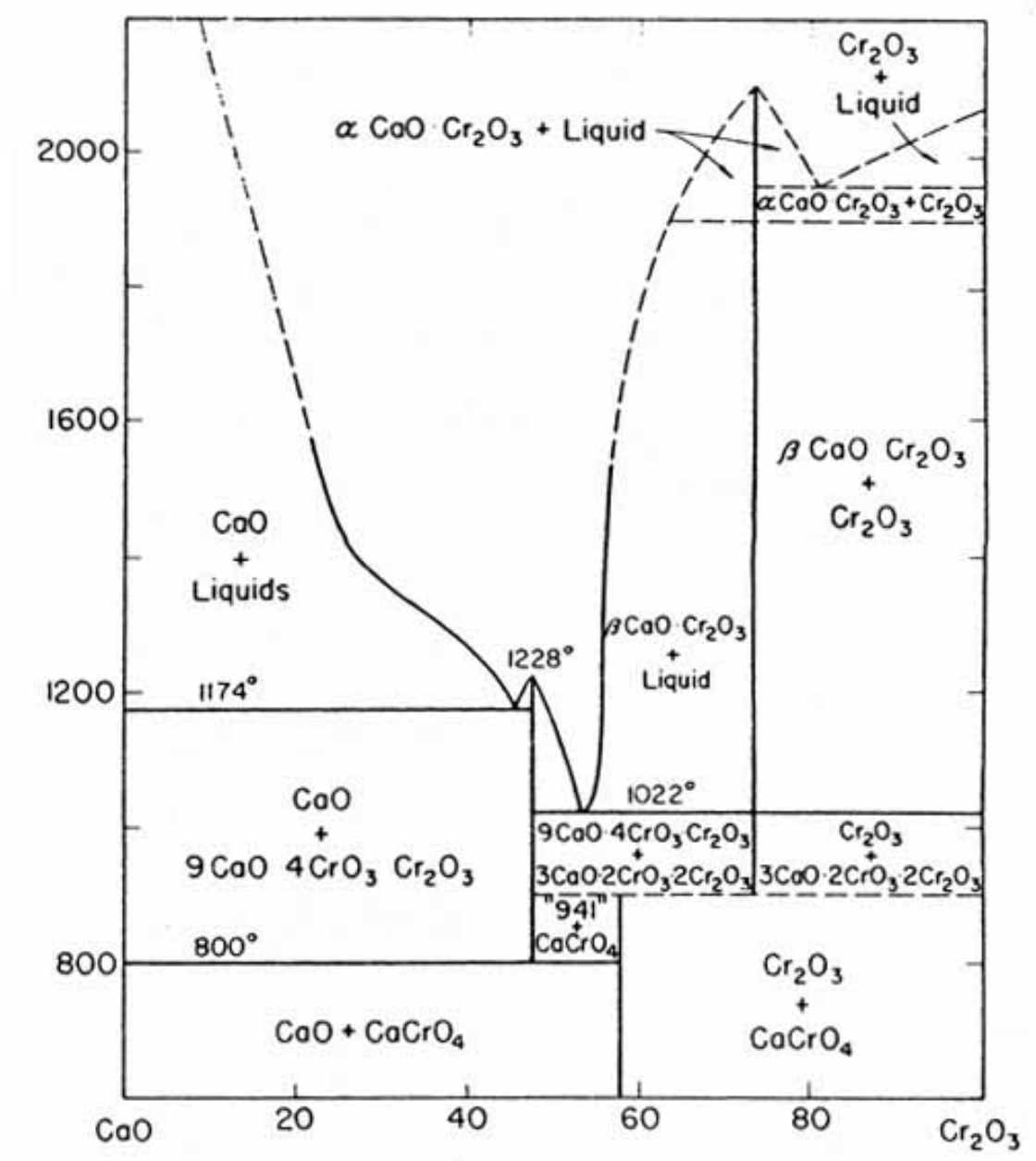

Figure 5.23: Phase diagram of the CaO-Cr_2O_3 system taken from Levin *et al.* [61]. All temperature values are in degrees Celsius.

According to previous work [6], the silicon and calcium impurities surrounding the chromium oxide particle are made up of two layers. The layer closest to the chromium oxide particle was calcium rich and the outer layer was silicon rich. It follows that the calcium oxide impurities first interact with the chromium oxide particles forming the inner layer and the silicon impurities interact with the matrix producing the outer layer.

The faceted appearance of the chromium oxide particles that remain in these regions of impurities tend to suggest that solidification from a melt has taken place. When solidification of certain types of materials occurs, faceted growth takes place where there is an anisotropy in the growth rates of the different crystallographic planes. This results in a crystal like appearance of the solidified structure, which has surfaces bounded by the slowest growing planes [62]. Heating a solid to extreme temperatures tends produce to a reduction in curvature and surface area, so it appears that at the time of quenching there was a melt that solidified in that region. The faceted chromium oxide crystals are bounded by a glassy phase, which contains silicon and calcium as well as other impurities like aluminum, magnesium and titanium see Figure 5.24. This becomes an effective barrier against further reduction.

Though chromium oxide particles remain in the 15wt% samples heat-treated to the highest temperatures used, lattice parameter calculations show that after a temperature of 1100°C, the composition of chromium in iron has changed by very little. (See Figure 5.15.) This means that the interaction the chromium oxide has with impurities that most affects its ability to reduce most likely occurs before this temperature.

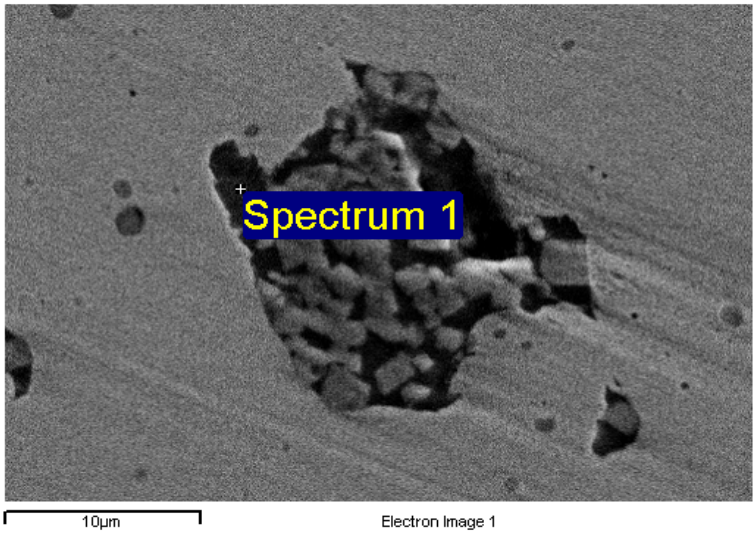

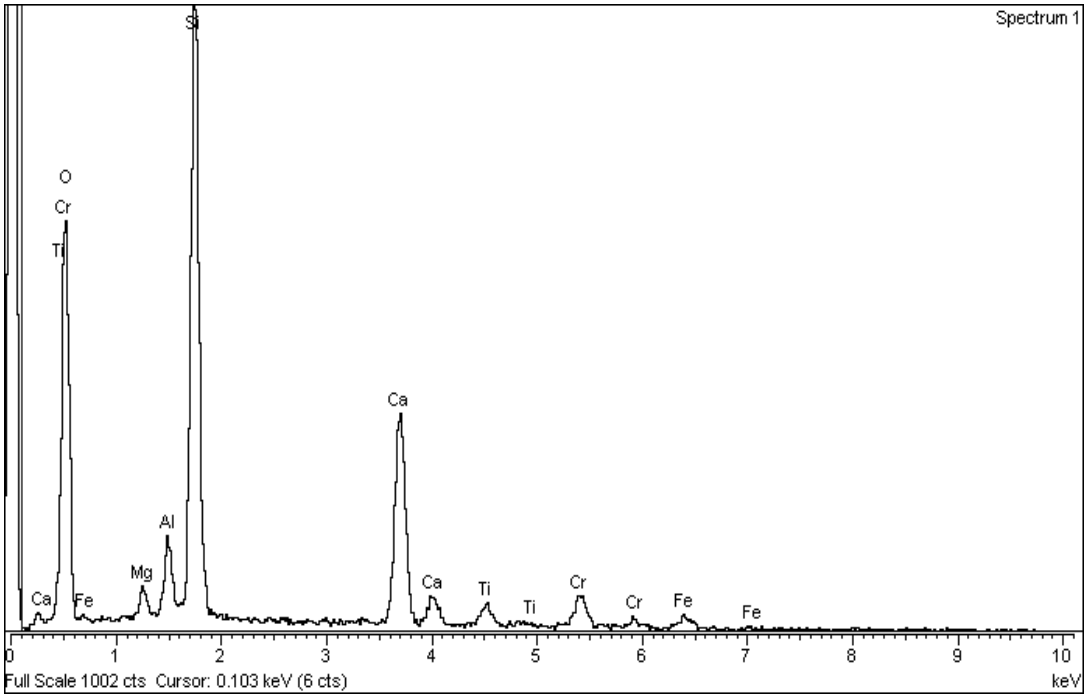

Figure 5.24: SEM image showing glassy phase surrounding chromium oxide particle for a 15wt% sample heat-treated to 1300°C and corresponding EDS point scan of the region indicated.

In samples that were held isothermally, a titanium oxide impurity was found to surround some metal particles. Unlike the case above where the impurities surrounded and effectively blocked the unreduced chromium oxide particle from further reduction, it seems that the particles surrounded by titanium oxide are allowed to reduce. (See Figure 5.25.) There is porosity around the metal particles imbedded in the impurity and in the impurity itself. This would allow further reduction to occur. Impurities surrounding particles in samples that were not held isothermally did not have this porosity and so remained as oxide particles.

At temperatures above 1000°C, remaining oxide particles start interacting with impurities in the sample. As a result, phases are produced that shield the oxide particle from further reduction and also liquid phases that enhance sintering in the matrix surrounding the particle. When samples are held isothermally at this temperature, these chromium oxide-impurity interactions do not occur. Therefore, the presence of impurities in samples held isothermally does not inhibit the reduction of chromium oxide as it does is samples heat-treated above 1000°C under a heating rate.

5.6 Chromium Oxide Dissolution

The profiles of the composition distribution of chromium in iron were measured in samples containing chromium and chromium oxide particles. Point scans were taken radiating outward from the center of the particles. Figure 5.26 shows the dissolution profiles of chromium and chromium oxide particles in samples that were heat-treated in the same manner. The data show that in both cases the interfacial compositions, C_I, were similar. In the case where chromium oxide is reduced to the metal and is then

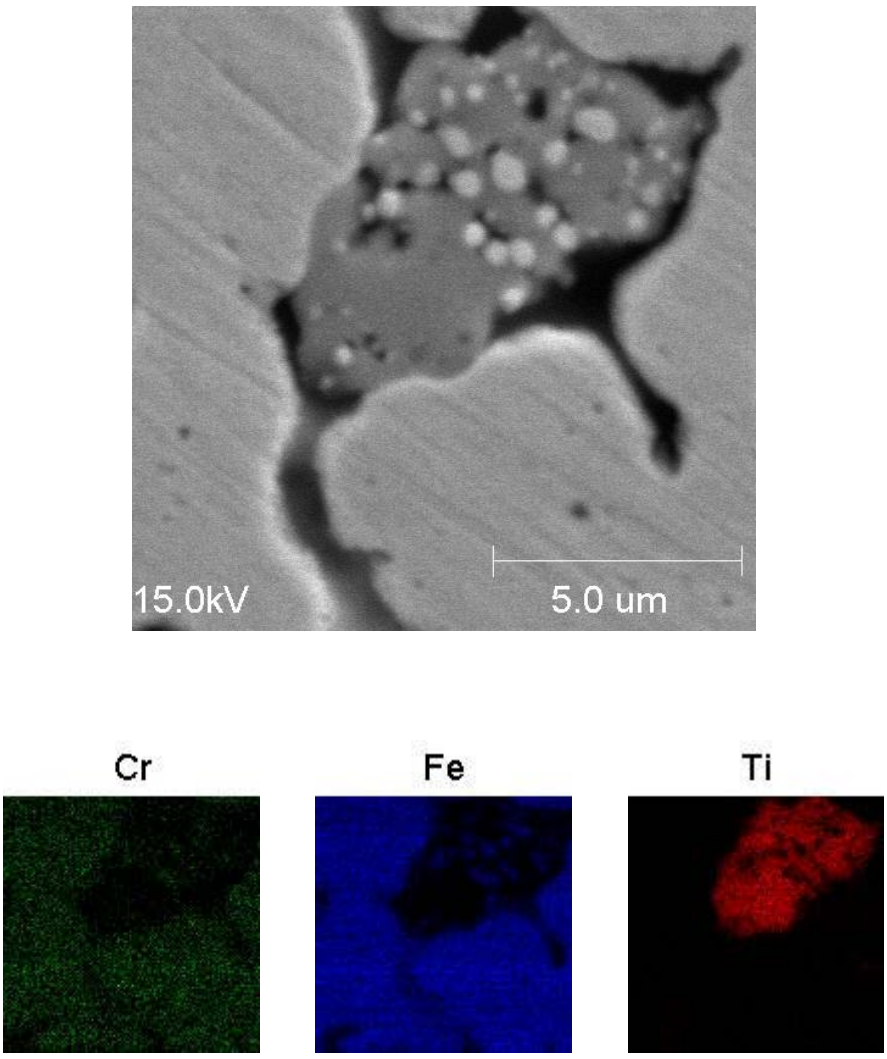

Figure 5.25: SEM Image of TiO_2 impurity and the iron, chromium and titanium dot maps taken in that region for a sample heat-treated to 1000°C then held isothermally for 10 minutes.

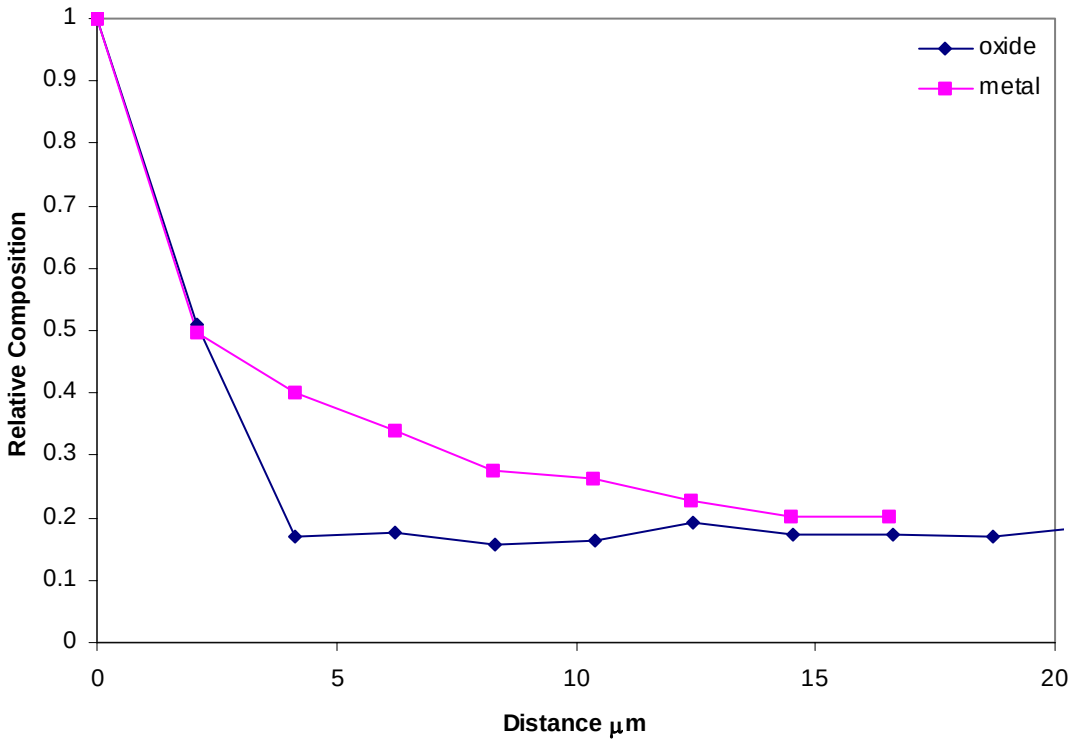

Figure 5.26: Composition distribution of chromium away from particles of chromium oxide and chromium metal for 15wt% samples heat-treated to 1000°C and held for 10 minutes.

dissolved into the matrix, there is a smaller uptake of iron into the matrix than for the case where chromium metal is just being dissolved into the iron. This means that the transformation of the oxide to the metal is a limiting factor in the dissolution of chromium oxide in the iron matrix. This is evidence that the dissolution of chromium oxide into iron is interface controlled or at least mixed control.

5.7 Results Summary

The results of the sintering model for iron heat-treated under a heating rate matched well with experimental values obtained by Nadler [6]. When the model was run for the case, including an isothermal hold, the shrinkage predicted was considerably decreased at the start of the isothermal hold. The results of the sintering model run for nickel matched reasonably well with the experimental data. A very low start temperature must be used to accommodate the calculation of sintering for a small particle size. This is because the materials parameters for nickel, used in the model produces a sharp initial increase in the neck growth rate that would otherwise terminate the program.

Portions of iron oxide/chromium oxide honeycombs of various compositions were heat-treated to temperatures above 600°C. At this temperature the iron oxide is mostly reduced to the metal and chromium oxide remains. For all the compositions, the oxide phase became more distinct from the iron matrix as sintering of the iron matrix eliminated a sufficient amount of porosity. The chromium oxide in samples with higher chromium content (15wt% and 25wt%) remained very interconnected in the iron matrix. As a result the onset of sintering in these samples was delayed.

XRD showed the chromium content in the matrix of the 15wt% samples reached a plateau at heat-treatment temperatures of 1100°C and above. Microstructural data showed that unreduced chromium oxide particles still remained in the samples heat-treated under a constant heating rate up to 1300°C.

Experimental data of the reducing chromium oxide particles in samples that were held at 1000°C compared well with the generated dissolution model for these samples. Experimental data was also taken from samples that were heated-treated under a constant heating rate. When this data was compared to the data generated from the model, it was shown that the reduction rate was much slower than predicted. This result shows the effect that the heating rate has on the ability of the chromium oxide particles to reduce in an iron matrix.

EDS analysis also showed that impurities, mostly silicon and calcium compounds concentrated around the particles that remained. The sintering of the iron matrix for these samples was enhanced due to non-isothermal heating. The combination of the chromium oxide interaction with impurities and the densification of the matrix around the particle inhibited complete reduction.

The composition distributions of chromium in iron taken away from particles of chromium oxide and chromium metal for similar heat-treatments were compared. The composition profile measured for the oxide particle showed that there was a smaller intake of chromium into the iron matrix. The reduction reaction of the oxide going to metal played a limiting factor in the overall dissolution of the particle.

CHAPTER 6

CONCLUSIONS

The goal of this research was to follow the reduction of chromium oxide by hydrogen in an iron matrix, and determine the microstructural features that affect reduction in iron-chromium honeycombs. It was found that the dissolution of chromium oxide into iron is limited by the reduction of the oxide to the metal at the chromium oxide/iron interface. Reduction most effectively takes place when there is a balance between the extent of the contact that chromium oxide has with the iron matrix and the porosity available in the matrix. Reduction of chromium oxide is aided by contact with iron because chromium is allowed to diffuse away from the reducing particle through the iron matrix. The extent of porosity in the matrix determines the availability of channels to transport gaseous reduction reactants and products to and away from the chromium oxide.

A model was adapted from Ashby *et al*. [42, 43] that described the sintering behavior of iron having similar characteristics and heat-treatments as the iron matrix in the experimental samples. The same was done for nickel, which also produced a reasonably good comparison. The results of this model predicted that the shrinkage rates that occur in iron heated non-isothermally would generally increase with the exceptions of changes in the phase and stage of sintering. When the same model was

run for conditions including an isothermal hold, the shrinkage predicted was considerably slowed, as compared to the former conditions.

Based on the results of the model for iron, two heat-treatments were used. In one case a constant heating rate of 5°C/min was used. In the second, an isothermal hold at 1000°C was adopted. By comparing the results of the two heat-treatments the following results can be drawn.

As the samples are heat-treated in hydrogen using a constant heating rate of 5°C/min, iron oxide is first reduced. Chromium oxide reduction occurs subsequently. Sintering in the iron matrix occurs at an increasingly accelerated rate because of the non-isothermal heating. Microsturctural observations show that at temperatures above 800°C, the matrix starts to densify around the chromium oxide particles, allowing better contact with the matrix. Results of X-ray diffraction show a notable increase in the intake of chromium into the iron matrix beyond a temperature of 800°C. However, too much densification of the matrix around the particle hinders gaseous exchange at the reduction site.

Sintering in the iron matrix was slowed considerably when the samples were held isothermally. The microstructure surrounding the chromium oxide particles showed more porosity in these samples than in samples that were heated at a constant rate to the same temperature then quenched. Microstructural analysis showed that the chromium oxide particles were being eliminated at a faster rate in samples that were held isothermally than in samples that continued to be heated to higher temperatures. This was more evident when the experimental data were compared to a simple model that described the dissolution of chromium in iron. The model predicted that increasing

heat-temperatures would produce increasing dissolution kinetics. This was not evidenced by the experimental results.

Interface compositions values of chromium in iron measured at the chromium oxide/iron couple interface for different temperatures [6] were equated to the equilibrium compositions for chromium oxide reducing in hydrogen while in contact with iron [14]. This showed that P_{H_2}/P_{H_2O} was decreasing for increasing temperatures, indicating that the amount of water vapor at the interface was increasing relative to the hydrogen available. The greater the degree of sintering in the iron matrix, the more difficult it is for the gaseous reactants and products to be transported to and from the chromium oxide particles.

During the heat-treatments in which the temperature was continuously increased to 1300°C, impurities that are commonly present in the oxide precursors, especially silicon oxide and calcium oxide reacted with the reducing chromium oxide. Layers were formed around the chromium oxide that inhibited continued reduction. Phase diagrams show that these reactions occured above 1000°C. Samples that were held at 1000°C for a period of time, below the temperatures at which these reactions occur, showed that the chromium oxide continued to reduce effectively without the formation of these impurity layers.

The composition profiles taken from samples containing chromium oxide particles showed lower chromium compositions over the same distance from the particles than the profiles taken from samples containing chromium metal particles. The reduction reaction occurring in the samples with the oxide particles limited the

dissolution process, indicating that the dissolution of chromium oxide in iron is interface-controlled.

The optimum microstructure, one with the maximum chromium oxide dissolution and maximum densification after sintering, is achieved by using a controlled heating rate to 1000°C, followed by a hold at this temperature. Heating should then be continued to the final temperature. Using a hold at this temperature allows free gaseous exchange of hydrogen and water vapor to and from the particle. Reduction of the oxide and the dissolution of the particle into the metal are therefore less restricted. A hold time at this temperature also has the added benefit in that it is lower than the temperatures at which chromium oxide has interactions with silicon and calcium impurities. The chromium oxide has the opportunity to be completely reduced so that no interactions with these impurities can occur at higher temperatures. The result is that after heat-treatment is complete, any inclusions that remain in the structure are composed only of the impurities themselves, not chromium oxide surrounded by the product of interactions with these impurities. The inclusions that remain in the structure are therefore smaller and pose a reduced risk of mechanical failure. Since these impurities are commonly found in the starting materials used for producing honeycombs, limiting their ability to hamper the complete reduction is highly advantageous.

APPENDIX A

SINTERING PROGRAM

The following program was run for different particle sizes and for the heating rates and temperatures given for the experimental conditions.

```
Private Sub Form_Load()
HTSch% = 3
time#(0) = 0
Pi# = 3.141592654
increTime# = 0.1
StartTemp# = 200
EndTemp#(1) = 250
EndTemp#(2) = 400
EndTemp#(3) = 1400
HeatRate#(1) = 5
HeatRate#(2) = 3
HeatRate#(3) = 5
HoldTime#(1) = 0
HoldTime#(2) = 0
HoldTime#(3) = 0
HoldTimeCount#(1) = 0
HoldTimeCount#(2) = 0
HoldTimeCount#(3) = 0
InitPartRad# = 0.00001
SurFreeEnergy#(1) = 2.1
SurFreeEnergy#(2) = 2
ShearMod#(1) = 64000000000#
ShearMod#(2) = 81000000000#
AtomicVolume#(1) = 1.18E-29
AtomicVolume#(2) = 1.21E-29
TheoryDensity#(1) = 7620
TheoryDensity#(2) = 7650
```

```
xNeckSize#(0) = (SurFreeEnergy#(1) * (InitPartRad# ^ 2) / (10 * ShearMod#(1))) ^ (1
/ 3)
yShrinkage#(0) = (xNeckSize#(0) ^ 2) / (6 * InitPartRad#)
absyShrinkage#(0) = yShrinkage#(0) / InitPartRad#
density#(a#) = 0.5
Temp#(0) = StartTemp#
Dv0#(1) = 0.00024
Dv0#(2) = 0.00000627
Qv#(1) = 239.8
Qv#(2) = 252
dsDs0#(1) = 0.0000000025
dsDs0#(2) = 0.00000000011
Qs#(1) = 232
Qs#(2) = 220
dgDg0#(1) = 0.00000000000112
dgDg0#(2) = 0.000000000000075
Qg#(1) = 174
Qg#(2) = 159
Pvap0#(1) = 36700000000#
Pvap0#(2) = 36700000000#
Qvap#(1) = 382
Qvap#(2) = 382
R# = 0.008314
k# = 1.38E-23
End Sub

Private Sub cmdStart_Click()
a# = 0
h% = 1 'section of heating schedule

'checking which iron phase is present


Do Until time#(a#) > 10000000
   If Temp#(a#) < 912 Or Temp#(a#) > 1394 Then
      AlphaGamma% = 1
   Else
      AlphaGamma% = 2
   End If
   ' temperature fixed with time
   time#(a# + 1) = time#(a#) + increTime#

   If Temp#(a#) >= EndTemp(h%) Then
      If HoldTime#(h%) > 0 And HoldTime#(h%) > (HoldTimeCount#(h%) / 60) Then
         Temp#(a# + 1) = EndTemp(h%)
         HoldTimeCount#(h%) = HoldTimeCount#(h%) + increTime#
```

```
      Else
      h% = h% + 1
      If h% > HTSch% Then
         GoTo SavingFile
      End If
      Temp#(a# + 1) = Temp#(a#) + ((time#(a# + 1) - time(a#)) * HeatRate#(h%) / 60)
      End If
   Else
      Temp#(a# + 1) = Temp#(a#) + ((time#(a# + 1) - time(a#)) * HeatRate#(h%) / 60)
   End If


   ' other parameters fixed with temp and time
   'Diffusivities
   Dv#(a#) = Dv0#(AlphaGamma%) * Exp(-1 * Qv#(AlphaGamma%) / (R# *
(Temp#(a#) + 273.15)))

   dsDs#(a#) = dsDs0#(AlphaGamma%) * Exp(-1 * Qs#(AlphaGamma%) / (R# *
(Temp#(a#) + 273.15)))

   dgDg#(a#) = dgDg0#(AlphaGamma%) * Exp(-1 * Qg#(AlphaGamma%) / (R# *
(Temp#(a#) + 273.15)))

   Pvap#(a#) = Pvap0#(AlphaGamma%) * Exp(-1 * Qvap#(AlphaGamma%) / (R# *
(Temp#(a#) + 273.15)))


   'radius of curvature and theta values
   pRadiusCurv#(a#) = ((xNeckSize#(a#) ^ 2) + (yShrinkage#(a#) ^ 2) - (2 *
InitPartRad# * yShrinkage#(a#))) / (2 * (InitPartRad# - xNeckSize#(a#)))
   'thetaAngle#(a#) = ataN((InitPartRad# - yShrinkage#(a#)) / (xNeckSize#(a#) +
pRadiusCurv#(a#)))

   'A parameter function of surface and gb diffusion
   Aalpha#(a#) = dgDg#(a#) / dsDs#(a#)


   'curvatures
   KmCurvature#(a#) = (1 / xNeckSize#(a#)) - (1 / pRadiusCurv#(a#))
   'Debug.Print (((1 + (Aalpha#(a#) * Log(2) / (2 * Log(((xNeckSize(a#) +
pRadiusCurv#(a#)) / pRadiusCurv#(a#)) - 0.75)))) * (KmCurvature#(a#) ^ 2)))
    K2Curvature#(a#) = ((1 + (Aalpha#(a#) * Log(2) / (2 * Log(((xNeckSize(a#) +
pRadiusCurv#(a#)) / pRadiusCurv#(a#)) - 0.75)))) * (KmCurvature#(a#) ^ 2)) ^ 0.5
    K1Curvature#(a#) = (KmCurvature#(a#) ^ 2) / K2Curvature#(a#)
    K3Curvature#(a#) = 2 / ((0.74 * InitPartRad#) - xNeckSize#(a#))
```

```
   'd1 and d2 diffusion paths
   d2#(a#) = (1 + ((4 / 3) * (K2Curvature#(a#) - K1Curvature#(a#)) /
K2Curvature#(a#))) * pRadiusCurv#(a#)
   d1#(a#) = pRadiusCurv#(a#) - d2#(a#)


   'Neck Growth rates
   neckGrowthRate1#(a#) = 2 * dsDs#(a#) * (K1Curvature#(a#) ^ 3) *
SurFreeEnergy#(AlphaGamma%) * AtomicVolume#(AlphaGamma%) / (k# *
(Temp#(a#) + 273.15))
   neckGrowthRate2#(a#) = 2 * Dv#(a#) * (K1Curvature#(a#) ^ 2) *
SurFreeEnergy#(AlphaGamma%) * AtomicVolume#(AlphaGamma%) / (k# *
(Temp#(a#) + 273.15))
   neckGrowthRate3#(a#) = Pvap#(a#) * K1Curvature#(a#) *
SurFreeEnergy#(AlphaGamma%) * (AtomicVolume#(AlphaGamma%) ^ 1.5) / (((k# *
(Temp#(a#) + 273.15)) ^ 1.5) * ((2 * Pi * TheoryDensity#(AlphaGamma%)) ^ 0.5))
   neckGrowthRate4#(a#) = 4 * dgDg#(a#) * (K2Curvature#(a#) ^ 2) *
SurFreeEnergy#(AlphaGamma%) * AtomicVolume#(AlphaGamma%) /
(xNeckSize#(a#) * k# * (Temp#(a#) + 273.15))
   neckGrowthRate5#(a#) = 4 * Dv#(a#) * (K2Curvature#(a#) ^ 2) *
SurFreeEnergy#(AlphaGamma%) * AtomicVolume#(AlphaGamma%) / (k# *
(Temp#(a#) + 273.15))
   'neckGrowthRate6#(a#) = (4 / 9) * Dv#(a#) * K2Curvature#(a#) * xNeckSize#(a#) *
10000000000# * SurFreeEnergy#(AlphaGamma%) *
AtomicVolume#(AlphaGamma%) * (K2Curvature(a#) - (1.5 *
ShearMod#(AlphaGamma%) * xNeckSize#(a#) / (InitPartRad# *
SurFreeEnergy#(AlphaGamma%)))) / (k# * (Temp#(a#) + 273.15))

   neckGrowthRate6#(a#) = K2Curvature#(a#) * 4 * 100000000000000# *
(xNeckSize#(a#) ^ 2) * Dv#(a#) * (K2Curvature#(a#) - (1.5 *
ShearMod#(AlphaGamma%) * xNeckSize#(a#) / (SurFreeEnergy#(AlphaGamma%) *
InitPartRad#))) * SurFreeEnergy#(AlphaGamma%) *
AtomicVolume#(AlphaGamma%) / (k# * (Temp#(a#) + 273.15) * 9)
   If neckGrowthRate6#(a#) < 0 Then
      neckGrowthRate6#(a#) = 0
   End If

   'neckGrowthRate6#(a#) = K2Curvature#(a#) * 4 * 100000000000000# *
xNeckSize#(a#) * Dv#(a#) * SurFreeEnergy#(AlphaGamma%) *
AtomicVolume#(AlphaGamma%) / (k# * (Temp#(a#) + 273.15) * 9)
   neckGrowthRate7#(a#) = (1 / 16) * dgDg#(a#) * (K3Curvature#(a#) ^ 3) *
SurFreeEnergy#(AlphaGamma%) * AtomicVolume#(AlphaGamma%) / (k# *
(Temp#(a#) + 273.15) * (Log(0.74 * InitPartRad# * K3Curvature(a#) / 2) - 0.75))
   neckGrowthRate8#(a#) = (1 / 16) * xNeckSize#(a#) * Dv#(a#) * (K3Curvature#(a#)
^ 3) * SurFreeEnergy#(AlphaGamma%) * AtomicVolume#(AlphaGamma%) / (k# *
(Temp#(a#) + 273.15) * (Log(0.74 * InitPartRad# * K3Curvature#(a#) / 2) - 0.75))
```

```
   'Shrinkage rates
   'yShrinkRate1#(a#) = (neckGrowthRate4#(a#) + neckGrowthRate5#(a#) +
neckGrowthRate6#(a#)) * 2 * thetaAngle#(a#) * pRadiusCurv#(a#) / xNeckSize#(a#)
   yShrinkRate1#(a#) = (neckGrowthRate4#(a#) + neckGrowthRate5#(a#) +
neckGrowthRate6#(a#)) * 2 * pRadiusCurv#(a#) / xNeckSize#(a#)
   yShrinkRate2#(a#) = (neckGrowthRate7#(a#) + neckGrowthRate8#(a#)) * 4 *
(((0.74 * InitPartRad#) - xNeckSize#(a#)) ^ 2) / ((xNeckSize#(a#) ^ 2) - (((0.74 *
InitPartRad#) - xNeckSize#(a#)) ^ 2))


   If pRadiusCurv(a#) < (0.74 * InitPartRad#) - xNeckSize(a#) Then

      CurrentNeckGrowthRate#(a#) = neckGrowthRate1#(a#) + neckGrowthRate2#(a#)
+ neckGrowthRate3#(a#) + neckGrowthRate4#(a#) + neckGrowthRate5#(a#) +
neckGrowthRate6#(a#)
      CurrentyShrinkRate#(a#) = yShrinkRate1#(a#)
      densifyRate#(a#) = 0.5 * Pi * yShrinkRate1#(a#) / (InitPartRad# * ((1 -
absyShrinkage#(a#)) ^ 4))
   Else
      CurrentNeckGrowthRate#(a#) = neckGrowthRate7#(a#) + neckGrowthRate8#(a#)
      CurrentyShrinkRate#(a#) = yShrinkRate2#(a#)
      densifyRate#(a#) = 0.2 * (InitPartRad# ^ 3) * Pi * yShrinkRate2#(a#) *
((xNeckSize#(a#) ^ 2) - (((0.74 * InitPartRad#) - xNeckSize#(a#)) ^ 2)) / (((0.74 *
InitPartRad#) ^ 5) * ((0.74 * InitPartRad#) - 1.45 * ((0.74 * InitPartRad#) -
xNeckSize#(a#))))
   End If


   'neck size and shrinkage
   xNeckSize#(a# + 1) = xNeckSize#(a#) + ((time#(a# + 1) - time#(a#)) *
CurrentNeckGrowthRate#(a#))
   yShrinkage#(a# + 1) = yShrinkage#(a#) + ((time#(a# + 1) - time#(a#)) *
CurrentyShrinkRate#(a#))
   absyShrinkage#(a# + 1) = yShrinkage#(a# + 1) / InitPartRad#

   'density and porosity
   'density#(a#) = 0.5 * ((1 - absyShrinkage#(a#)) ^ -3)
   density#(a# + 1) = density#(a#) + ((time#(a# + 1) - time(a#)) * densifyRate#(a#))
   porosity#(a#) = 1 - density#(a#)


   a# = a# + 1
   If xNeckSize(a#) > (InitPartRad# * 0.74) Then
      GoTo SavingFile
   End If
```

```
   'alpha-gamma phase check
   Debug.Print "checking", a#, xNeckSize#(a#), pRadiusCurv#(a# - 1), time#(a#), "temp", Temp#(a#), h%, CurrentyShrinkRate#(a# - 1), CurrentNeckGrowthRate#(a# - 1)
   Debug.Print neckGrowthRate1#(a# - 1), neckGrowthRate2#(a# - 1), neckGrowthRate3#(a# - 1), neckGrowthRate4#(a# - 1), neckGrowthRate5#(a# - 1), neckGrowthRate6#(a# - 1), neckGrowthRate7#(a# - 1), neckGrowthRate8#(a# - 1)
Loop
GoTo SavingFile
' After sintering or heat treatment is done, getting the data in a file.
SavingFile:
Open "C:\McIntosh\Visual basic Programs\Sintering Model Results\SinteringData.txt" For Output As #1
   Write #1, "Time (s)", "Temp (°C)", "Neck Size (m)", "Shrinkage Rate (m/s)", "Shrinkage (m)", "Fractional Density"
   For z# = 5 To a# Step 5
      Write #1, time#(z#), Temp#(z#), xNeckSize#(z#), CurrentyShrinkRate#(z#), yShrinkage#(z#), density#(z#)
   Next z#
Close #1
End Sub
```

APPENDIX B

DISSOLUTION PROGRAM

The program for the dissolution of chromium oxide in iron is written in MathLab and is given below.

```
% Based on Whelan's treatment
% Metal Science Journal, 1969, V.3, p. 95
close all;
clear all;
% k=2*(CI-Cm)/(Cp-CI)
dt=1;
k=0.22222222222222;
Do=240e+6; %diffusion factor
R(1)=15; % initial radius
Temp=1273.15; %initial starting temperature in Diffusivity equation units
Rg=8.314; % gas constant
Q=239800; % activation energy
hr=0; %heating rate in temp units per second
count=0;
for i=1:6000
   t=i*dt;
   time(i)=t;
   Temp=Temp+hr*time(i);
   D=0.05
   %D=Do*exp(-Q/(Rg*Temp));
   tau(i)=D*k*t/(R(1)^2);
   R(i+1)=R(i)-k*D*dt/(R(i))-k*dt*((D/(t*pi))^(1/2));
   RR(i)=R(i+1)/R(1); %dimensionless radius
end

figure(1)
plot(tau,RR); % plot of dimensionless radius vs. dimensionless time
figure(2)
for i=1:length(RR)
   Rad(i)=R(1)*RR(i);
```

```
end
plot(time,Rad)
dattime=transpose(time);
datRad=transpose(Rad);
dlmwrite('dattimesphere.dat',dattime);
dlmwrite('datRadsphere.dat',datRad);
```

APPENDIX C

SALTYKOV'S ANALYSIS

The sizes of particles observed in a section of a three dimensional microstructure, are not necessarily the true particle sizes. The diameter of the observed particle section is equal to or less that the actual particle diameter. Using the probabilities that a spherical particle may be sectioned in any particular position, Saltykov [55] devised a method to predict the particle size distribution of particles in a matrix from the distribution of their sections.

C.1 Saltykov's Method

C.1.1 Size Class Interval

The minimum number of size classes that should be used for Saltykov's method to produce reasonable results is seven. The maximum number of size classes for which coefficients are given is fifteen. The size class interval Δ, is defined as

$$\Delta = \frac{d_m}{K} \qquad [C.1]$$

where d_m is the largest particle section diameter and K is the number of size classes. The maximum K should be chosen such that Δ is not smaller that the resolution of the microscope.

C.1.2 Particle Size Distribution

The particle section diameters are separated into the size classes of, [0 to Δ], [Δ to 2Δ],…., [(i-1) Δ to iΔ],…., [(K-1)Δ to KΔ] such that $(N_A)_1$, $(N_A)_2$,…., $(N_A)_i$,…, $(N_A)_K$, are the numbers of particle sections per unit area that fall within each size class. The number of particles per unit volume N_V is related to N_A by the following equation

$$\left(N_V\right)_j = \sum_{i=j}^{K} b_{(j,i)} \frac{\left(N_A\right)_i}{\Delta} \qquad [C.2]$$

where are Saltykov's coefficients, given in the Table C.1. It should be noted that Saltykov's coefficients are negative for i > j and positive for i = j.

Table C.1: Saltykov's Coefficients $b_{(j, i)}$

j\i	1	2	3	4	5	6	7	8	9	10	11	12	13	14	15
1	1	0.1547	0.0360	0.013	0.0061	0.0033	0.0020	0.0013	0.0009	0.0006	0.0005	0.0004	0.0003	0.0002	0.0001
2		0.5774	0.1529	0.042	0.0171	0.0087	0.0051	0.0031	0.0021	0.0015	0.0010	0.0009	0.0006	0.0006	0.0004
3			0.4472	0.1382	0.0408	0.0178	0.0093	0.0057	0.0037	0.0026	0.0018	0.0013	0.0010	0.0007	0.0007
4				0.3779	0.1260	0.0386	0.0174	0.0095	0.0058	0.0038	0.0027	0.002	0.0016	0.0012	0.0009
5					0.3333	0.1161	0.0366	0.0168	0.0094	0.0059	0.004	0.0028	0.0021	0.0016	0.0013
6						0.3015	0.1081	0.0346	0.0163	0.0091	0.0058	0.0041	0.0028	0.0022	0.0016
7							0.2773	0.1016	0.0329	0.0155	0.0090	0.0057	0.0040	0.0029	0.0022
8								0.2582	0.0961	0.0319	0.0151	0.0088	0.0056	0.0039	0.0028
9									0.2425	0.0913	0.0301	0.0146	0.0085	0.0055	0.0039
10										0.2294	0.0872	0.0290	0.0140	0.0083	0.0054
11											0.2182	0.0836	0.0280	0.0136	0.0080
12												0.2085	0.0804	0.027	0.0132
13													0.2000	0.0776	0.0261
14														0.1925	0.0750
15															0.1857

Table C.2: Particle size distribution for a 15wt% sample heat-treated to 1000°C with a hold time of 10mins

Size Class μm	N_v m^{-3}
0-1.90229	2378960.799
1.90229-3.80458	685408.3758
3.80458-5.70686	69770.19013
5.70686-7.60915	18263.97135
7.60915-9.51144	7353.014341
9.51144-11.41373	3865.038123
11.41373-13.31601	2095.970716
13.31601-15.21830	361.1615561
15.21830-17.12059	248.6303391
17.12059-19.02288	437.0015508
19.02288-20.92516	150.0580064
20.92516-22.82745	0
22.82745-24.72974	36.32258982
24.72974-26.63203	0
26.63203-28.53432	91.27340905

Table C.3: Particle size distribution for a 15wt% sample heat-treated to 1000°C with a hold time of 100mins

Size Class μm	N_v m^{-3}
0-1.25775	0
1.25775-2.51550	1709.0352
2.51550-3.77325	1722.1597
3.77325-5.03000	3714.9195
5.03000-6.28875	647.03249
6.28875-7.54649	0
7.54649-8.80424	695.43453

REFERENCES

[1] J. Wittenauer, B. Norris, Journal of Metals 43 (1990) 36-41.

[2] K. M. Hurysz, R. Oh, J. K. Cochran, J. T. H. Sanders, K. J. Lee, Modeling Powder Extrusion Pastes for Forming Lightweight Multifunctional Structures, in: '', Processing Properties of Lightweight Cellular Metals and Structures, vol TMS, 2002. 167-176.

[3] K. M. Hurysz, Paste Mechanics for Fine Extrusion, in: '', School of Materials Science and Engineering, vol Georgia Institute of Technology, Atlanta, 2001.

[4] L. J. Gibson, M. F. Ashby, Cellular Solids: Structure and Properties,, Pergamon Press, New York, 1988.

[5] J. S. Reed, Principles of Ceramic Processing, John Wiley & Sons Inc., New York, 1995.

[6] J. H. Nadler, The Hydrogen Reduction of Iron and Chromium Oxides, in: '', School of Materials Science and Engineering, vol Georgia Institute of Technology, Atlanta, 2003. 155.

[7] A. A. El-Geassy, ISIJ International 37 (1997) 844-853.

[8] A. A. El-Geassy, Ironmaking and Steelmaking 26 (1999) 41-52.

[9] C. Gleitzer, Solid State Ionics 38 (1990) 133-141.

[10] M. Gougeon, B. Dupre, C. Gleitzer, Metallurgical Transactions B 17B (1986) 657-663.

[11] S. E. Khalafalla, J. P. L. Weston, Transactions of the Metallurgical Society of AIME 239 (1967) 1494-1499.

[12] M. Moukassi, P. Steinmetz, B. Dupre, C. Gleitzer, Metallurgical Transactions B 14B (1983) 125-132.

[13] E. Newberg, J. N. Pring, Proceedings of the Royal Society of London Series A 92 (1916) 276-285.

[14] Y. G. Gurevich, I. D. Radomysel'skii, L. F. Barshchevskaya, N. R. Frage, Y. I. Pozhidaev, Poroshkovaya Metallurgiya 1 (1975) 16-19.

[15] M. G. Walls, A. Ponthieux, B. Rondat, R. A. Owen, Journal of Vacuum Science Technology A 14 (1996) 1362-1367.

[16] J. H. Nadler, J. T. H. Sanders, J. K. Cochran, Reduction of Iron and Chromium Sesquioxide Powder Mixtures for Metal Honeycomb Structures, in: ", Processing and Properties of Lightweight Cellular Metals and Structures, vol The Metals Minerals and Materials Society, 2002. 147-155.

[17] J. H. Nadler, J. T. H. Sanders, R. F. Speyer, Journal of the Materials Research Society 18 (2003) 1787-1794.

[18] H. J. T. Ellingham, Journal of the Society of Chemical Industry Transactions and Communications 63 (1944) 125-133.

[19] O. Kubaschewski, C. B. Alcock, P. J. Spencer, Materials Thermochemistry, Pergamon Press, New York, 1993.

[20] J. M. W. Chase, NIST-JANAF Thermochemical Tables, American Institute of Physics, Woodbury, New York, 1998.

[21] J. H. Nadler, J. T. H. Sanders, J. K. Cochran, S. S. Kim, Oxide Reduction and Diffusion in Fe-Cr Alloy Honeycombs, in: ", 2nd International Conference on Thermal Process Modeling and Computer Simulation, vol 2003.

[22] R. Maddin, J. D. Muhly, T. S. Wheeler, Scientific American 237 (1977) 122-131.

[23] J. Christie, How Did Ancient Metallurgists Think to Reduce Iron Oxide to Iron? Do We Know?: www.madsci.org/posts/archives/jan99/915460743.sh.r.html, 1999.

[24] C. Laurent, C. Blazczyk, M. Brieu, A. Rousset, NanoStructured Materials 6 (1995) 317-320.

[25] I. Arsentyeva, B. Jordovic, D. Krsmanovic, Science of Sintering 30 (1998) 11-17.

[26] B. Jordovic, D. Krsmanovic, I. Arsentyeva, Science of Sintering 30 (1998) 149-155.

[27] C. G. Maier, U. S. Bureau of Mines Bulletin 436 (1989) 1-109.

[28] M. N. Rich, Method of Obtaining Chromium, in: ", vol US, 1929. 2.

[29] W. Rohn, Method of Producing Chromium, in: ", vol US, 1933.

[30] P. P. Alexander, Method for Reduction of Refractory Oxides, in: ", vol US, 1936.

[31] R. M. German, Sintering Theory and Practice, John Wiley & Sons Inc., New York, 1996.

[32] O. Kubaschewski, G. Heymer, Acta Metallurgica 8 (1960) 416-423.

[33] T. Ohmi, Y. Nakagawa, M. Nakamura, A. Ohki, Journal of Vacuum Science Technology A14 (1996) 2505-2510.

[34] P. J. Alberry, C. W. Haworth, Metal Science 8 (1974) 407-412.

[35] H. Baker, ASM Handbook, ASM International, Materials Park, Ohio.

[36] A. Salak, Ferrous Powder Metallurgy, Cambridge International Science, Cambridge UK, 1995.

[37] R. M. German, An Overview of Enhanced Sintering Treatments for Iron, in: ", Sintering and Heterogeneous Catalysis, vol 16, Materials Science Research, 1984. 103-114.

[38] F. Thummler, W. Thomma, Metallurgical Reviews 12 (1967) 69-108.

[39] D. L. Johnson, Ultra-Rapid Sintering, in: Kuczynski, Miller, Sargent ", Sintering & Heterogeneous Catalysis, vol 16, Materials Research Society, 1984. 243-252.

[40] P. Roura, J. Costa, J. Farjas, Materials Science and Engineering A 337 (2002) 248-253.

[41] S. Haglund, J. Agren, P. Lindskog, Zeitschrift fur Metallkunde 89 (1998) 323-326.

[42] M. F. Ashby, Acta Metallurgica 22 (1974) 275-289.

[43] F. B. Swinkels, M. F. Ashby, Acta Metallurgica 29 (1981) 259-281.

[44] S. Haglund, J. Agren, B. Uhrenius, Zeitschrift fur Metallkunde 89 (1998) 316-322.

[45] A. Schoeler, W. Bleck, R. Link, Steel Research 71 (2000) 551-559.

[46] M. O. Prado, E. D. Zanotto, C. R. Chimie 5 (2002) 773-786.

[47] M. O. Prado, C. Fredericci, E. D. Zanotto, Journal of Non-Crystalline Solids 331 (2003) 157-167.

[48] J. W. Martin, R. D. Doherty, B. Cantor, Stability of Microstructure in Metallic Systems, Cambridge University Press, Cambridge, 1997.

[49] H. B. Aaron, G. B. Kotler, Metallurgical Transactions 2 (1971) 393-408.

[50] R. A. Tanzilli, R. W. Heckel, Transactions of the Metallurgical Society of AIME 242 (1968) 2313-2321.

[51] J. Frank V. Nolfi, P. G. Shewmon, J. S. Foster, Transactions of the Metallurgical Society of AIME 245 (1969) 1427-1433.

[52] L. Boltzmann, Ann. Physik 53 (1894) 960.

[53] C. Matano, Japan J. Physics 8 (1932) 109.

[54] U. H. Tundal, N. Ryum, Metallurgical Transactions A 23A (1992) 433-444.

[55] S. A. Saltykov, The Determination of the Size Distribution of Particles in an Opaque material from measurement of the Size Distribution of their Sections, in: Lecture Notes in Stereology, vol Springer Verlang, New York, 1967.

[56] A. Gokhale, Personal Communication, in: ", vol 2004.

[57] J. B. Nelson, D. P. Riley, An Experimental Investigation of Extrapolation Methods in the Derivation of Accurate Unit-Cell Dimensions of Crystals, in: ", Proceedings of the Physics Society, vol 57, London, 1945. 160-177.

[58] A. Taylor, H. Sinclair, in: ", Proceedings of the Physics Society, vol 57, London, 1945. 126.

[59] W. B. Pearson, W. B. Pearson Lattice Spacings and Structures of Metals and Alloys, Pergamon Press, New York, 1958.

[60] M. H. Kedr, ISIJ International 40 (2000) 309-314.

[61] E. M. Levin, R. S. Roth, Phase Diagrams for Ceramists, in: vol American Ceramic Society, Westerville, OH.

[62] W. Kurz, D. J. Fisher, Atom Transfer at the Solid/Liquid Interface, in: Fundamentals of Solidification, vol Trans Tech Publications Ltd., Aedermannsdorf, Switzerland, 1992. 21-44.

VITA

Monique Sandra McIntosh was born in the twin island country of Trinidad and Tobago to parents Curtis Emanuel McIntosh and Claudette Sandra (Booth) McIntosh. The youngest of three girls, she now has two brothers-in-law and a young nephew. Monique enrolled into Georgia Tech as an Undecided Engineering Major in the Fall of 1996 and soon decided on Materials Engineering as her major. She graduated with a Bachelors degree in Materials Science and Engineering in Spring 1999 and started her graduated studies later that Fall. Monique received her Ph.D. from the same institution in the Spring of 2005.